

DISSERTATION

Numerical Simulations of Metal Matrix Composites - Tribological Behavior and Finite Strain Response on Different Length Scales

ausgeführt zum Zwecke der Erlangung des akademischen Grades eines
Doktors der technischen Wissenschaften unter der Leitung von

Univ.Doiz. Dipl.-Ing. Dr.techn. Heinz Pettermann

E317

Institut für Leichtbau und Struktur-Biomechanik

eingereicht an der Technischen Universität Wien

Fakultät für Maschinenwesen und Betriebswissenschaften

von

Dipl.-Ing. Christopher O. HUBER

Matrikelnummer: 9125447

Pannaschg. 7/2/5

1050 Wien

Wien, im Februar 2008

Christopher Huber

ABSTRACT

The present thesis is concerned with the computational simulation of Metal Matrix Composites (MMCs), a material where particulate reinforcements are embedded in a metal phase, and which bears the potential to be tailored to particular applications. The objective of this work is to improve computational predictions, on the one hand, of the thermo-mechanical behavior in frictional contact and, on the other hand, of the elastoplastic properties of MMCs undergoing finite strains. Both topics follow a hierarchical approach employing micromechanical methods within the continuum mechanics approach.

The first executive chapter deals with computational predictions of the tribological behavior of MMCs. The influence of particle volume fraction and clustering of particles is investigated at different length scales. Finite Element simulations are performed employing periodic unit cells based on homogeneous, randomly distributed inclusions in a matrix phase with 30% particle volume fraction. In addition, the present work introduces modified unit cells with 10% particle volume fraction, with both homogeneous random and clustered distributions. These modifications are derived from the original cell by either randomly removing inclusions in the former case, or from a predefined area in the latter case. Based on these experiences, numerical simulations employing the Finite Element Method (FEM) of the frictional behavior of a MMC material, including heat conduction in the steady state, are performed. Experiments and analytical calculations serve to determine certain unknown process parameters by employing a simplified model by means of homogenizing the material. Within the scope of this model, heat transfer and conduction

are described. In the FEM simulations, the inhomogeneous body is considered. Limitations of the thermo-elastic FEM predictions are related to frictionally excited thermo-elastic instability, the stability limit is estimated analytically using two different approaches from the literature and compared to the simulation findings. The limited number of experimental tests does not allow for quantitatively reliable results but the analytical and the FEM simulations' predictions are qualitatively compared. The practical consequences of thermoelastic instability are discussed.

The second executive chapter deals with computational simulations of elasto-plastic properties of a particulate metal matrix composite (MMC) undergoing finite strains. Two different procedures are utilized for homogenization and localization; an analytical constitutive material law based on a mechanics of materials approach, and a periodic unit cell method. Investigations are performed on different length scales – the macroscale of the component, the mesoscale where the MMC is regarded as homogenized material, and the microscale corresponding to the particle size. The FEM is employed to predict the macroscopic response of a MMC component. Its constitutive material law has been implemented into the employed FEM package, based on the incremental Mori Tanaka (IMT) approach and extended to the finite strain regime. This approach gives access to the meso-scale fields as well as to approximations for the micro-scale fields in the individual MMC phases. Selected locations within the macroscopic model are chosen to extract general loading histories. These deformation and temperature histories are applied to unit cells using the periodic microfield approach (PMA). As a result, mesoscopic responses as well as highly resolved microfields in the matrix and the particles are available. A Gleeble-type experiment employing an MMC with 20%vol of particles is investigated as an example. Comparisons of the IMT and the PMA are performed on the macro-, meso-, and microlevels to investigate if the IMT is a tool capable of predicting the behavior of an entire MMC component in the first place, and to assess its limits.

The two constitutive laws, Incremental Mori-Tanaka and J2-plasticity, are compared to

determine how large an error is made (on the mesoscopic level) if the behavior of the inhomogeneous material is described by a homogeneous, isotropic material model employing the uniaxial stress-strain curve of the MMC and adopting J2-plasticity for the post-yield regime. Furthermore, a method to address mesoscopic strain concentration of periodic unit cells under certain circumstances is presented.

KURZFASSUNG

Die vorliegende Arbeit befasst sich mit der numerischen Simulation von Metallmatrix Composites (MMCs), einem Material, in dessen Metallphase Verstärkungen in Form von Partikeln eingebettet sind. MMCs zeichnen sich, wie andere Composites auch, dadurch aus, dass sie auf bestimmte Anwendungsgebiete und -fälle hin 'zugeschnitten' werden können. Ziel der Arbeit ist es, verbesserte Vorhersagen – einerseits auf dem Gebiet des thermo-mechanischen Verhaltens unter Reibbelastung, andererseits auf dem Gebiet der elasto-plastischen Eigenschaften von MMCs unter großen Verzerrungen – zu entwickeln. Beide Aufgabenstellungen nutzen einen hierarchischen Zugang und verwenden mikromechanische Methoden der Kontinuumsmechanik.

Nach einer Einführung beschäftigt sich das zweite Kapitel mit der Vorhersage des tribologischen Verhaltens von MMCs. Der Einfluss des Partikelvolumensanteils sowie von Clustering der Inklusionen wird auf verschiedenen Längenskalen untersucht. Finite Elemente (FE) Simulationen periodischer Einheitszellen werden durchgeführt, wobei eine Einheitszelle mit homogener, zufälliger Verteilung der Inklusionen in der Matrixphase mit einem Partikelvolumensanteil von 30% verwendet wird. Diese Einheitszelle wird weiters modifiziert hinsichtlich ihres Volumensanteils (10%) sowie der Art der Verteilung der Partikel (homogen-zufällig – bzw. in Clustern). Aufbauend auf der Auswertung dieser Berechnungen werden numerische Simulationen des Reibverhaltens von MMCs durchgeführt, auch unter Berücksichtigung der Wärmeleitung im thermo-mechanischen Gleichgewichtszustand. Experimente und analytische Berechnungen dienen zur Bestimmung unbekannter

Prozessparameter an einem vereinfachten Modell durch homogenisierte Betrachtungsweise des Materials. In Rahmen dieses vereinfachten Modells werden Wärmeübergang und Wärmeleitung beschrieben. Im Gegensatz dazu werden in den FE Simulationen die inhomogenen Körper betrachtet. Die Grenzen der entsprechenden thermo-elastischen Simulationen werden auf die durch Reibung angeregte, thermo-elastische Instabilität zurückgeführt. Das Stabilitätslimit wird mithilfe zweier unterschiedlicher Methoden aus der Literatur abgeschätzt und mit Ergebnissen aus numerischen Simulationen verglichen. Die begrenzte Anzahl der experimentellen Tests erlaubt zwar keinen quantitativen Vergleich, die analytischen und die FE Vorhersagen werden aber qualitativ gegenübergestellt und die praktischen Konsequenzen von thermo-elastischer Instabilität diskutiert.

Das dritte Kapitel beschäftigt sich mit der numerischen Simulation elasto-plastischer Eigenschaften partikelverstärkter MMCs unter großen Deformationen. Für Homogenisierung und Lokalisierung werden zwei unterschiedliche Vorgangweisen eingeschlagen: ein analytisches Konstitutivgesetz basierend auf einem Kontinuumsmechanik-Ansatz sowie eine Einheitszellenmethode. Die Untersuchungen werden auf verschiedenen Längenskalen durchgeführt – der Makroebene der Komponente, der Mesoskala, auf der der MMC als homogenisiertes Material betrachtet wird, und der Mikroebene entsprechend der Partikelgröße. Die FE Methode wird eingesetzt, um die makroskopische Antwort des MMCs vorherzusagen. Das dazu verwendete Konstitutivgesetz wurde in den benutzten FE-Code als Subroutine implementiert. Es basiert auf der inkrementellen Mori Tanaka (IMT) Methode und wird für große Deformationen erweitert. Diese Vorgehensweise liefert die mesoskopischen Felder sowie Approximationen für die Mikro-Felder in den einzelnen Phasen des MMCs. Belastungsgeschichten werden aus ausgewählten Bereichen innerhalb des makroskopischen Modells extrahiert. Diese Deformationsgeschichten werden in Form von Randbedingungen auf Einheitszellen mit periodischen Randbedingungen aufgebracht. Als Ergebnis erhält man die mesoskopischen Antworten sowie hoch aufgelöste Mikrofelder in der Matrix und den Partikeln. Der Stauchversuch eines MMCs mit 20%vol Partikeln wird als Beispiel untersucht. Die IMT wird mit den Einheitszellenrechnungen auf den verschiedenen Längenskalen

verglichen, um einerseits zu bestimmen, ob die IMT als Instrument zur Vorhersage des Verhaltens einer MMC-Komponente geeignet ist, und andererseits auch, um ihre Grenzen zu beurteilen.

Weiter werden die Konstitutivgesetze IMT und J2-Plastizität miteinander verglichen. Ziel ist es, zu beurteilen, welcher Fehler auf mesoskopischer Ebene gemacht wird, wenn das Verhalten des inhomogenen Materials durch ein homogenes, isotropes Materialmodell beschrieben wird, dessen Materialparameter aus dem einachsigen Spannungs-Dehnungsverlauf des MMCs bestimmt werden und dessen plastisches Verhalten mit der J2-Plastizität beschrieben wird. Zuletzt wird eine Methode vorgestellt, welche die Konzentration von Verzerrungen innerhalb der Einheitszellen unter bestimmten Umständen unterbindet.

Acknowledgements

The present work was carried out in the course of my employment at the Institute of Lightweight Design and Structural Biomechanics at the Vienna University of Technology. The funding of the Austrian Aerospace Research (AAR) / Network for Materials and Engineering by the Austrian Federal Ministry of Economics and Labor is gratefully acknowledged.

I am deeply indebted to my thesis supervisor, Univ. Doz. Dr. H. Pettermann, for giving me the opportunity to do the doctorate in the first place. His support and guidance were the basis of this thesis. I also thank him for his experienced, invaluable advice in countless discussions and his patience during this work. My gratitude also belongs to Prof. Antretter for accepting the co-advisorship. His advice and perspective are very much appreciated. Additionally, I would also express my thanks to all my former and current colleagues at the ILSB. The amazing atmosphere, really unique in terms of positiveness, creates an exceptional environment of support and friendship. Special mentions go out to Clara Schuecker, Mathias Luxner, Robert Bitsche, Christian Grohs and Gerald Wimmer ... and Gerhard Schneider, of course, for all his UNIX wizardry.

I look back very positively to cooperations with Cecilia Poletti (IMK), Andreas Merstallinger (ARCS), and Sascha Kremmer (Böhler Schmiedetechnik).

Finally, I would like to express my gratitude to Profs. H. J. Böhm and F. G. Rammerstorfer, who are certainly most responsible for creating the special ILSB environment.

Contents

ABSTRACT	III
KURZFASSUNG	VI
ACKNOWLEDGEMENTS	IX
1 Introduction	1
1.1 Introduction to composites	1
1.2 Scope of the present work	4
1.3 Micromechanical methods	6
1.3.1 Micromechanics approach	6
1.3.2 Homogenization and localization basics	7
1.3.3 The Mean Field approach (MFA)	8
1.3.4 Periodic microfield approach	13
2 Numerical simulations of the tribological behavior of Metal Matrix Composites	22
2.1 Tribology basics	23
2.1.1 Literature review	23

2.1.2	Surfaces	24
2.1.3	Friction	25
2.1.4	Frictional heating	27
2.1.5	Heat conduction and partitioning	28
2.1.6	Wear	30
2.2	Experimental test setup	33
2.3	Influence of different volume fractions and particle distributions on the frictional response to a macroscopic frictional load	35
2.3.1	Modeling approach	36
2.3.2	Example	39
2.3.3	Results	41
2.4	Analyses of the tribological behavior of MMCs under consideration of frictionally excited thermoelastic instability	52
2.4.1	Simplified analytical model	52
2.4.2	Heat fluxes, heat partitioning factor, thermal contact resistance	53
2.4.3	Heat balance	55
2.4.4	Derivation of thermal contact resistance and heat partitioning factor	56
2.4.5	Thermoelastic instability	58
2.4.6	Finite element model	61
2.4.7	Results	62

2.4.8	Conclusion	66
3	Forming simulations of MMC components by a micromechanics based hierarchical FEM approach	68
3.1	Introduction	68
3.1.1	Motivation and scope	68
3.1.2	Literature review	69
3.2	Modeling approach	70
3.3	Example	75
3.4	Results	76
3.4.1	Macro response: deformation	76
3.4.2	Meso response: Cauchy stresses	77
3.4.3	Micro response	81
3.4.4	Conclusion	86
3.5	Mesoscopic strain concentration/localization in periodic unit cells	87
3.5.1	Problem description, identified conditions, and an approach to prevent mesoscopic strain concentration in the employed unit cells . . .	87
3.5.2	Method	91
3.5.3	Example and results	91
3.5.4	Conclusion	104

3.6	Comparison of the two constitutive laws, J2-plasticity and Incremental Mori-Tanaka	105
3.6.1	Method	105
3.6.2	Example, mesoscopic results, and conclusion	106
3.6.3	Incremental Mori-Tanaka hardening behavior	110
4	Summary	113
A	Transformation of the deformation to rotated coordinate systems, step by step procedure	115
	Bibliography	118

Chapter 1

Introduction

1.1 Introduction to composites

The better part of 'every day' products is made from monolithic materials, consisting of either a single material or a combination of materials with their individual components hardly distinguishable, e.g. a metal alloy. A composite, on the other hand, is defined a material consisting of different constituents which are essentially insoluble¹⁾ in each other and bonded along the shared interface. A typical composite topology is depicted by the matrix-inclusion type, employing a connected phase (the matrix) and a distributed phase (the inclusions). Various classifications are possible, e.g. by inclusion type in particulate or fibrous phases, where the latter can be subclassified further into short or long fiber reinforcements, compare Fig. 1.1. Materials with short and long fiber reinforcements with random orientations, many polycrystals, and porous or cellular materials typically exhibit statistically isotropic behavior – global thermal and elastic properties are invariant with respect to orientation. In this case two independent parameters are needed to describe the elastic behavior and a single parameter for thermal expansion. Alignment of rein-

¹⁾or solubility is prevented during manufacturing

forcements typically causes statistically transversely isotropic behavior. In this case, five independent elastic and two thermal expansion parameters are sufficient for describing the global thermo-elastic behavior. If the reinforcements are embedded in a metallic matrix, the composite is denoted *metal matrix composite* (MMC), with the inclusions being metallic or metal-based (carbides) or non-metallic (ceramics). In this case, for equiaxed reinforcements of statistically homogeneous distribution, material symmetry is reduced to statistical isotropy with two independent elastic parameters and one for the effective linear thermal expansion.

Metal matrix composites and typical applications

The global material behavior of an MMC is subject to the individual material properties of the constituents, their volume fraction, aspect ratio, distribution of inclusions, as well as distribution of orientation or size (if polydisperse). Selective influence on the above properties during manufacturing, if possible, gives rise to 'tailoring' of the global properties towards a designated value. The drawback of these 'designed' materials is – due to the complex manufacturing processes – cost.

Manufacturing of MMCs is performed with the matrix being either in liquid state – the simplest (and cheapest) method by simply stir mixing the inclusions into the molten matrix (*slurry casting*), compare e.g. [Suresh et al., 1993], or by *infiltration* of a preform by pressure or vacuum [Zweben, 2000]. Solid state processing includes *powder consolidation*, where



Figure 1.1: Classification of composites by inclusion type [Schuecker, 2005].

powders of the constituents are compacted in a die and sintered [Zweben, 2000].

While scientific research on MMCs has been done for about four decades, the actual use of these materials in general applications has not been initiated until some 15 years ago. Mass market products include developments of the automotive and aerospace industry as well as sporting goods. The driving force and motivation to use advanced composite materials often is enhancing performance in terms of mass reduction or efficiency, e.g. considering fuel economy. This also serves to explain the increased use of light metals in, e.g., automotive chassis or engine blocks [Suresh et al., 1993; Zweben, 2000]. As mentioned above, MMC materials also bear the potential to be tailored to particular applications. This, however, requires profound understanding of the mechanisms of interaction of the constituents on the microlevel and their effect on the global behavior. While the opportunities of composite materials are inviting, there is also the problem of technical feasibility, cost effective production, and tooling. Thus, particle reinforced MMCs commonly are carving out the niche of being produced in a relatively cost effective way when compared to continuously reinforced materials.

MMCs have a strong position in the aerospace industry, especially with the use of titanium alloys as the matrix and the associated improvements of certain characteristics with respect to elevated temperatures, favoring lightweight materials with high specific strengths and stiffnesses. Controlled thermal expansion coefficients as well as stability in thermal cycling are also motivations behind making use of MMC capabilities. Excellent examples for these cases are turbine blades, where also the noteworthy heat resistance of MMCs comes into play [Suresh et al., 1993]. There is also extensive use of composites in helicopters [Suresh et al., 1993] – while temperatures are lower in skin structures and polymer matrix based composites are used, the rotor applications are in need of higher (specific) strengths and stiffness. In this context, MMCs are established for example in transmission structures as well as swash plates [Suresh et al., 1993].

Wear resistant material is employed in applications such as cutting tools or wear resistant

surface finishes – fields where the high temperature strength as well as hardness of carbides shine. Because of their brittleness in pure form, dispersion in a metallic matrix to increase toughness is a very reasonable way to go, again paving the way to the application of MMCs in this field.

1.2 Scope of the present work

This thesis comprises two executive chapters following a theory part, the first one (chapter 2) dealing with tribological investigations while the second (chapter 3) focuses on predicting finite strain deformations of MMCs. Both employ numerical simulations using the Finite Element method (FEM) within a hierarchical approach. Micromechanical methods are used within the continuum mechanics of materials approach on every length scale.

The objective of the tribological investigations is to present a method, on the one hand, for predicting the global response, i.e. the macroscopic coefficient of friction. On the other hand, the mesoscopic and microscopic responses are predicted in terms of stress and strain distributions as a result of frictional loading of an inhomogeneous material. The influence of different particle volume fractions as well as distributions in form of clustering of particles is treated. Furthermore, a method is presented to predict the thermoelastic behavior of MMCs in typical frictional contacts by different approaches. Analytical calculations accompanying experimental results performed at the Austrian Research Centers in Seibersdorf serve as an input to simulations employing FEM. Experimental results [Poletti et al., 2004] show increased coefficients of friction as well as wear with higher sliding velocity, possibly indicating a change in mechanisms. The effects of frictionally excited thermoelastic instability (TEI), associated with thermo-mechanical coupling at the contact surface, are investigated and a connection or contribution of TEI to the aforementioned experimental findings is assessed.

The second executive part deals with computational simulations of an elasto-plastic par-

ticulate metal matrix composite undergoing finite strains. Two different approaches are utilized for homogenization and localization; an analytical constitutive material law based on a mean field approach, and a periodic unit cell method. Investigations are performed on different length scales within a hierarchical approach. The Finite Element Method is employed to predict the macroscopic response of a component made from a metal matrix composite. Its constitutive material law, based on the incremental Mori-Tanaka approach, has been implemented into a Finite Element Method package, and is extended to the finite strain regime. This approach gives access to the mesoscale fields as well as to approximations for the microscale fields in the individual phases of the composite. Selected locations within the macroscopic model are chosen and their entire mesoscopic deformation history is applied to unit cells using the periodic microfield approach. As a result, mesoscopic responses as well as highly resolved microfields are available. A Gleeble-type experiment (a compression test of a cylindrical specimen) employing a metal matrix composite with 20vol% of particles is investigated as an example to determine if the incremental Mori-Tanaka approach qualifies as an appropriate constitutive law for the studied application.

1.3 Micromechanical methods

The description of the MMC material is performed on different length scales, the latter shall be defined in this work as following.

- *Macroscale* ... the length scale of a component
- *Microscale* ... the length scale set by the inclusions, e.g. diameter or mean distance between.
- *Mesoscales(s)* ... intermediate length scale(s), e.g. subdomains of the model, clusters of particles

It is noted that the inclusions as well as the matrix may be inhomogeneous themselves, giving rise to additional scales which can be linked formally via the micromechanics approach.

1.3.1 Micromechanics approach

The central aim of micromechanical approaches is to bridge the involved length scales. The principal idea employed is to split the stress and strain fields of inhomogeneous materials into contributions of these individual length scales, which have to be sufficiently different. On every chosen length scale the material behavior is described by that of an energetically equivalent homogenized material. Throughout these processes and on every scale chosen in this work, the continuum micromechanics approach is employed, i.e., investigations of properties are performed at the microscale using the continuum mechanics framework.

1.3.2 Homogenization and localization basics

The transition from a higher to a lower scale is performed by *localization* whereas the reverse approach is denoted *homogenization*. Computations which operate on several levels of scale, employing homogenization as well as localization, use the *hierarchical approach to micromechanical modeling*.

The basic idea in homogenization is to find a volume element's response to a prescribed macroscopic uniform load and determining the effective properties, with the purpose of material characterization or constitutive modeling. Micromechanical constitutive modeling relates the full (homogenized) stress and strain (or strain rate) tensors to each other as well as homogenized fluxes and temperature gradients, describing the overall response for any loading condition and history. Localization procedures aim to find the local responses of the individual phases to macroscopic loading.

The stress and strain fields on the microscopic scale, $\boldsymbol{\epsilon}(\vec{x})$ and $\boldsymbol{\sigma}(\vec{x})$, respectively, are linked to the macroscopic scale in the elastic case in terms of localization relations defined [Böhm, 2002]

$$\begin{aligned}\boldsymbol{\epsilon}(\vec{x}) &= \mathbf{A}(\vec{x})\langle\boldsymbol{\epsilon}\rangle \\ \boldsymbol{\sigma}(\vec{x}) &= \mathbf{B}(\vec{x})\langle\boldsymbol{\sigma}\rangle ,\end{aligned}\tag{1.2}$$

where $\mathbf{A}(\vec{x})$ and $\mathbf{B}(\vec{x})$ are denoted mechanical strain and stress concentration tensors [Hill, 1963] and the $\langle \rangle$ brackets indicate volumetric averaging with reference to the total volume. The complementary homogenization relations read

$$\begin{aligned}\langle\boldsymbol{\epsilon}\rangle &= \frac{1}{\Omega_s} \int_{\Omega_s} \boldsymbol{\epsilon}(\vec{x}) \, d\Omega = \frac{1}{2\Omega_s} \int_{\Gamma_s} (\vec{u}(\vec{x}) \otimes \vec{n}_\Gamma(\vec{x}) + \vec{n}_\Gamma(\vec{x}) \otimes \vec{u}(\vec{x})) \, d\Gamma \\ \langle\boldsymbol{\sigma}\rangle &= \frac{1}{\Omega_s} \int_{\Omega_s} \boldsymbol{\sigma}(\vec{x}) \, d\Omega = \frac{1}{\Omega_s} \int_{\Gamma_s} \vec{t}(\vec{x}) \otimes \vec{x} \, d\Gamma ,\end{aligned}\tag{1.3}$$

where Ω_s represents the volume under consideration, $\vec{u}(\vec{x})$ is the deformation vector, $\vec{t}(\vec{x}) = \boldsymbol{\sigma}(\vec{x})\vec{n}_\Gamma(\vec{x})$ is the surface traction vector, $\vec{n}_\Gamma(\vec{x})$ is the surface normal vector to surface Γ_s and \otimes is the dyadic product of vectors. The above equations denote that the mean stresses and strains within a control volume are fully determined by the surface displacements and tractions, as long as no displacement jumps within the control volume occur, i.e. a perfect interface is assumed. Equation (1.2) is extended formally to thermo-elastic behavior as well as to the nonlinear range for elasto-plastic materials.

Due to the complexity of real microgeometries, certain assumptions about the distribution of the inclusions or approximations for the stress and strain fields as well as the concentration tensors are employed in practical cases. There are two main groups of micromechanical approaches, which are distinguished by the perspective from which the geometry of the inclusions is described. Mean field approaches (MFAs) and variational bounding methods are based on descriptions by statistical information, based on the essential assumptions that the material is statistically homogeneous. On the other hand, periodic microfield approaches (PMAs)/unit cell methods or embedded cell/windowing approaches regard discrete microstructures.

1.3.3 The Mean Field approach (MFA)

Mean field approaches obtain effective properties of inhomogeneous materials on basis of the individual phase properties and rely on phase averages of stress and strain fields, using statistical information of the microscale geometry, inclusion shape and orientation. The treatment follows [Rammerstorfer and Böhm]. Effective properties are, e.g., the overall tensors of elasticity and compliance as well as the tensor of thermal expansion. In this case in the localization relations, Eq. (1.2), the concentration tensors $\mathbf{A}(\vec{x})$ and $\mathbf{B}(\vec{x})$ are superseded by averages $\overline{\mathbf{A}}$ and $\overline{\mathbf{B}}$, which are no longer functions of the spatial variables, reading

$$\boldsymbol{\epsilon}^{(p)} = \overline{\mathbf{A}}^{(p)} \langle \boldsymbol{\epsilon} \rangle \quad \text{with} \quad \langle \boldsymbol{\epsilon} \rangle = \sum_p \xi^{(p)} \boldsymbol{\epsilon}^{(p)} \quad (1.4)$$

$$\boldsymbol{\sigma}^{(p)} = \overline{\mathbf{B}}^{(p)} \langle \boldsymbol{\sigma} \rangle \quad \text{with} \quad \langle \boldsymbol{\sigma} \rangle = \sum_p \xi^{(p)} \boldsymbol{\sigma}^{(p)} \quad , \quad (1.5)$$

where (p) indicates the respective phase and $\xi^{(p)}$ is the phase volume fraction.

Many mean field methods are based on the equivalent inclusion idea of Eshelby [Eshelby, 1957], which describes the stress and strain distribution in a homogeneous phase with a single, dilute subregion undergoing a shape or size transformation. For elastic homogeneous ellipsoidal inclusions the strain states of the inclusion are uniform for both the unconstrained as well the constrained configuration and are related to each other by the Eshelby tensor [Eshelby, 1957]. In some cases, e.g. spheroidal inclusions in an isotropic matrix, the Eshelby tensor can be evaluated analytically, compare [Rammerstorfer and Böhm; Tandon and Weng, 1988], else a numerical approach is feasible, compare [Gavazzi and Lagoudas, 1990]. Composites with inclusion volume fractions exceeding a few percent have to use mean field descriptions which take into account the interaction of inclusions, especially the effect of the surrounding inclusions on the stress and strain field of the matrix around a single inclusion. A well established approach is that of Mori and Tanaka [Mori and Tanaka, 1973], who introduced the idea of an appropriate average matrix stress which includes the perturbations due to other inclusions. Using this approach, the methodology for dilute inclusions is retained, e.g. [Benveniste, 1987]. The stress and strain in the inclusion and the newly found average matrix stress and strain are still related by the dilute concentration tensors. For pure mechanical loading this reads

$$\boldsymbol{\epsilon}^{(i)} = \overline{\mathbf{A}}_{dil}^{(i)} \boldsymbol{\epsilon}^{(m)} \quad (1.6)$$

$$\boldsymbol{\sigma}^{(i)} = \overline{\mathbf{B}}_{dil}^{(i)} \boldsymbol{\sigma}^{(m)} \quad , \quad (1.7)$$

with (i) and (m) denoting the inclusion and the matrix phase, respectively. The Mori-Tanaka type approach describes composites comprised of inclusions embedded in a matrix and agrees with one of the Hashin-Shtrikman bounds²⁾ [Weng, 1990]. The inclusions are taken to be aligned and have a unique aspect ratio, which may lie between zero (practically resembling platelets) and infinity (resembling continuous fibers). The interface between the phases is assumed to be mechanically and thermally perfect. The "standard" Mori-Tanaka method has been extended to non-aligned inclusions, e.g. [Pettermann et al., 1997], using inclusion orientation distribution functions, and to account for a thermo-elasto-plastic phase [Pettermann et al., 1999] by a tangent approach in which the constitutive relations are expressed in a rate form. The rates of the stress and strain fields are then treated analogously to the stress and strain fields. In the field of FEM with finite time increments, this tangent approach becomes an incremental one, requiring an iterative procedure. One of the advantages of an incremental approach is that it overcomes the limitation of secant methods being restricted to radial load paths, which is especially important in light of the incremental method being used as a constitutive law. The tangent tensors on the local level are generally anisotropic, which is found to give too stiff predictions for the tangent tensor on the macroscopic level, compare [Bornert et al., 2001; Gonzalez and Llorca, 2000]. Very good predictions, particularly for aspect ratios around 1, are achieved when isotropization of the local tangent tensors is enforced [Doghri and Ouaar, 2003; Pierard and Doghri, 2006]. However, while the overprediction of macroscopic strain hardening is tamed, the physical meaning behind the isotropization is not yet fully understood.

The Incremental Mori-Tanaka (IMT) approach

The employed Incremental Mori-Tanaka Method (IMT) represents an extension [Pettermann et al., 1999] of the "standard" Mori-Tanaka scheme, e.g. [Mori and Tanaka, 1973; Benveniste, 1987], within the Mean Field Approach. In the presented form it is a mi-

²⁾In case of stiff inclusions the lower bound and vice versa.

mechanics based thermo-elasto-plastic constitutive material law applicable to two-phase matrix-inclusion type composites. It serves as a material description at the integration point level within a Finite Element code in order to perform thermo-elasto-plastic analyses of composite components. The matrix is taken to behave elasto-plastically and is described by metal (J2-) plasticity with isotropic hardening. As the present version of the IMT uses the modifications proposed by [Doghri and Ouaar, 2003; Pierard and Doghri, 2006], numerical evaluation of the Eshelby tensor using the instantaneous, elasto-plastic tangent tensor of the matrix material is no longer required.

Incremental formulation

The phase averaged stress and strain rate tensors in the individual phases (p) on the microscale, $d\boldsymbol{\sigma}^{(p)}$ and $d\boldsymbol{\epsilon}^{(p)}$, respectively, are related to the macroscopic stress and strain rate tensors, $d\boldsymbol{\sigma}_a$ and $d\boldsymbol{\epsilon}_a$ by instantaneous stress and strain concentration tensors, $\overline{\mathbf{B}}_t^{(p)}$ and $\overline{\mathbf{A}}_t^{(p)}$, respectively, as well as instantaneous thermal stress and strain concentration tensors, $\overline{\mathbf{b}}_t^{(p)}$ and $\overline{\mathbf{a}}_t^{(p)}$, respectively, by the expressions

$$\begin{aligned} d\boldsymbol{\epsilon}^{(p)} &= \overline{\mathbf{A}}_t^{(p)} d\boldsymbol{\epsilon}_a + \overline{\mathbf{a}}_t^{(p)} d\vartheta \quad , \\ d\boldsymbol{\sigma}^{(p)} &= \overline{\mathbf{B}}_t^{(p)} d\boldsymbol{\sigma}_a + \overline{\mathbf{b}}_t^{(p)} d\vartheta \quad . \end{aligned} \tag{1.8}$$

The second terms on the right hand side of Eq.(1.8), $\overline{\mathbf{b}}_t^{(p)} d\vartheta$ and $\overline{\mathbf{a}}_t^{(p)} d\vartheta$, respectively, represent the thermal strain for free thermal deformation and the thermally induced stress for constrained deformation under a homogeneous temperature change. Using general relations [Rammerstorfer and Böhm], for n phases, knowledge of the mechanical concentration tensors of $n - 1$ phases as well as all constituents' properties is sufficient for obtaining all concentration tensors and describing the global thermo-elasto-plastic behavior of the two-phase composite. The effective tangent tensor of the composite can be obtained from the properties of the phases and the concentration tensors using the relations [Pettermann,

1997]

$$\begin{aligned}\mathbf{E}_t^* &= \mathbf{E}^{(i)} + (1 - \xi)(\mathbf{E}_t^{(m)} - \mathbf{E}^{(i)})\bar{\mathbf{A}}^{(m)} \quad , \\ \boldsymbol{\alpha}_t^* &= (\mathbf{E}_t^*)^{-1}[\mathbf{e}^{(i)} + (1 - \xi)(\bar{\mathbf{A}}_t^{(m)})^T(\mathbf{e}^{(m)} - \mathbf{e}^{(i)})] \quad .\end{aligned}\tag{1.9}$$

In these equations the superscripts (m) and (i) indicate the matrix and inclusion phase, respectively. $\mathbf{E}^{(i)}$ and $\mathbf{E}_t^{(m)}$ are the elasticity tensor of the inclusions and the elasto-plastic tangent tensor of the matrix, respectively. $\boldsymbol{\alpha}$ is the tensor of coefficients of thermal expansion, \mathbf{e} is the specific thermal stress tensor³⁾, $\mathbf{e} = -\mathbf{E}\boldsymbol{\alpha}$, and ξ is the volume fraction of the inclusions. A complementary formulation can be given using the stress concentration tensor instead of the strain concentration tensor. These tensors are functions of the inclusion volume fraction, the material tensors of the phases, and the Eshelby tensor, \mathbf{S}_t , which is a function itself of the inclusions' aspect ratio and the material properties of the matrix.

Implementation

The IMT is implemented into the FEM code `ABAQUS/Standard` [Simulia Inc., 2004] as a user defined material law (UMAT) [Pettermann, 1997]. The input to the incremental iterative scheme is given by `ABAQUS` by providing a strain increment. The output of the constitutive material law are stress responses and the tangent operator tensor of the composite material at the end of the increment.

Extension into the finite strain regime

The original version of the IMT is designed for small strain applications. In the light of the finite strain simulations of chapter 3, where the MMC is undergoing large deformations,

³⁾The overall stress response of the constrained material to a thermal unit load

the IMT has been extended to account for finite strains [Pettermann et al., 2006; Huber et al., 2007].

The extension of the IMT is designed to apply to metal plasticity, where in case of significant deformation the elastic strain is small compared to the inelastic one due to the elastic modulus of the matrix phase typically being orders of magnitude larger than the yield stress. This allows the use of additive decomposition of strain rates as well as the choice of use of Cauchy stress and logarithmic strain as conjugate measures. Matrix plasticity is also assumed to be the exclusive origin of the rotation of the material base reference system. For equi-axed reinforcements these rotations are assumed to be equal (in the meanfield sense). This implies that the rotation of the matrix phase is fully conveyed to the embedded linear elastic particles.

Being an analytical approach based on phase averages, the advantages of the IMT are the very low computational cost in terms of computing time as well as memory requirements when compared to the PMA. FEM simulations of entire components are possible using the IMT as a constitutive material law. Furthermore, due to the incremental formulation, complex loading conditions and arbitrary loading paths can be regarded. Mean field methods have difficulties to account for complex particle shapes, clustering⁴⁾, and size distribution effects and provide only an approximative mean value that does not fully account for the effects of local fluctuations of the stress and strain fields. One approach to predict these highly resolved fields is the periodic microfield approach.

1.3.4 Periodic microfield approach

The periodic microfield approach involves a representation of an inhomogeneous material by a model material using a periodic phase arrangement for the inclusions, the boundary

⁴⁾However, it is possible to account for clustering in a two-step approach.

conditions, the material orientations as well as the loading. Consequently the model can be regarded as extending to infinity in all directions by periodic repetition. Thus, as long as the periodicity of the above is maintained, complex microgeometries can be modeled within the restrictions of present computation capacities, implying a trade-off between generality of the geometry and the resolution of the model.

The PMA usually interprets strains and stresses as contributions from constant macroscopic ('slow') variables and periodic fluctuations ('fast' variables $\boldsymbol{\epsilon}'$, $\boldsymbol{\sigma}'$), e.g., in the form [Rammerstorfer and Böhm]

$$\begin{aligned}\boldsymbol{\epsilon}(\vec{x}) &= \langle \boldsymbol{\epsilon} \rangle + \boldsymbol{\epsilon}'(\vec{x}) \\ \boldsymbol{\sigma}(\vec{x}) &= \langle \boldsymbol{\sigma} \rangle + \boldsymbol{\sigma}'(\vec{x}) \quad .\end{aligned}\tag{1.10}$$

If the length scales are sufficiently different, it can be safely assumed that the above periodic fluctuations of stress and strain on the microlevel do not affect the macro-behavior. Inversely, variations on the macroscale cannot be regarded and consequently do not influence the microscale⁵⁾. Consequently, to fulfill Eq. (1.3), it is required that the volume integrals over fast variables vanish,

$$\langle \boldsymbol{\epsilon}'(\vec{x}) \rangle = 0 \quad \text{and} \quad \langle \boldsymbol{\sigma}'(\vec{x}) \rangle = 0 \quad .\tag{1.11}$$

Unit cell approaches for particle reinforced materials are challenged somewhat by the fact that there are no periodic geometries that are indeed elastically isotropic. To arrange realistic models for approximating statistically isotropic materials one typically has to look into unit cells containing a larger number of particles located within the cell at random positions. Loading comprises uniform far-field mechanical loads as well as uniform temperature loads. Using the Finite Element Method, unit cells are typically employed for

⁵⁾One has to make sure that these variations are indeed nonexistent or sufficiently small.

numerical investigations. As a result, periodic stress and strain microfields of high resolution are obtained at the expense of large computing times as well as considerable temporary storage requirements. These results typically also include non-linear behavior of the inhomogeneous materials. Note that in the latter case, markedly larger unit cells are generally necessary than in the elastic regime to accurately predict the material response because correlations between particles are likely to change if regions of the matrix are already plastic, thus making the matrix inhomogeneous itself and giving rise to microscopic structures considerably larger than individual particles [Rammerstorfer and Böhm].

Scale transition, boundary conditions, and load/displacement introduction

Far field stresses and strains are applied to unit cells using the master node concept [Pettermann and Suresh, 2000]. Accordingly, far-field loads or displacements are introduced to the unit cells via concentrated nodal forces or prescribed displacements at the master nodes. Employing the divergence theorem similar to Eq. (1.3) the actual load on each master node is the surface integral of the surface tractions over the face which is 'slaved' to the corresponding master node. For rectangular unit cells, the concentrated force on a node is the respective stress on a unit cell face times the area of the face. In order to apply far field strain, the displacements at the master nodes are obtained from the macroscopic strains. For the example of linear displacement–strain relations, the displacements of the master nodes in x and y direction, u and v , respectively, of the plane periodic unit cell of Fig. 1.2 are obtained by [Rammerstorfer and Böhm]

$$u_{SE} = \langle \epsilon_{11} \rangle l_{EW} \quad v_{SE} = \langle \epsilon_{12} \rangle l_{EW} \quad u_{NW} = \langle \epsilon_{21} \rangle l_{NS} \quad v_{NW} = \langle \epsilon_{22} \rangle l_{NS} , \quad (1.12)$$

with ϵ_{12} and ϵ_{21} being half the shear angles in the 12-plane and l being the unit cell dimension in the respective direction.

The complementary action within this concept is to determine the overall responses of the composite material by evaluating the reaction forces and/or displacements of the unit cells' master nodes. In general the overall stress and strain tensors within a unit cell are evaluated by volume averaging by a numerical integration scheme or by using the equivalent surface integrals from Eq. (1.3). For hexahedral cells averaged stress and strain components may be evaluated by dividing the reaction forces at the master nodes by the respective surface area and by dividing the displacements by the respective cell lengths. Direct volume averaging according to Eq. (1.3) is also performed for evaluating phase averaged quantities. The actual integration within the FEM is done by approximate numerical quadrature reading [Rammerstorfer and Böhm]

$$\langle f \rangle = \frac{1}{\Omega_p} \int_{\Omega_p} f(\mathbf{x}) d\Omega \approx \frac{1}{\Omega_p} \sum_{l=1}^N f_l \Omega_l , \quad (1.13)$$

with f_l and Ω_l being the function value and the integration point volume associated with the l -th integration point within the phase integration volume Ω_p containing N integration points. Phase averaging of non-linear functions always raises the question whether it is correct to average first and obtain the function afterwards or vice versa. There is no general rule as to accomplish this as it is, for example, inaccurate or even wrong to obtain equivalent stresses, e.g. the von-Mises stress, on basis of an averaged stress tensor. However, it is correct to average the plastic strains and obtain the accumulated equivalent plastic strain from these values.

Periodicity boundary conditions are employed so that undeformed as well as deformed states are enforced without gaps, overlaps or unphysical constraints to deformation. In practical FEM analyses, such boundary conditions are implemented in terms of equations, effectively linking three or more degrees of freedom by linear equations. For example, for a planar unit cell model corresponding points of adjacent unit cells are linked together via

$$\begin{aligned}
 u_P - u_{SW} &= u_Q - u_{SE} \\
 v_P - v_{SW} &= v_Q - v_{SE} \quad ,
 \end{aligned}
 \tag{1.14}$$

where u and v are the displacements in x and y directions, respectively, of the Master nodes (NW, NE, SW and SE) as well as the nodes P and Q, compare Fig. 1.2. Due to degradation of the band-structure of the FEM system matrix, equations in practice tend to increase computing time.

Nonlinear homogenization of periodic unit cells

The homogenization scheme is based on the displacements and reaction forces at the master nodes of a given unit cell. In this work, the *total Lagrangian* formulation is used, i.e. all entities are referred to on the initial state at $t = 0$ (the undeformed configuration). The treatment follows [Pahr, 2004].

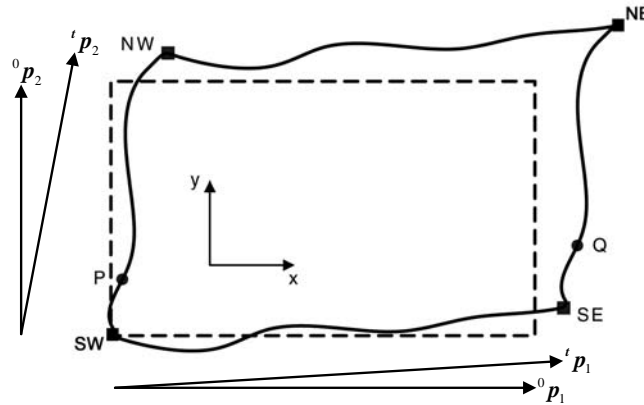


Figure 1.2: Master node positions on a plane unit cell with periodic boundary conditions in a deformed state, and vectors of periodicity of the unit cell in the undeformed ("0") and deformed state ("t").

As a "measure" of deformation within a finite strain regime the deformation gradient, $\mathbf{F} = \mathbf{F}(t)$, is used. It describes the transformation of a line element $d\vec{X}$ in the undeformed configuration to its deformed state $d\vec{x}$, reading

$$d\vec{x} = \mathbf{F}d\vec{X} . \quad (1.15)$$

For obtaining the deformation gradient in a single material point, the transformations of three linearly independent line elements are required. For unit cell simulations, these line elements ideally make up the three edges of the unit cell coincident with the position vectors of the master nodes. The three individual transformation equations can be written in a consolidated form, determining the deformation gradient from a deformed state in tensor notation via

$$\mathbf{F} = d\mathbf{x}d\mathbf{X}^{-1} , \quad (1.16)$$

if the matrices $d\mathbf{x} = [d\vec{x}_1, d\vec{x}_2, d\vec{x}_3]$ and $d\mathbf{X} = [d\vec{X}_1, d\vec{X}_2, d\vec{X}_3]$ comprise the line elements as column vectors.

In periodic unit cell analyses, the deformation gradient can be determined by the resulting displacements ${}^t_0\vec{u}_i$ of the master nodes at time t (left superscript) and referenced to the undeformed state $t = 0$ (left subscript), and the three vectors of periodicity of a three-dimensional unit cell, ${}^0\vec{p}_i$, at $t = 0$, for $i = 1..3$, compare Fig. 1.2. The periodicity vectors for time t read

$${}^t\vec{p}_i = {}^0\vec{p}_i + {}^t_0\vec{u}_i . \quad (1.17)$$

By using this scheme, the resulting deformation gradient is homogenized within the unit cell. Substituting the three line elements $d\mathbf{x}$ with the periodicity vectors ${}^t\vec{p}_i$ and $d\mathbf{X}$ with ${}^0\vec{p}_i$, Eq. (1.16) yields the deformation gradient ${}^t_0\mathbf{F}$, describing deformation at time t as

$${}^t_0\mathbf{F} = {}^t\mathbf{p} \cdot {}^0\mathbf{p}^{-1} . \quad (1.18)$$

An alternative to using the unit cells' vectors of periodicity is to use the position vectors of the master nodes.

From the master node displacement vector and the periodicity vectors, the normal vectors are derived as

$$\vec{n}_i = (\vec{p}_j + \vec{u}_j) \times (\vec{p}_k + \vec{u}_k) \Big|_{i,j,k=1,2,3} \wedge i \neq j \neq k , \quad (1.19)$$

each for the deformed and undeformed configurations. The homogenized stress tensor is then computed from the system of equations

$$\boldsymbol{\sigma} = \mathbf{H} \cdot \mathbf{n} \quad \text{and} \quad \boldsymbol{\sigma} = \mathbf{H} \cdot \mathbf{N} . \quad (1.20)$$

Here, \mathbf{H} and \mathbf{n} are the matrices of the reaction forces and normal vectors, respectively, in the sense that the respective vectors compose the column vectors of these matrices, reading

$$\mathbf{H} = \begin{pmatrix} H_{M1,1} & H_{M2,1} & H_{M3,1} \\ H_{M1,2} & H_{M2,2} & H_{M3,2} \\ H_{M1,3} & H_{M2,3} & H_{M3,3} \end{pmatrix} \quad \text{and} \quad \mathbf{n} = \begin{pmatrix} n_{1,1} & n_{2,1} & n_{3,1} \\ n_{1,2} & n_{2,2} & n_{3,2} \\ n_{1,3} & n_{2,3} & n_{3,3} \end{pmatrix} . \quad (1.21)$$

For the normal vectors in the deformed (actual) configuration, \mathbf{n} , Eq. (1.20) defines the Cauchy stress tensor, $\boldsymbol{\sigma}$. For the normal vectors in the undeformed (initial) configuration, \mathbf{N} , Eq. (1.20) yields the first Piola Kirchhoff, stress tensor, \mathbf{P} . Unlike the Cauchy stress tensor, \mathbf{P} is generally not symmetric.

One attribute of the deformation gradient is that it can be decomposed into a symmetric and a rotational part, denoted the polar decomposition, reading

$${}^t\mathbf{F} = {}^t\mathbf{V} {}^t\mathbf{R} = {}^t\mathbf{R} {}^t\mathbf{U} , \quad (1.22)$$

with \mathbf{V} and \mathbf{U} denoted as the left and right stretch tensors, respectively, and \mathbf{R} being the rigid body rotation tensor. The deformation state at t can be reached by either stretching the body with the principal stretches in the principal directions and rotating it afterwards, or by rotating first and stretching later.

The right Cauchy-Green tensor is defined

$$\mathbf{C} = \mathbf{F}^T \mathbf{F} . \quad (1.23)$$

A noteworthy attribute of \mathbf{C} is its invariance to rotation of the material base. Polar decomposition and the orthogonality of the rotation, $R^T = R^{-1}$, yield

$$\mathbf{C} = \mathbf{U}^T \mathbf{R}^T \mathbf{R} \mathbf{U} = \mathbf{U}^T \mathbf{U} = \mathbf{U}^2 , \quad (1.24)$$

because \mathbf{U} is symmetric. Every symmetric tensor can be formally denoted in terms of a spectral decomposition. For the right Cauchy-Green tensor this reads

$$\mathbf{C} = \sum_{i=1}^3 \lambda_i^2 \cdot \vec{N}_i \otimes \vec{N}_i , \quad (1.25)$$

with λ_i^2 being the eigenvalues and \vec{N}_i the eigenvectors of the respective Eigenvalue problem $\mathbf{C} \cdot \vec{N}_i = \lambda_i^2 \cdot \vec{N}_i$. A symmetric tensor of rank 2 has three real eigenvalues and three principal directions. The eigenvalues' physical meaning is the amount of stretching in direction of the eigenvectors which define the principal directions.

The Green-Lagrange strain tensor, ϵ^{GL} , is defined as

$$\epsilon^{GL} = \frac{1}{2} (\mathbf{F}^T \mathbf{F} - \mathbf{I}) . \quad (1.26)$$

By help of the displacement gradient $\mathbf{G} = \mathbf{F} - \mathbf{I}$ this can be expressed as

$$\boldsymbol{\epsilon}^{GL} = \underbrace{\frac{1}{2}(\mathbf{G} + \mathbf{G}^T)}_{\text{linear}} + \underbrace{\frac{1}{2}(\mathbf{G} \mathbf{G}^T)}_{\text{quadratic}} , \quad (1.27)$$

where the first and second summands are the linear and quadratic parts of the strain tensor, respectively.

The logarithmic strain tensor, $\boldsymbol{\epsilon}^{ln}$, is defined as

$$\boldsymbol{\epsilon}^{ln} = \ln \mathbf{V} . \quad (1.28)$$

Of course, homogenized versions of the individual strain measures are obtained by Eqs. (1.27) and (1.28) if the deformation gradient is homogenized in the first place, e.g. derived from the master node displacements of a periodic unit cell as described above.

Chapter 2

Numerical simulations of the tribological behavior of Metal Matrix Composites

Tribology is the science of interactions between contacting surfaces of bodies, moving relatively to each other. These interactions control friction and wear, two important processes with impact on economic reasoning and long-term reliability. On the one hand, tribological knowledge is important for the designer aiming at the reduction of friction and wear¹⁾. On the other hand, it is important for the manufacturer to understand the tribological background of unwanted friction or excessive wear, in the interest of energy saving, equipment uptime, or life expectancy. Although ‘conventional’ tribology is well established, the development of new materials requires the understanding of underlying tribological processes.

¹⁾unless brake systems are to be designed, which require higher coefficients of friction

2.1 Tribology basics

2.1.1 Literature review

The importance of contact problems in the field of mechanics is founded in the fact that contact is one of the most frequently deployed methods of applying loads to a structure or a body. One unpleasant attribute of contact are unilateral inequalities, which are used to eliminate tensile tractions at and material penetration of contacting surfaces. If a point is not in contact, its gap, g , to the counterbody is positive and the contact pressure, p , is zero²⁾. If the point is indeed in contact, the gap is zero per definition and results in a positive pressure, reading

$$g > 0, \quad p = 0, \quad \text{and} \quad g = 0, \quad p > 0 \quad . \quad (2.1)$$

The system of inequalities of Eq.(2.1) serve to determine the points of a surface which are in contact. In case of a prescribed contact area, the uniqueness of the solution for linear elastic material has been proved by [Fichera, 1972]. As only relatively simple contact problems can be treated analytically, numerical methods have evolved and appropriate algorithms are included in most commercial finite element codes, e.g. [Simulia Inc., 2004]. A discussion on numerical algorithms is found in [Kikuchi and Oden, 1988].

Consideration of friction introduces additional conditions. According to the Coulomb friction condition [Simulia Inc., 2004; Johnson, 1992]

$$\tau_{eq} < \tau_{crit}, \quad \tau_{crit} = \mu p \quad , \quad (2.2)$$

there are two states possible for any point within a contact area. First, the stick condition (no relative motion), where the magnitude of tangential traction, τ_{eq} , is less than the product of the coefficient of friction (COF), μ , and pressure, p . Secondly, the slip condition

²⁾Except when adhesion is considered

(relative motion), where the tangential traction is defined μp . Even though Coulomb friction is apparently simple, it is difficult to deal with analytically. It certainly helps that a quasi-static solution can be achieved in many cases where the loading rate is sufficiently low. In this case the tribological system passes a series of equilibrium states. Sometimes it is possible to further reduce the problem to a static one for monotonic and proportional loading. Frictional dissipation at the contact surface also introduces heat into the system, resulting in a thermomechanical problem. If the dependence of the stress field on the thermal distortion is zero or low, this can be solved sequentially. In this case, the heat transfer problem is solved first and the resulting temperature solution is placed into a stress analysis as a predefined field. Otherwise, a fully coupled thermomechanical problem has to be solved simultaneously for both the displacement and the temperature degrees of freedom.

If a thermo-elastic problem is driven by frictional heat generated during sliding, the temperature field at the contacting surface can lead to thermo-elastic instability, giving rise to wear and other possibly undesired effects. Instabilities of this kind are often found in brake or clutch systems and are known as frictionally excited thermo-elastic instabilities (TEI) [Barber, 1969]. A critical sliding speed above which the system is unstable was found analytically by [Dow and Burton, 1972], who investigated the effect of a small perturbation on the uniform temperature (or pressure) solution and its growth in time. Recently, similar work was done by [Ciavarella and Barber, 2005], who determined the stability range including a pressure dependent thermal contact resistance and its effect on the frictionally excited TEI.

2.1.2 Surfaces

A keyword for tribology is *surface*. Since the interaction takes place on surfaces, the composition and state of the involved surfaces as well as the surface near material are of great influence on the tribological behavior of the system, affecting contact, friction, and wear.

A solid surface has complex structures and properties depending on the nature of the bulk material, the method of preparation affecting the surface geometry, and the interaction between the surface and the environment. The problem with surfaces in tribological processes is that during experiments, one cannot observe the contact faces during the interaction³⁾, which makes it necessary to rely on the examination of the surfaces' states before and after interaction.

An additional problem is that surface layers contain zones dependent on the bulk material and forming processes, which can have properties entirely different from the bulk material (e.g. lightly and heavily deformed layers, chemically reacted or chemi- and physisorbed layers). With exception of noble metals, all metals and alloys (and many nonmetals) form oxide layers in air or layers of nitrides, sulfides, and chlorides in other environments.

Surface roughness

Surface texture is the deviation (random or periodical) from the nominal surface which includes roughness, waviness, lay, and flaws. Short wavelength roughness is denoted micro-roughness, whereas waviness (macro-roughness) describes longer wavelengths of asperity spacing. Lay describes the existence of a principal direction of a predominant surface pattern, and flaws are randomly distributed, singular deficiencies of the surface.

2.1.3 Friction

Overview

Friction commonly refers to a force resulting from sliding, responsible for an energy transformation in the process, since surfaces in contact usually transmit shear as well as normal forces across the interface. Generally, there is a correlation between these two force com-

³⁾except maybe in experiments involving glass as one tribological partner

ponents. The ‘magnitude’ of friction is often expressed in terms of the COF, μ , which is given by the frictional force, F , divided by the load, W , pressing two surfaces together, Eq. (2.3). W is referred to as normal or applied load.

$$\mu = \frac{F}{W} \quad . \quad (2.3)$$

Note that expressing friction by using a coefficient does not imply the latter to be an intrinsic feature of the contributing materials. Every sliding condition produces a different COF, because of alteration of the participating surfaces over time. Surfaces (especially metals) tend to oxidize in air, some hydrolyze, or gases are attracted to adsorb. ‘Contaminants’ (like water vapor, oil vapor or simply fingerprints) may settle and change the friction properties considerably. Adsorption and oxidation of solid substrate surfaces takes place within a time frame of about 10^{-8} s to 10^{-7} s. Consequently, it is difficult to find values of COFs in publications, which are applicable for the frictional situation and environment at hand. Most published values have been determined in controlled environments and narrow ranges of relevant parameters. Although data is usually reliable and reproducible, it applies only to the environment used within the test. Often only a fixed (single) value for the COF is given, e.g. 0.2 for (dry) steel against a steel counterbody, neglecting that one can measure values ranging from 0.1 to 1.2, depending on the sliding conditions and environmental influences mentioned above.

Ranges of coefficients of friction

General ranges of coefficients of friction can be defined more easily than absolute values, e.g. [Bhushan, 2001]:

- $\mu < 0.1$ = very low friction — achievable either by rolling or by elastic contact between surfaces that have low adhesive force between them

- $\mu = 0.1 \dots 0.2$ = low friction — achievable by fluid film lubrication⁴⁾
- $\mu = 0.2 \dots 0.8$ = intermediate friction — usually found with moderately hard materials not carefully cleaned
- $\mu > 0.8$ = high friction — with soft, well cleaned metal parts

Since plastic deformation will appear in measurements as an increase of the COF, one important condition for low friction is that the asperities should not be loaded beyond the elastic limit. Plastic flow in the asperities appears if the traction exceeds this limit. In this case asperities are likely to be stretched in the direction of sliding, resulting in a rougher surface, on average, than before. Loosened particles located at the sliding interfaces can also be the reason for an increase or decrease of the COF. Oxides especially on metals may come loose during sliding and over time bulk material is removed as well, either by adhesive tearing or by fatigue failure. Grains of ceramic material are more likely to be loosened because of the weaker bonding.

2.1.4 Frictional heating

During sliding, mechanical energy is transformed into internal energy or heat [Bhushan, 2001]. As a result, the temperatures of the involved bodies increase. It is known that frictional heating is concentrated within the real area of contact of the bodies in relative motion. Theories exist that frictional heating occurs by atomic-scale interactions within the top atomic layers on the contacting surfaces [Landman et al., 1993], whereas other investigators state that the energy dissipation takes place in the bulk material beneath the contact region by plastic deformation processes [Rigney and Hirth, 1979]. Nevertheless, there is a common agreement that nearly all of the energy dissipated in frictional contacts is transformed into heat which is entirely⁵⁾ conducted into the contacting bodies at the

⁴⁾note that this represents a different mechanism, which is not considered in this work

⁵⁾if convection and/or radiation effects can be neglected

actual contact interface, e.g. [Uetz and Föhl, 1978].

2.1.5 Heat conduction and partitioning

Analytical analysis

Assuming all energy is dissipated as heat on the sliding surface due to friction, the rate of heat generated per unit area, \dot{q}_{diss} , reads

$$\dot{q}_{diss} = \mu p v \quad (2.4)$$

where μ is the COF, p the contact pressure and v is the (scalar) relative sliding velocity. If μ , p , or v vary over the considered contact area, a appropriate differential condition has to be used. A certain fraction of \dot{q}_{diss} enters each of the contacting bodies and induces either a heat conduction problem within the bodies, a convection problem in case of interaction with the environment, a temperature rise of the body, a radiation problem, or a combination thereof. Heat conduction, convection and radiation problems may be treated quasistatically in the steady state, whereas heating up of a body is a transient process per se.

The conduction of heat within a body is described by the Fourier equation

$$-k \cdot \text{grad } T = \dot{q} \quad (2.5)$$

with k being the thermal conductivity, T the temperature, and \dot{q} the heat flux within the regarded solid. If one-dimensional variation of temperature is assumed, Eq. 2.5 is reduced to

$$-k \frac{dT}{dx} = \dot{q} \quad (2.6)$$

The task of a thermal analysis is to determine the solution of the appropriate equation above subject to thermal boundary conditions which include the heat generation equation (2.4).

In a frictional problem, two bodies have to be considered. Analytical calculation of their temperatures requires determination of the partitioning of frictionally dissipated heat between the contacting bodies. The totally generated heat in the interface, \dot{q}_{diss} , Eq. (2.4), is partitioned into the individual heat fluxes \dot{q}_1 and \dot{q}_2 , respectively, entering body 1 and 2, compare Fig. 2.1. The global heat balance reads

$$\dot{q}_1 + \dot{q}_2 = \dot{q}_{diss} = \mu p v \quad . \quad (2.7)$$

Definition of a heat partition factor ζ as

$$\zeta = \frac{\dot{q}_1}{\dot{q}_{diss}} \quad \text{and} \quad 1 - \zeta = \frac{\dot{q}_2}{\dot{q}_{diss}} \quad (2.8)$$

yields

$$\dot{q}_1 = \zeta \mu p v \quad \text{and} \quad \dot{q}_2 = (1 - \zeta) \mu p v \quad . \quad (2.9)$$

Note that the heat partitioning factor is generally a function of position since both \dot{q}_1 and \dot{q}_2 may vary with position, which is not reflected in these simple equations. Even the dissipated heat flux can vary within the contact patch since the contact pressure and/or

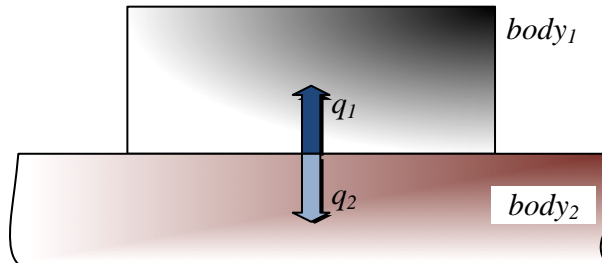


Figure 2.1: Heat fluxes into bodies 1 and 2, respectively, due to frictional heat dissipation at the contact interface.

relative sliding velocity are not necessarily constant.

There are analytical solutions available for the heat partition function using heat source methods, which mostly are iterative solutions based on matching the surface temperatures of the two contacting bodies at all positions within the contact area⁶⁾. Due to the complexity of these solutions, numerous approximate solutions for the heat partition function exist, often assuming the heat partitioning to be constant.

Numerical analysis

Many FEM codes facilitate the solution of heat conduction problems. However, in FE simulations, contrary to analytical solutions, no heat partitioning function needs to be evaluated. In ABAQUS, only an initial estimate is required as an input from the user. The temperature distribution in both bodies is then subject to the boundary conditions applied to the model as well as the thermophysical material properties, resulting in a natural flow into the contacting bodies. The boundary conditions, in terms of temperatures or heat fluxes (including the heat source due to frictional dissipation located at the interface) are responsible for conducting the heat out of the system. In case of simulations with the counterbody being a rigid body the heat flux into the MMC is stipulated by a defined partitioning factor.

2.1.6 Wear

Wear is defined as the material removal from a surface due to interaction with another surface. It is measured in terms of *wear rate*, which is defined as wear volume per sliding distance, or in terms of *specific wear rate*, which is defined as wear volume per sliding distance and load.

⁶⁾If contact is assumed to be ‘perfect’, no temperature jump should be expected across the contact interface within the real area of contact.

Wear rates can vary over several orders of magnitude, depending on the operating conditions and materials selection, which suggests that influence on the latter is a key element for controlling wear. Since wear is a complex system dependent on many variables, wear rate over a range of test conditions is typically described by multiple wear maps, see e.g. [Poletti, 2005]. These maps may also contain the change of dominant wear mechanisms corresponding to the loading situation.

There exist different fundamental types of wear mechanisms (Fig 2.2) [Bhushan, 2001]. *Adhesive* wear is characterized by adhesion at the contact interface being high enough to resist sliding. Two different modes can be identified under large deformation as flake (or tongue) forming mode and a wedge forming mode (Fig 2.3). *Abrasive* wear is characterized by surface material removal by abrasive grooving on the surface of the material with less hardness. For ductile materials, three different modes can be identified as cutting mode, wedge forming mode, and ploughing mode (Fig 2.4), whereas for brittle materials, wear particles are generated by crack propagation. Fatigue and corrosive wear will not be discussed.

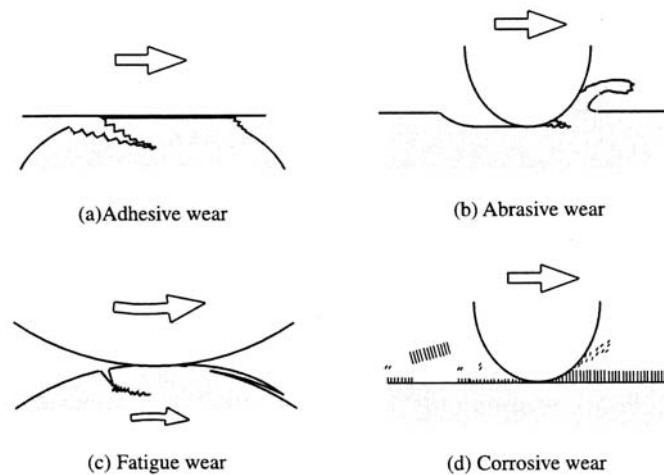


Figure 2.2: Sketch of the four fundamental wear modes [Bhushan, 2001].

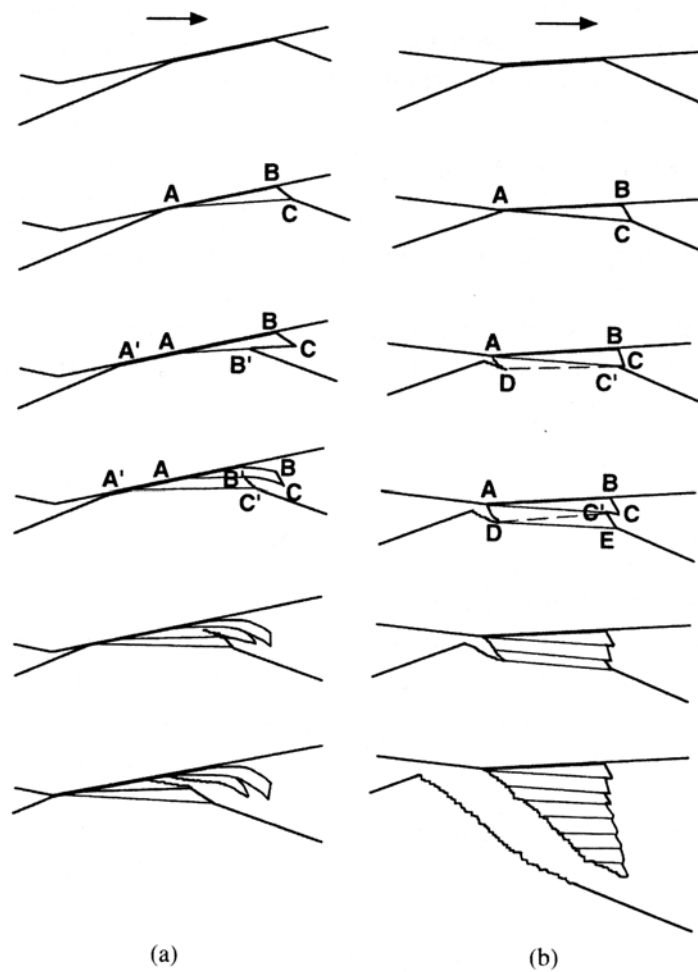


Figure 2.3: Schematic adhesive transfer process during wear: adhesive transfer of a thin flake-like particle (a), a wedge-like particle (b) [Bhushan, 2001].

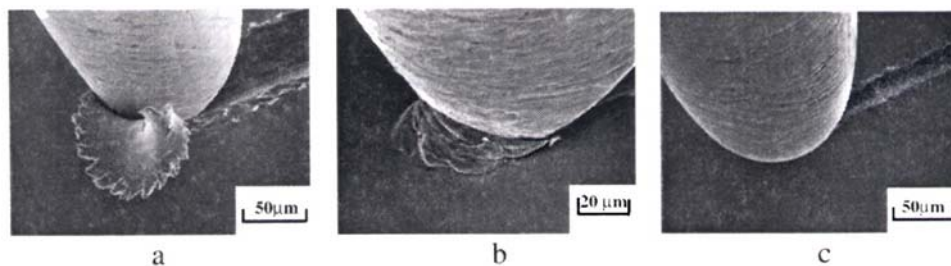


Figure 2.4: Three different modes of abrasive wear observed by SEM: (a) cutting mode ; (b) wedge forming mode; (c) ploughing mode [Bhushan, 2001].

2.2 Experimental test setup

To provide input for certain process parameters in the analytical calculations as well for the FE analyses, standard *pin-on-ring* tribological experiments are performed by cooperation partner *Austrian Research Centers Seibersdorf (ARCS)*. The test arrangement involves a pin (diameter 4mm) pressed against a ring (diameter 55mm), which is spinning at varying speeds for the different measurements. Weights acting on the pin are used for realizing different, globally constant contact pressures. A sketch as well as a photograph of the test setup are shown in Fig. 2.5 and Fig. 2.6, respectively. Pin temperatures denoted as $T_{2.5}$ and $T_{7.5}$, respectively, are measured at distances of 2.5mm and 7.5mm from the contact surface. Since these distances decrease during experiments due to wear, a small (linear) shift in time of the temperature profile along the axis of the pin with respect to the (also measured) linear wear takes place. The shift is accounted for in experiments with both high global contact pressure and sliding speed.

Additionally, a thermographic camera is employed to determine the temperature in the vicinity of the contact surface as well as the global temperature of the ring, T_{Ring} . A frame of the recording is exemplarily shown in Fig. 2.7 (courtesy of *Austrian Research Centers Seibersdorf*). Indicated are also the windows of measurement of the thermal probes.

Other important measured quantities apart from the pin temperatures are the global COF, μ_{eff} , and ring temperature, T_{Ring} . For the present investigations, only the *global* temperature of the ring is of interest. Consequently, the measurement is taken at a sufficient distance away from the sliding track to ensure a point of the body with no (or very small) spatial temperature gradient. Although there is heating up on the sliding track of the ring it is limited spatially and decays long before the same spot on the track reaches the contact area again.

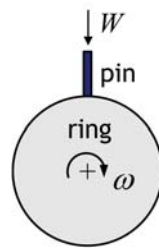


Figure 2.5: Schematic of a pin-on-ring experiment; the force pressing the pin onto the ring is denoted W , the ring is spinning with angular velocity ω .

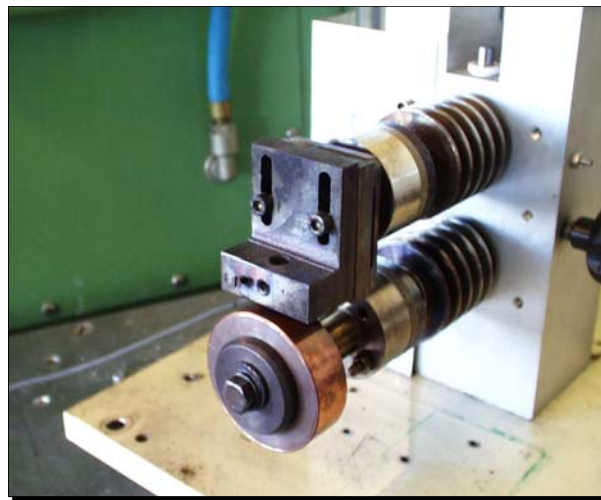


Figure 2.6: A photograph of the pin-on-ring test arrangement [Poletti, 2005].

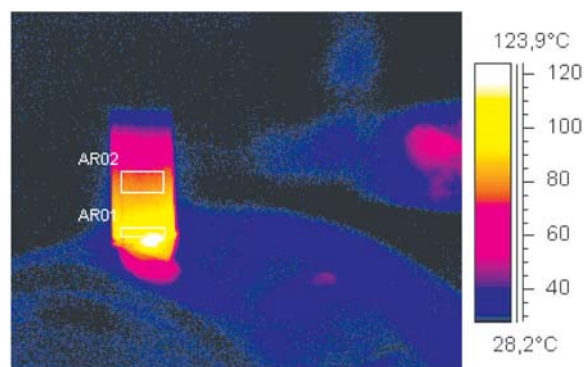


Figure 2.7: A frame of the recording of the thermographic camera. Also indicated are the windows of measurement AR01 and AR02, respectively, referring to the location of the thermal probes.

2.3 Influence of different volume fractions and particle distributions on the frictional response to a macroscopic frictional load

The objective in this part of the thesis is, on the one hand, the prediction of the macroscopic coefficient of friction. On the other hand, the mesoscopic and microscopic response is predicted in terms of stress and strain distributions as a result of frictional loading of an inhomogeneous material. The influence of different particle volume fractions as well as distributions in the form of clustering of inhomogeneities is treated. The motivation behind modelling clusters is that the "real" materials indeed do not exhibit perfect random distribution of particles, but have a tendency to develop clustering of inclusions, compare Fig. 2.8.

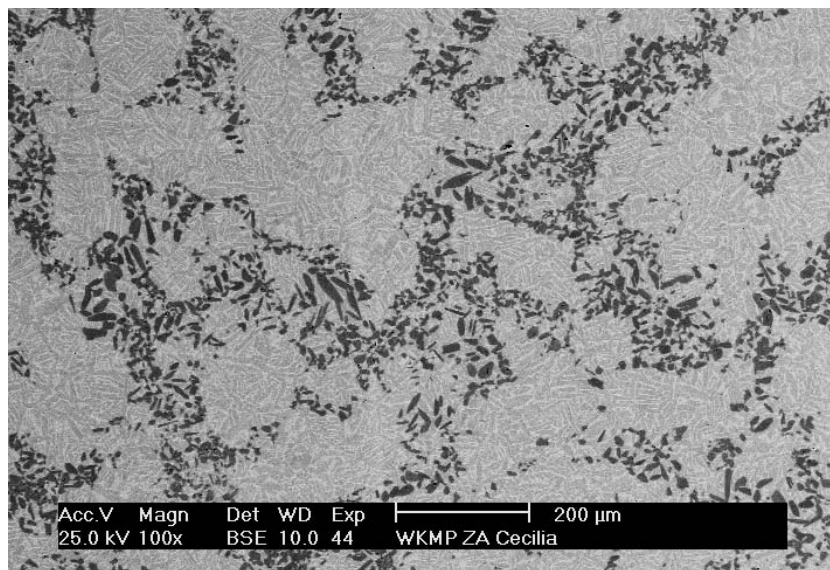


Figure 2.8: Scanning-electron microscope image of the distribution of the particles in a material; matrix(light), particles(dark) [Poletti, 2005].

2.3.1 Modeling approach

A modified periodic microfield approach is used to investigate the mechanical and thermal response of a composite material. The modification results from allowing a free surface as the contacting surface, not establishing periodicity conditions in this direction. The macroscopic frictional loading is realized by pressing a counterbody onto a unit cell and enforcing relative motion by prescribed sliding of the counterbody.

Plane rectangular multi-inclusion unit cells represent the MMC by modeling various distributions of particles embedded in a matrix phase. The cells are based on the works of [Segurado et al., 2001]. The finite element model for the basic configuration with 30%vol inhomogeneities in a random distribution is shown in Fig. 2.9. The unit cells' length and height are 16mm and 7mm, respectively.

The tribo-surfaces of the cells show cut particles and allow for interaction with the counterbody. At the two lateral sides the periodic matrix-inclusion geometry is forced to deform periodically and to show equal temperature fields by applying appropriate coupling equa-

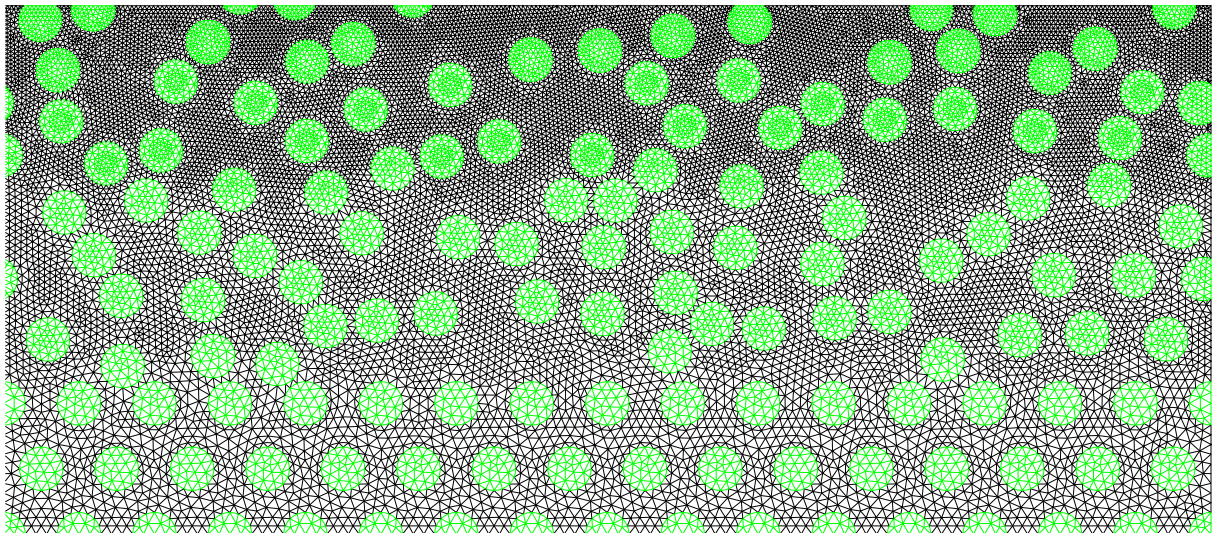


Figure 2.9: Finite element unit cell model with a homogeneous random distribution of 30%vol inhomogeneities; matrix(dark), particles(light);

tions. The temperature as well as the deformations are fixed at the bottom surface because from [Segurado et al., 2001] it is evident that the extra effort in special arrangement of particles and boundary conditions for this model edge is not necessary, as perturbations of the stress or strain fields on the contact surface decay quickly. Plane stress assumptions are used. While plane stress models are typically more compliant and plane strain models exhibit a stiffer behavior than 3D-approaches, the difference in the response regarding the COF between both planar models using the original cells have been small [Segurado et al., 2001]. The matrix material as well as the circular particle domains are taken to behave thermo-elastically. A perfect mechanical and thermal interface between the matrix and its inclusions is assumed. The counterbody is modeled by a rigid body with no temperature degree of freedom and, consequently, receives no heat during the simulations. It is assumed that the entire frictionally dissipated heat enters the unit cell (which is in contrast to subsequent simulations in the next sections where the counterbody gains the ability to participate in the heat transfer). Each phase has its individual coefficient of friction with respect to the counterbody. The cells are loaded by applying a macroscopic contact pressure via the tangentially sliding counterbody. The sliding distance is chosen such that a steady state is reached in all cases. It is assumed that all energy from the frictional contact is transformed into heat which is conducted into the contacting bodies at the actual contact interface, according to a stipulated, constant global heat partitioning factor. Surface roughness is not directly accounted for but character and condition of the surfaces are regarded in the local COF of the respective contact pair. Loosened particles or third body abrasion as well as effects thereof will not be considered in this work.

The Finite Element program ABAQUS [Simulia Inc., 2004] is used for the simulations. Six-node modified plane stress elements with degrees of freedom for displacements and temperatures are used for the simulations. Their modification consists of providing two additional displacement variables and one additional temperature variable [Simulia Inc., 2004]. The reason for this choice lies in the problem of second order elements to reproduce contact

pressure without the help of a midpoint node⁷⁾ [Simulia Inc., 2004]. Element based surface to surface contact using the master-slave concept is employed. As it is modeled as rigid, the counterbody contact surface is the natural choice for the master surface. The simulations are generally divided into several steps, with the first one dedicated to the establishment of the contact pressure, and the subsequent steps for the sliding process. A steady state is reached quickly within the first two or three increments of the sliding step, as can be checked for example in the lateral reaction force on the counterbody, the stress and strain states, the contact pressure distribution as well as the temperature distribution on the contact surface. As contact problems generally produce non-symmetric system matrices, the unsymmetric solver of **ABAQUS/Standard** is invoked. For the constraint enforcement method, the Augmented Lagrange method is employed [Simulia Inc., 2004]. Using this approach, interpenetration of contact surfaces exceeding a certain tolerance calls another series of iterations where the contact pressure is 'augmented' until convergence is achieved again, i.e. the actual penetration is less than the tolerance parameter. The Augmented Lagrange method requires additional iterations and is essentially an approximation compared to direct methods which strictly enforce a given pressure-overclosure behavior using the inequalities Eq.(2.1). However, this contact enforcement method is employed to avoid overconstrained problems where convergence cannot be achieved with the direct or penalty methods. Vertices which are both members of contact conditions as well as periodic boundary conditions have to be removed from the multipoint constraints in lateral as well as vertical direction in order to avoid overconstraints at these nodes⁸⁾.

The rigid counterbody uses the same element type as the MMC model, but with no temperature degrees of freedom, as the entire dissipated heat is attributed to the MMC anyway. By mapping the master surface nodes of the master-slave contact pair onto the reference point of the counterbody, the global contact force is obtained. The lateral component of

⁷⁾For example, a constant pressure applied to the face of a second-order element, which does not have a midface node, produces consistent nodal forces at the corner nodes acting in the opposite sense of the pressure.

⁸⁾This involves the nodes NW and NE of the unit cell, compare Fig. 1.2

this force is used to determine the global COF by Coulomb's law.

Varying volume fraction and modeling clustering

The region where particles are to be masked into the matrix randomly⁹⁾ can be chosen on the basis of a numbering scheme. With this procedure, it is possible to model various particle distributions while maintaining randomness. For example, variation in the volume fraction maintaining random positioning of the inclusions and accumulation of particles in certain regions by deserting adjacent areas is modeled for the simulations.

2.3.2 Example

Investigations are carried out in order to predict the frictional behavior of Ti-matrices reinforced by TiC-particles. The Young's moduli, Poisson's ratios, coefficients of thermal expansion, thermal conductivities, and coefficients of friction against steel are listed in Table 2.1. Temperature-dependent data is not considered in the simulations. The reference temperature for the temperature rise is (arbitrarily) set to zero degrees.

The simulations are performed for 30%vol and 10%vol, respectively, homogeneous, randomly distributed as well as for 10%vol clustered configurations, compare Fig. 2.10.

An overall contact pressure of 1MPa and a sliding speed of 2mm/s are used for the simulations.

⁹⁾by assigning matrix properties to the corresponding element sets

Table 2.1: Thermomechanical properties of matrix and particles

		Matrix	Particles
Young's modulus	[GPa]	103	440
Poisson's ratio	[-]	0.3	0.19
Coeff. of therm. expansion	[1/K]	9.6E-06	8.0E-06
Thermal conductivity	[W/mK]	6.5	18
Coeff. of friction against steel	[-]	0.33	0.6

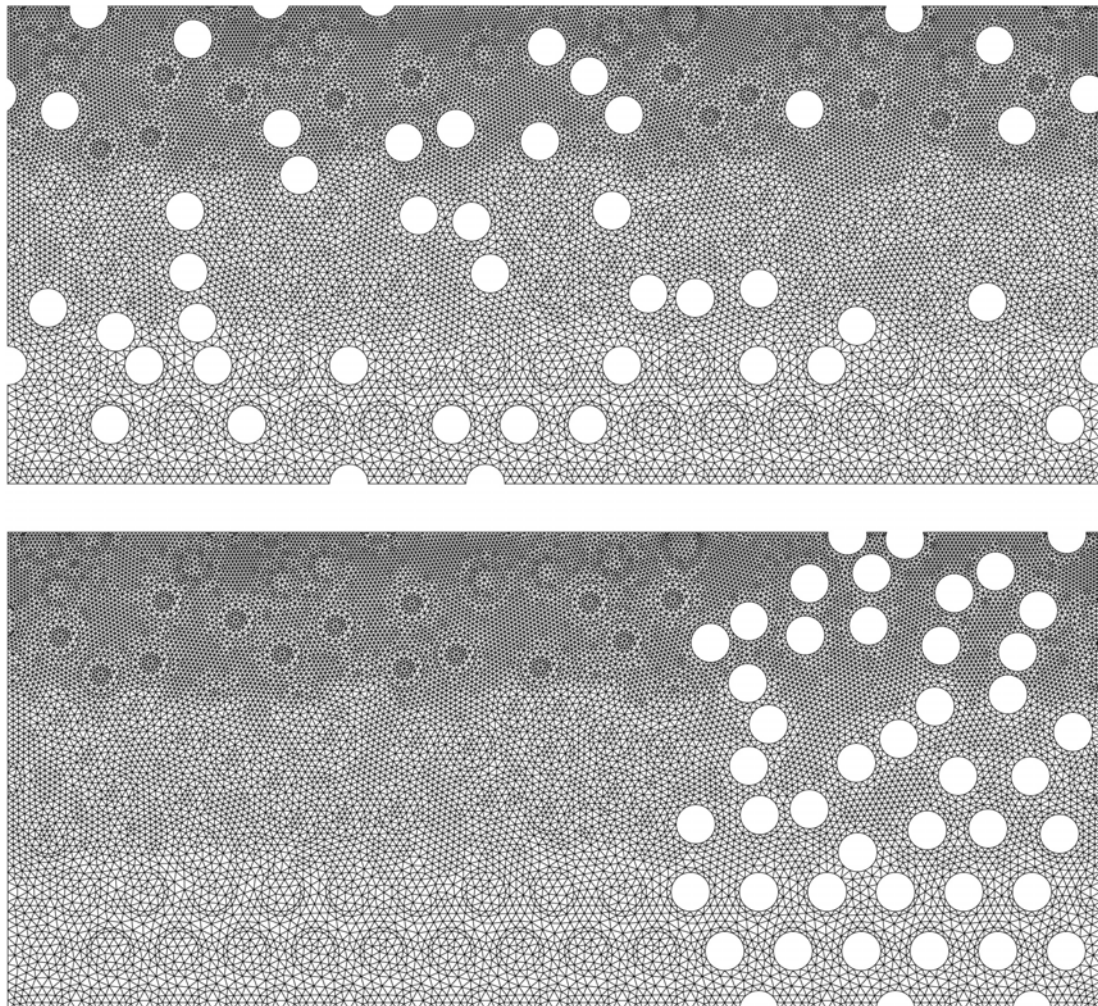


Figure 2.10: Unit cell models with homogeneous (top) and clustered (bottom) distribution of 10%vol particles.

2.3.3 Results

Contact pressure and surface traction distribution.

The thermomechanical interaction at and underneath the tribo-surface determines the local contact pressure distribution and, hence, the local frictional forces. The inhomogeneous microgeometry generates fluctuation of the contact pressure at the contact surface, compare Fig. 2.11. The frictional traction distribution is not shown as it is equivalent and only multiplied by the local COF, accordant to Coulomb's law. Stress peaks at the particle to matrix interface are singularities¹⁰⁾ caused by modeling a "perfect" mechanical and thermal interface using a single node¹¹⁾. For the chosen sliding direction, positive pressure peaks are caused by transition from a softer to a stiffer material and vice versa.

Figure 2.12 (left) shows the predicted contact pressure over the contact surface for the 10%vol clustered configuration in the steady state condition. In the reinforced region, high fluctuations are caused by individual particles. Due to the higher stiffness of this region, the cluster average is higher than the global value of the contact pressure, which is unit pressure due to the global equilibrium condition. Note that the results are not strictly periodic because the master nodes NW and NE are members of the contact surface and consequently have to be taken out of the periodicity equations to avoid overconstraints.

¹⁰⁾The order of the singularities can be determined by, e.g. [Bogy, 1971].

¹¹⁾Using two nodes would require knowledge of the interface properties.

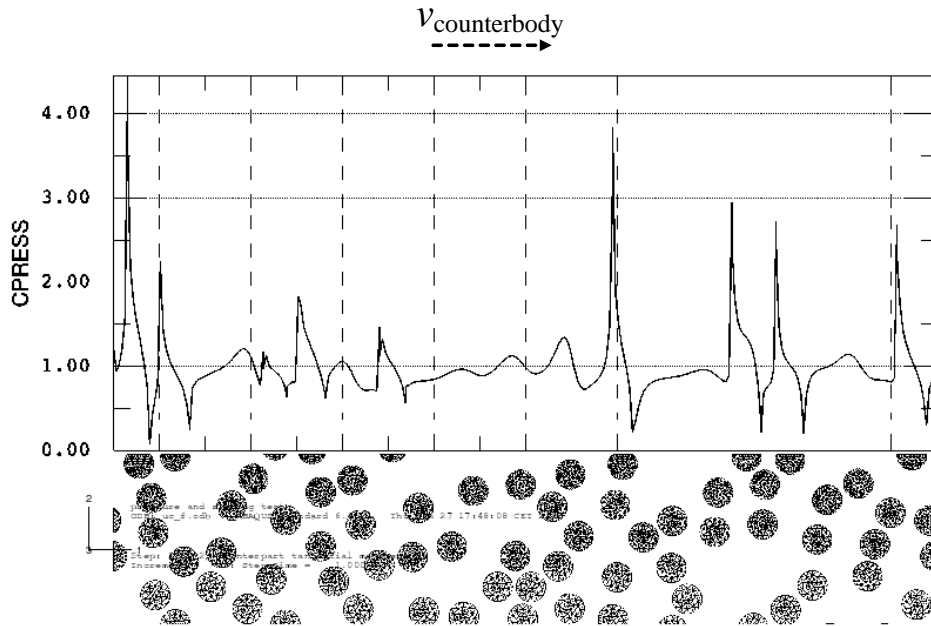


Figure 2.11: Contact pressure distribution on the surface of the 30%vol homogeneous, randomly distributed configuration, for an overall contact pressure of 1MPa and sliding speed 2mm/s.

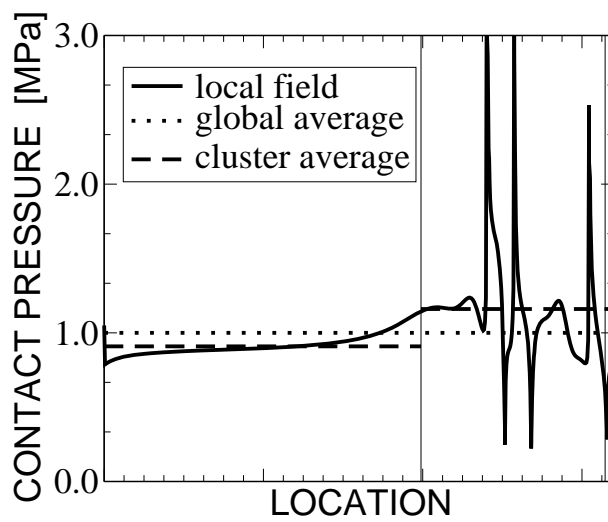


Figure 2.12: Predicted contact pressure for the 10%vol clustered configuration, for an overall contact pressure of 1MPa and sliding speed 2mm/s.

Stress state underneath the surface.

The contact interaction at the surface, a combination of unit pressure and sliding, is transferred into a complex stress and strain state inside the unit cell on the microscale, owing to the inhomogeneous micro-topology [Segurado et al., 2001]. Due to the higher stiffness of particles in contrast to the matrix of the present material, "stress bridges" are developing in the matrix in regions where particles are queuing. For example, Fig. 2.13(top) shows the distribution of the von Mises stress in the steady state. Stress concentrations develop especially in areas of particles having short mean free paths in the direction of the minimum (in-plane) principal stress. For a detail where these stress bridges in the matrix between adjacent particles are pronounced compare Fig. 2.13(bottom). In these regions, the magnitude of stress concentration, in terms of the von Mises stress over the applied pressure, $\sigma_{VM}^{(m)}/p$, is up to 2.5. Consequently, even for an assumed global contact pressure considerably lower than the yield limit of the matrix, plastic yielding¹²⁾ is introduced locally in the matrix of the inhomogeneous material.

Since the stiffer particles attract most of the load, the 10%vol clustered configuration has an increased meso stress level compared to the 30%vol distribution, because the same load is distributed to fewer particles. This is also reflected in the principal stresses in the particles, compare Fig. 2.14. As this plane problem is dominated by compression, the minimum (in-plane) principal stress is the critical one.

Note that the influence of the free surface decays relatively quickly within the unit cell. Variations of the contact pressure or the surface temperature from the homogeneous distribution decay within a third of the unit cell height, which can be observed also in Fig. 2.15.

¹²⁾not considered in these elastic simulations

Global coefficient of friction.

The predicted macroscopic coefficients of friction are listed in Table 2.2. As the local COF as well as the Young's modulus of the particles is higher, the global COF has a tendency to increase with the particle content. Its value is also influenced by the distribution of particles, but the difference between clustered and homogeneous random configurations with the same volume fraction is small. It is noted that the results for the COFs are not the same compared to derivations from a simple rule of mixture on the macroscopic level.

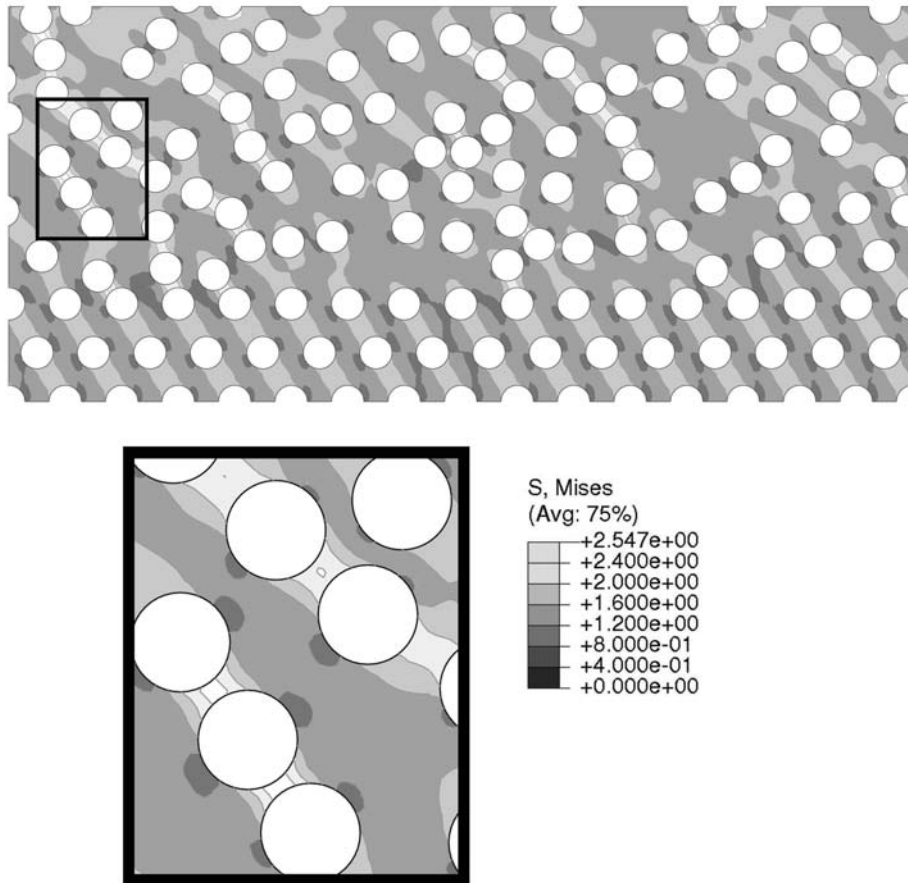


Figure 2.13: The von-Mises stress distribution (top) for an overall contact pressure of 1MPa and sliding speed 2mm/s; stress concentration in area of particles having short mean free paths in the direction of the minimum (in-plane) principal stress (bottom).

Global thermal conductivity.

The global thermal conductivity is determined from the FE simulations by the relation

$${}^{uc}k = \frac{\bar{q} h}{\bar{T}_o - \bar{T}_u} , \quad (2.10)$$

with \bar{q} being the average heat flux within the unit cell which, owing to the lateral periodic boundary conditions, has only a vertical component. $\bar{T}_o - \bar{T}_u$ is the global temperature

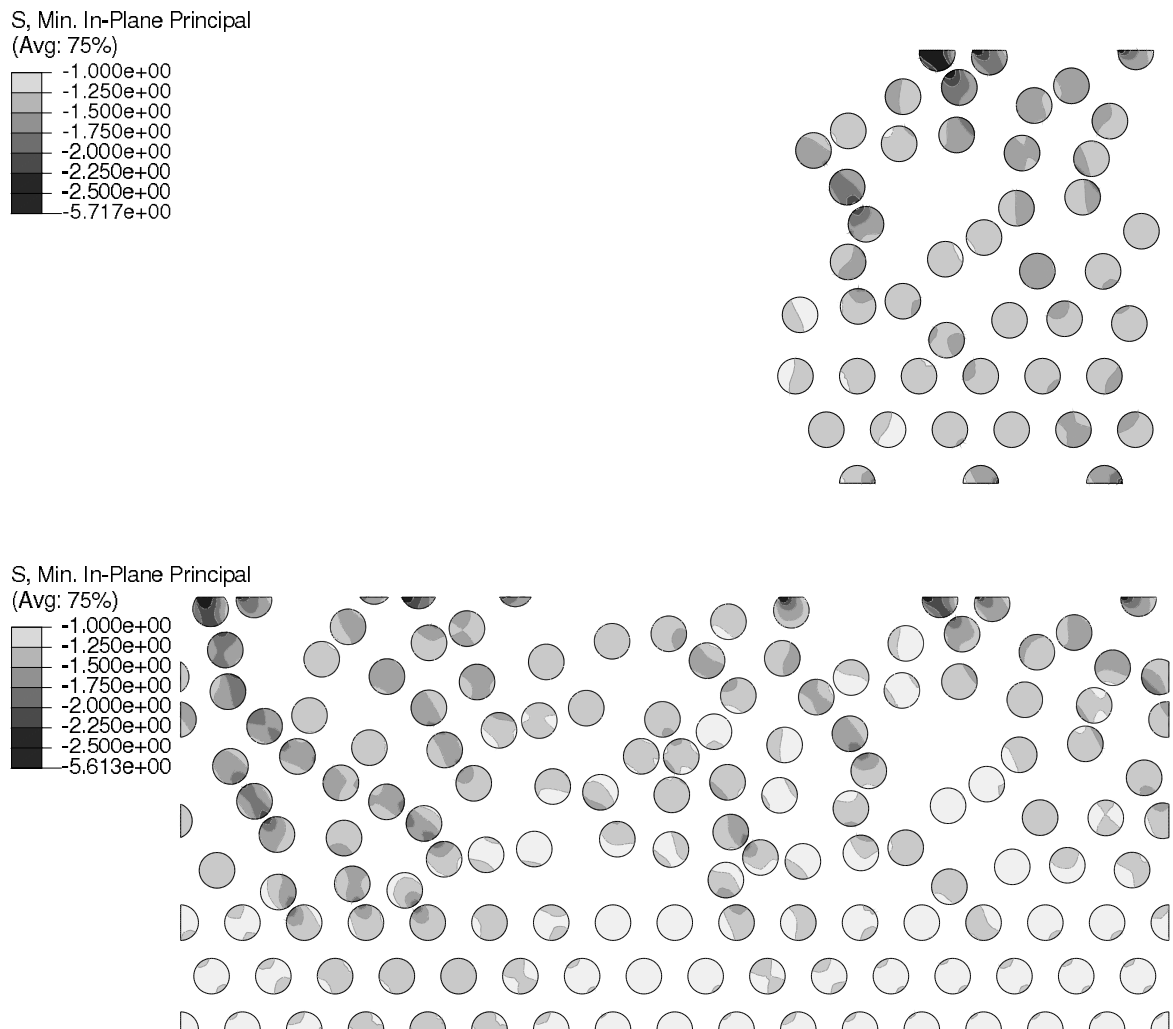


Figure 2.14: Distribution of the minimum (in-plane) principal stress in the particles, for the 10%vol clustered (top) and the 30%vol random configuration.

difference over the vertical unit cell dimension, h , in the steady state. The global heat flux and temperatures are determined by integrating all respective contributions on the contacting surface, e.g. for the heat flux this reads

$$\bar{q} = \frac{1}{A} \int_A \dot{q}(x) dA , \quad (2.11)$$

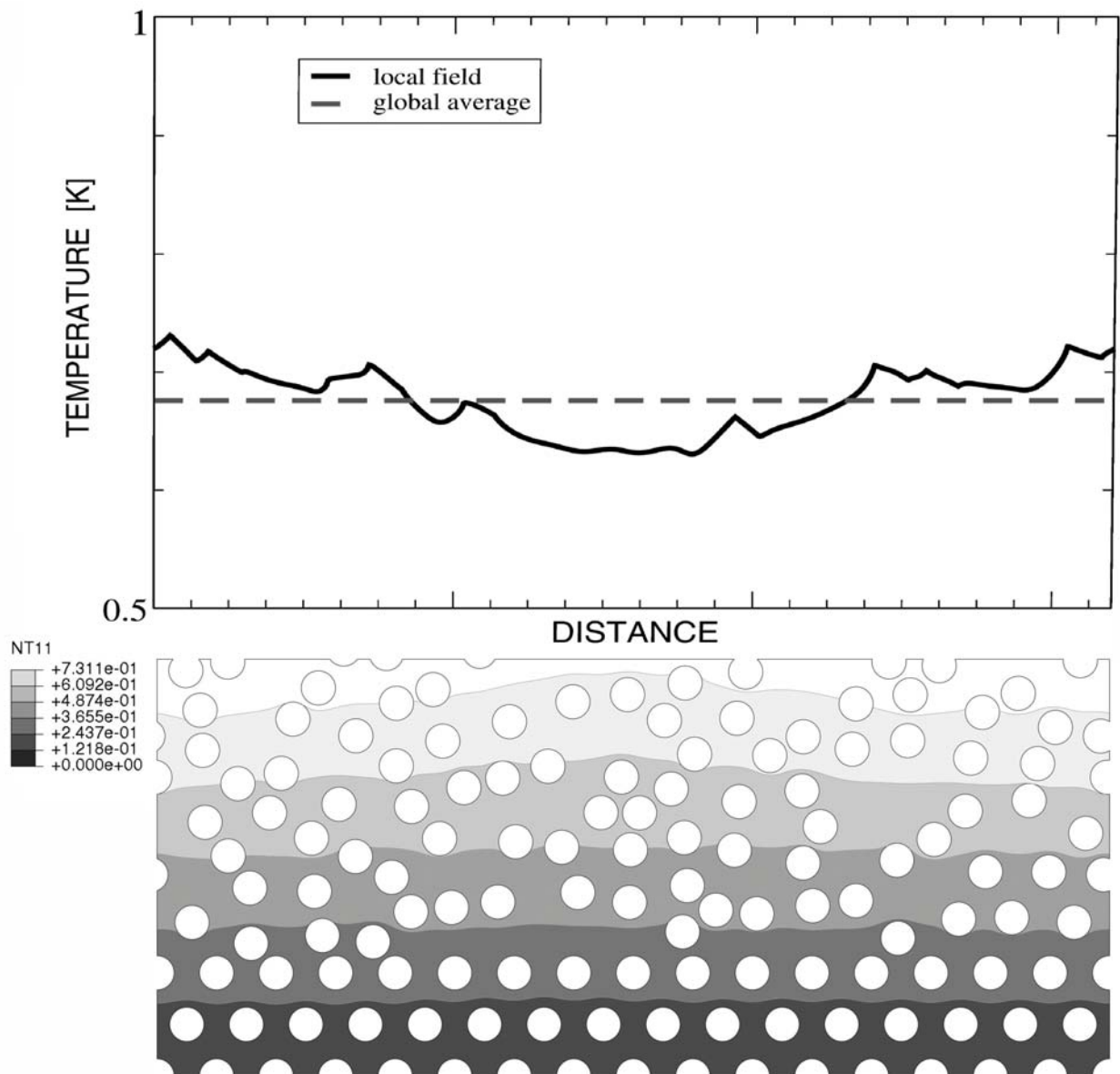


Figure 2.15: Temperature distribution on the free surface (top), in the matrix (bottom) for the 30%vol homogeneous distribution.

Table 2.2: Predicted mesoscopic values for the COF, $\bar{\mu}$, contact pressure, \bar{p} , heat flux, \bar{q} , temperature rise, \bar{T} , and thermal conductivity, \bar{k} , for the different models and regions with volume fraction $\bar{\xi}$, as predicted by the unit cell simulations. For \bar{k} , unit cell (UC) predictions as well as Mori-Tanaka (MT) estimations are performed. The asterisk (*) indicates input values.

	$\bar{\xi}$	$\bar{\mu}$	\bar{p}	\bar{q}	\bar{T}	\bar{k}	
	[%]	[-]	[MPa]	[Wm ⁻²]	[K]	[Wm ⁻¹ K ⁻¹]	
						UC	MT
homogeneous	30	0.420	1.0	0.837	0.676	8.7	8.94
homogeneous	10	0.373	1.0	0.745	0.729	7.16	7.25
clust'd overall	10	0.366	1.0	0.733	0.708	7.16	7.25
plain region	0	0.33*	0.909	0.602	0.691	matrix*	matrix*
clust. region	30	0.42*	1.16	0.964	0.739	8.7*	8.94*

with A being the surface area, $dA = 1 \cdot dx$ for a given planar unit cell.

When comparing the global thermal conductivity as predicted above with Mori-Tanaka estimates, e.g. [Rammerstorfer and Böhm], a very good agreement is found, compare Table 2.2, even considering the fact that planar cells are confronted with three-dimensional Mori-Tanaka estimates. The region containing the cluster of the 10%vol configuration, of course, has the same average thermal conductivity as the 30% configuration.

Frictional dissipation, heat conduction, and surface temperature distribution.

The local contact pressure and the local coefficient of friction determine the frictional heat dissipation, which acts as thermal loading within a heat transfer analysis solving for the local temperature fields. At the contact surface of the clustered region considerably more heat is dissipated due to the combination of a higher contact pressure and higher COF, especially at the cluster subregion with particles relatively close to each other. This gives rise to elevated temperatures on the micro as well as the meso-scale despite the higher thermal conductivity of the particles, and, thus, the higher average (mesoscopic) conductivity in

the cluster region. The particles attract heat and consequently redirect the vertical heat flux from an even distribution (homogeneous random distribution) over the unit cell area to the clustered region on the meso-level, compare Fig. 2.16. On the global scale, as the total heat flux only varies with the global COF, it scales linearly in the homogeneous and clustered configurations with the same volume fraction. Figure 2.17(bottom) shows the distribution of the temperature rise from the ambient temperature at the contact surface for the clustered cell. The periodic boundary conditions ensure temperature continuity over the lateral unit cell boundaries. Consequently, also the global heat flux in the horizontal direction vanishes. For the sake of completeness, the temperature as well as the contact pressure distributions along the contact surface for all particle distributions are compared in Figs. 2.17 and 2.18.

Note that the temperature fields, together with the phase contrast in thermal expansion, cause thermally induced stresses. Computation of these stresses lies fully within the capabilities of the models but is not performed for the present material because this effect is of minor significance.

Due to the limited amount of particles at the surface, several generic unit cells sharing the same topological descriptors should be investigated and averaged appropriately in order to obtain quantitatively reliable results [Segurado et al., 2001].

As a consequence of the relatively quick decay of perturbations from the surface, improved unit cells in terms of computing time should have a larger length-to-height ratio with as many particles at the surface as possible without a significant loss of quality regarding the described tasks. This also means that the importance of the periodic boundary conditions is decreasing.

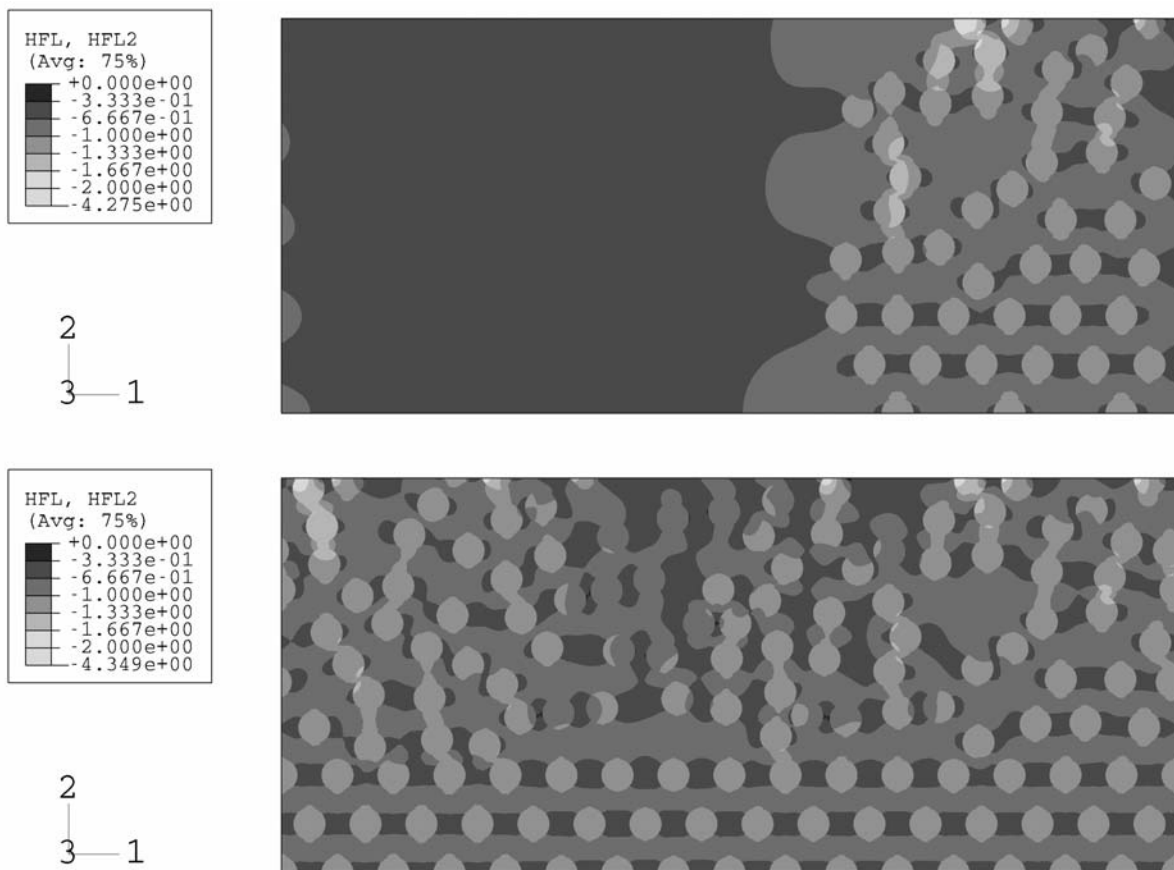


Figure 2.16: Predicted heat flux in the vertical direction for the 30%vol homogeneously distributed (bottom) and 10%vol clustered (top) configurations.

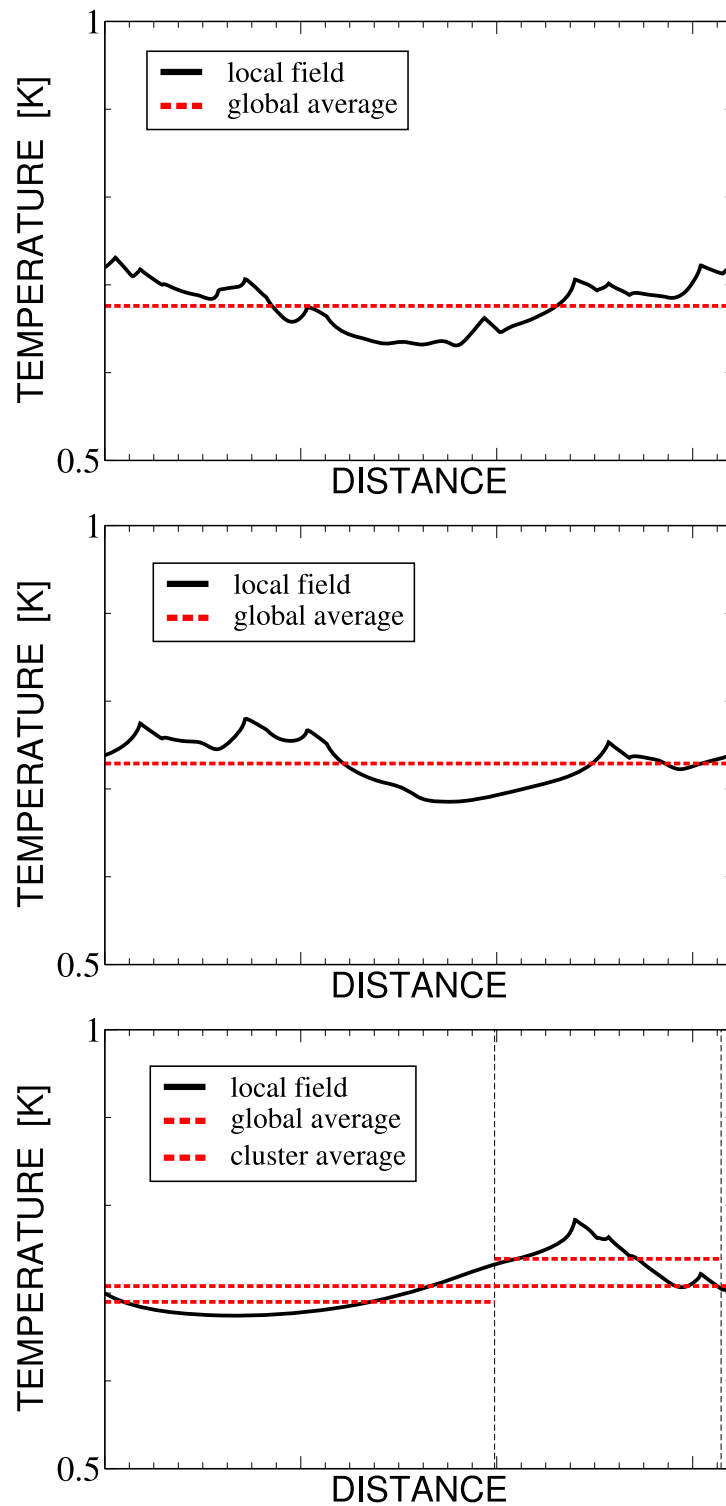


Figure 2.17: Predicted distribution of the surface temperature rise at at 1MPa load and 2mm/s sliding speed. From top to bottom: 30%vol and 10%vol homogeneous distribution, 10%vol clustered configuration.

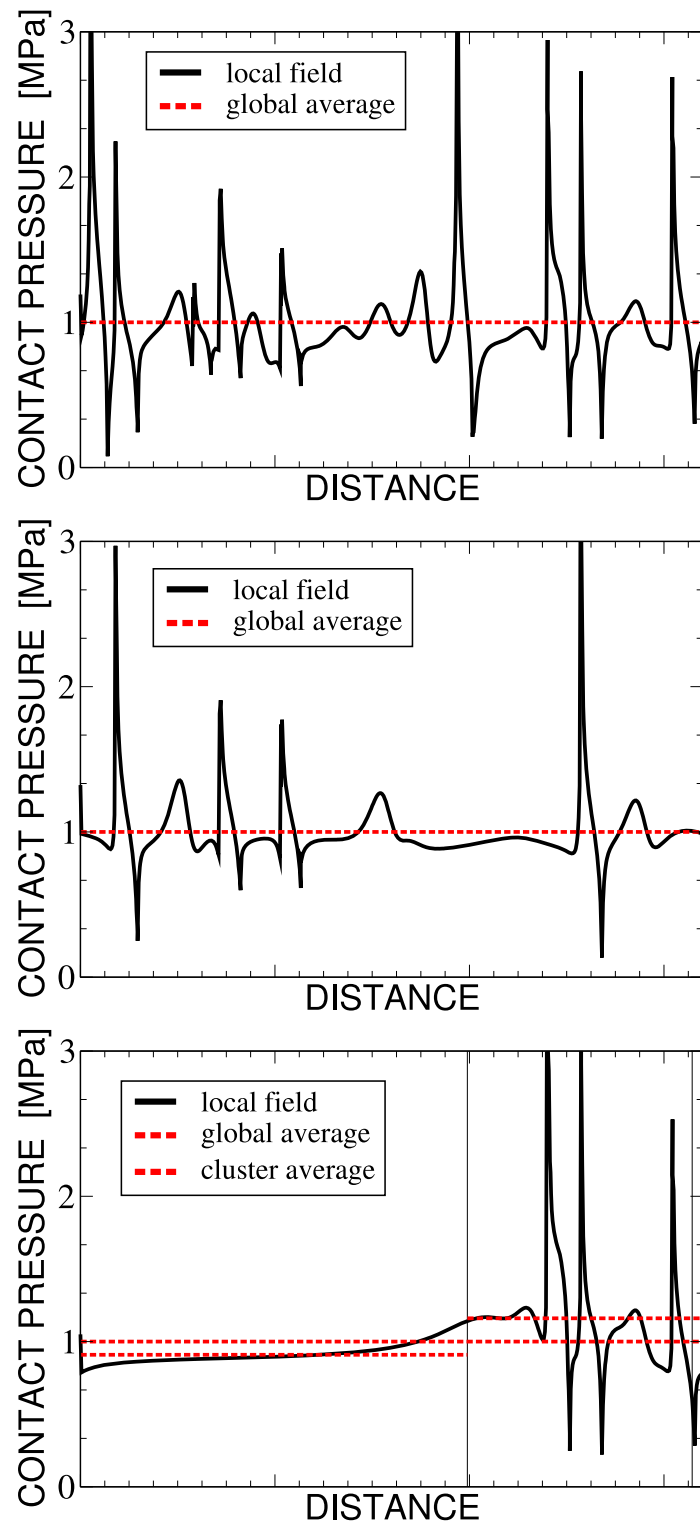


Figure 2.18: Predicted contact pressure for the different configurations at 1MPa load and 2mm/s sliding speed. From top to bottom: 30%vol and 10%vol homogeneous distribution, 10%vol clustered configuration.

2.4 Analyses of the tribological behavior of MMCs under consideration of frictionally excited thermoelastic instability

The thermoelastic behavior of MMCs in typical frictional contacts is treated by various approaches. Analytical calculations of a simplified homogenized model accompanying experimental results serve as an input to Finite Element simulations of the inhomogeneous MMC. Experimental results from [Poletti et al., 2004] show increased COFs and wear with higher sliding velocity, which raises the question about the origin of these phenomena. The effects of frictionally excited thermoelastic instability, associated with thermomechanical coupling at the contact interface, are investigated and a connection or contribution of TEI to the aforementioned experimental findings is assessed.

2.4.1 Simplified analytical model

With the simplified analytical model, in combination with the experimental results, certain unknown process parameters are determined to serve as inputs to the FEM simulations. In this case, the MMC is treated analytically as a homogenized material. Steady state is assumed.

Frictional contact

The frictional contact problem involves two bodies in sliding contact. Frictional heat is dissipated on the contact surface and partitioned between the bodies, subject to material properties and boundary conditions in temperature or heat flux. The standard experimental arrangements for measuring friction and wear, pin-on-ring and pin-on-disk, respectively, comply with this model. For illustration, Fig. 2.19 shows the heat flux distribution from

the perspective of the pin of a pin-on-ring experiment. A part of the total frictionally generated heat, \dot{q}_{diss} , Eq. (2.4), denoted $\dot{q}_{pin,out}$, enters the pin while a contact heat flux, \dot{q}_{cont} , is transmitted over the interface. Since no convection or radiation is considered, the entire heat flux $\dot{q}_{pin,out}$ leaves the pin into the pin's mounting. The nature of the heat fluxes is explained hereafter. Analogous considerations can be made for the ring.

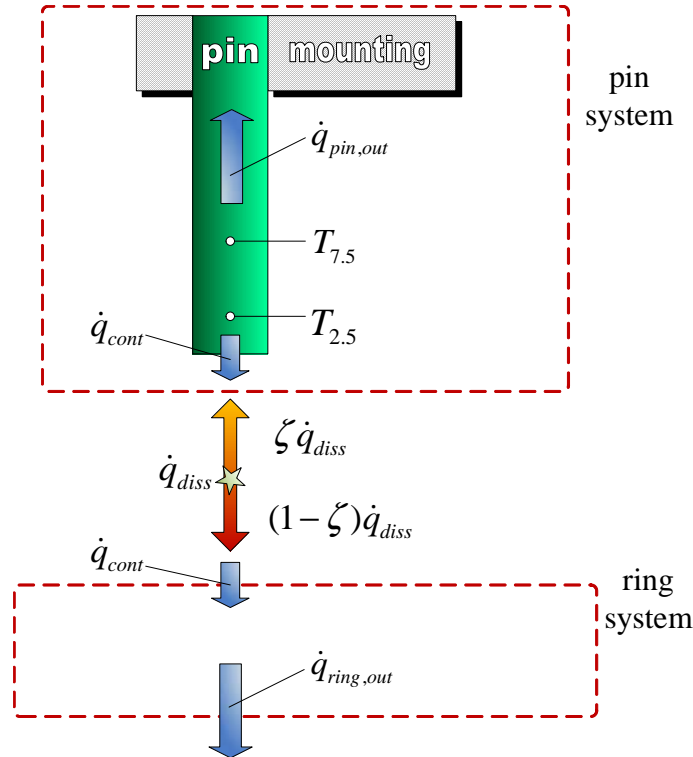


Figure 2.19: Heat balance for the pin in the steady state.

2.4.2 Heat fluxes, heat partitioning factor, thermal contact resistance

Assuming all energy is dissipated as heat on the sliding surface, the rate of heat generated per unit area, \dot{q}_{diss} , is given by Eq. (2.4). It has to be partitioned between the contacting bodies, resulting in the heat fluxes \dot{q}_i for body $i = 1, 2$. In case of two contacting bodies, using the definition of the heat partition factor, ζ , from Eq. (2.8), these heat fluxes

are determined with Eq. (2.9). In non-perfect contact, there exists a thermal contact resistance, which is generally pressure dependent¹³⁾ (among other possible dependencies). Consequently, the temperature in opposing points on the contacting surfaces will not match and a heat flux across the interface orientated towards the lower temperature surface will develop. If these temperatures are denoted T_i and T_j , respectively, the thermal contact resistance shall be defined as

$$R = \frac{(T_i - T_j)}{\dot{q}_{cont}} , \quad (2.12)$$

with \dot{q}_{cont} being the contact heat flux. Considering a pin-on-ring experiment, the pin is always the body of higher temperature, regarding its size compared to the ring, the latter constantly providing fresh, 'cool' material to the contact zone. In the experiments, the global temperature of the ring hardly rises above ambient temperature. As a consequence, the contact heat flux is always directed towards the ring.

If the temperature gradient within a body is known, the heat flux due to conduction is determined by Eq. (2.5) and reads

$$\vec{q}_{conduction} = -k\nabla T , \quad (2.13)$$

with k being the thermal conductivity. The temperature field within the pin is taken to be homogeneous in the radial direction – hence, one-dimensional, linear temperature distribution over the length is assumed. In case of the pin-on-ring test setup, the relation between the temperature distribution and the thermal conductivity of the pin material is given by Eq. (2.13) and yields

$$\dot{q}_{pin,out} = k_{pin} \frac{(T_{2.5} - T_{7.5})}{l} , \quad (2.14)$$

¹³⁾A descriptive model for pressure dependency is the 'smoothing out' of surface asperities with increasing pressure, thus, increasing the real area of contact.

where $T_{2.5}$ and $T_{7.5}$ are the measured pin temperatures, ideally along the axis, with the distance l in between. Since no radiation or convective effects are considered, all the heat passing an arbitrary section of the pin is transferred into the mounting.

The heat flux leaving the pin/ring system through the ring, $\dot{q}_{ring,out}$, is then determined by

$$\dot{q}_{ring,out} = \dot{q}_{diss} - \dot{q}_{pin,out} . \quad (2.15)$$

With these equations, the outgoing heat fluxes of pin and ring, $\dot{q}_{pin,out}$ and $\dot{q}_{ring,out}$, respectively, can be determined by knowing at least two temperatures along both bodies and their thermal conductivities.

2.4.3 Heat balance

With the heat fluxes described above, the heat balance can be established. The heat balance for pin and ring in sliding contact in the steady state, from the perspective of pin and ring, respectively, and neglecting convection and radiation, reads

$$\zeta \dot{q}_{diss} = \dot{q}_{cont} + \dot{q}_{pin,out} \quad (\text{pin system}) \quad (2.16)$$

$$(1 - \zeta) \dot{q}_{diss} = -\dot{q}_{cont} + \dot{q}_{ring,out} \quad (\text{ring system}) , \quad (2.17)$$

with $\dot{q}_{pin,out}$ and $\dot{q}_{ring,out}$ being the heat fluxes leaving the bodies through heat sinks, mounting, etc. Summation of these two equations of course yields the heat balance for the entire system; in this case the contact heat flux cancels out. The thermal contact resistance and the heat partitioning factor remain unknown so far.

2.4.4 Derivation of thermal contact resistance and heat partitioning factor

With the above equations, the thermal contact resistance and the heat partitioning factor are evaluated from pin-on-ring experiments using two methods with differing assumptions. The first approach involves evaluation of Eq. (2.16) at two different points of time of the experimental test, assuming that the thermal contact resistance, R , and conductivity, k , respectively, have not changed significantly, compare Fig. 2.20. The heat balance for the pin using Eqs. (2.16) and (2.12) reads

$$\zeta \dot{q}_{diss} = \frac{T_{pin} - T_{ring}}{R} + \frac{k_{pin}}{l} (T_{2.5} - T_{7.5}) , \quad (2.18)$$

with T_{pin} being the contact surface temperature average of the pin, computed from the measured temperatures and the heat conduction equation Eq. (2.13). The temperature of the ring, T_{ring} , hardly rising above ambient temperature, is known from measurements with the thermographic camera. Evaluation at two different points in time¹⁴⁾, t_1 and t_2 , yields the following system of two equations with the two unknowns R and ζ .

$$\begin{aligned} \zeta \dot{q}_{diss} &= \left. \frac{T_{pin} - T_{ring}}{R} \right|_{t_1} + \frac{k_{pin}}{l} (T_{2.5} - T_{7.5}) \Big|_{t_1} \\ \zeta \dot{q}_{diss} &= \left. \frac{T_{pin} - T_{ring}}{R} \right|_{t_2} + \frac{k_{pin}}{l} (T_{2.5} - T_{7.5}) \Big|_{t_2} , \end{aligned} \quad (2.19)$$

Solving for the thermal contact resistance yields

$$R = -\frac{l}{k} \frac{(T_{pin} - T_{ring}) \Big|_{t_1} - (T_{pin} - T_{ring}) \Big|_{t_2}}{(T_1 - T_2) \Big|_{t_1} - (T_1 - T_2) \Big|_{t_2}} . \quad (2.20)$$

¹⁴⁾In this case, no steady state is assumed.

The heat partitioning factor is then derived from Eq. (2.18).

The second method involves data from two different experiments, preferably tests incorporating the same global pressure but different sliding speeds, as the thermal contact resistance is assumed to be dependent on pressure p , but not on velocity v , compare Fig. 2.21. An additional assumption in this case is that the partitioning factor ζ is the same for both tests. Evaluating left hand side of Eq. (2.16) for steady states of the two tests reads

$$\begin{aligned}\zeta^1 \dot{q}_{diss} &= \frac{{}^1T_{pin} - {}^1T_{ring}}{R} + {}^1\dot{q}_{pin,out} \\ \zeta^2 \dot{q}_{diss} &= \frac{{}^2T_{pin} - {}^2T_{ring}}{R} + {}^2\dot{q}_{pin,out} .\end{aligned}\quad (2.21)$$

Solving the system of equations for the thermal contact resistance yields

$$R = \frac{{}^2q_{diss}(-{}^1T_{pin} + {}^1T_{ring}) + {}^1q_{diss}({}^2T_{pin} - {}^2T_{ring})}{{}^2q_{diss}{}^1q_{pin,out} - {}^1q_{diss}{}^2q_{pin,out}} ,\quad (2.22)$$

and for the heat partitioning factor,

$$\zeta = \frac{{}^2q_{pin,out}(-{}^1T_{ring} + {}^1T_{pin}) + {}^1q_{pin,out}({}^2T_{pin} - {}^2T_{ring})}{{}^2q_{diss}(-{}^1T_{pin} + {}^1T_{ring}) + {}^1q_{diss}(-{}^2T_{pin} + {}^2T_{ring})} .\quad (2.23)$$

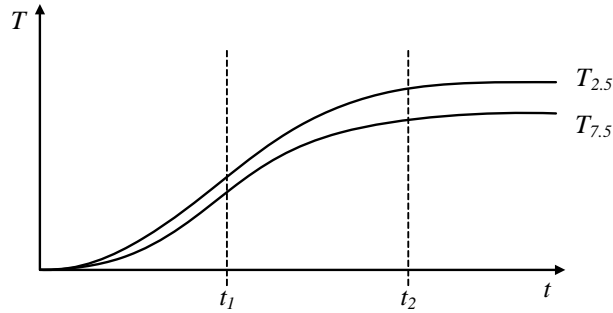


Figure 2.20: Determination of the thermal contact resistance and the heat partitioning factor (method 1); measured pin temperatures vs. time of a single experiment, evaluated at different points of time.

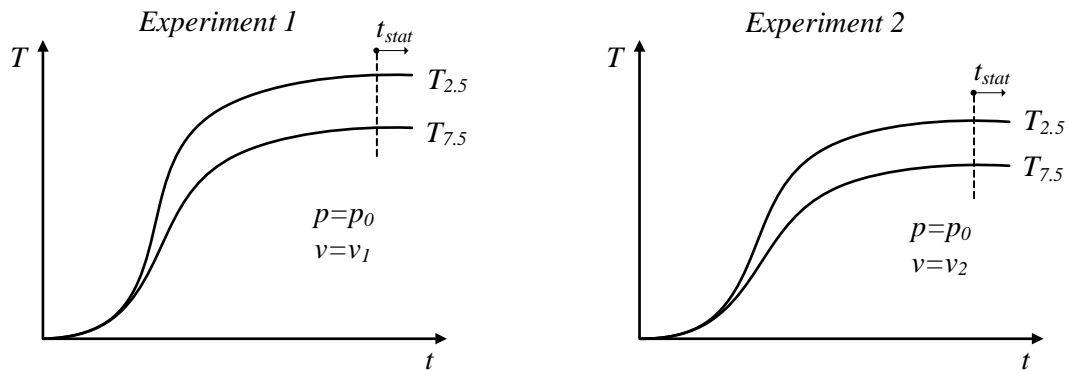


Figure 2.21: Determination of the thermal contact resistance and the heat partitioning factor (method 2); measured pin temperatures vs. time of two different experiments with the same pressure but different sliding velocities, evaluated in the steady state.

2.4.5 Thermoelastic instability

Criteria and derivation of the critical sliding speed.

If the frictional heat generated during sliding drives a thermoelastic problem, the resulting temperature field at the contacting surface can lead to thermoelastic instability. On a local level, the thermal distortion affects the contact pressure, which in turn influences the distribution of frictional heating, which closes the loop again by affecting the temperature field, thus becoming a feedback process. The result is a coupled thermomechanical problem, as the stress distribution is dependent on the thermoelastic deformations and the thermal problem becomes dependent on the stress state. Above a certain critical sliding speed, even uniform pressure distributions are unstable, leading to localisation of temperature and/or pressure, giving rise to damage, wear and other possibly undesirable effects.

[Dow and Burton, 1972] showed that, for a body sliding against a semi-infinite rigid counterbody, an initial perturbation of the temperature field will be amplified for values of the sliding speed greater than a certain limit, v_{crit} . In their work, perfect thermal contact is assumed, permitting the simple condition of temperature continuity over the contact surface. The boundary between stable and unstable (diminishing and growing) response

to an initial perturbation reads [Dow and Burton, 1972]

$$\frac{2n\pi}{l_{tribo}} = \frac{\mu v_{crit} \alpha E}{2k_{pin} J} - 2 \frac{k_{ring}}{k_{pin}} \sqrt{\frac{v_{crit}}{\pi \frac{k_{ring}}{\rho c} z}}, \quad (2.24)$$

where μ is the COF of the material pair, l_{tribo} and z , respectively, are the length and width of the contact patch, α is the coefficient of thermal expansion, k_{ring} and k_{pin} are the thermal conductivities of ring and pin, E is the Young's Modulus of the pin, ρ and c are mass density and specific heat capacity of the steel ring, J is the percentage of the frictional dissipation transformed into heat, and n is the wave number.

The critical velocity in absence of wear for frictionally excited thermoelastic instability (TEI) can then be derived solving for the case of $n = 1$ (the lowest wave number $2n\pi/l$), and assuming 100% heat dissipation ($J = 1$)

$$v_{crit} = \frac{4(\chi + 2\rho c k_{ring} l_{tribo}^2) - 2\sqrt{\rho c k_{ring} l_{tribo}^2 \chi + \rho^2 c^2 k_{ring}^2 l_{tribo}^4}}{\pi z \alpha^2 \mu^2 E^2 l_{tribo}^2}, \quad (2.25)$$

with $\chi = \pi^2 z \alpha \mu E k_{pin} l_{tribo}$

However, instability can also occur because of a pressure dependent thermal contact resistance, also making the heat flux transmitted across the interface dependent on the pressure. Interaction of these two processes was investigated by [Ciavarella and Barber, 2005], whose criterion can be used in this case. Frictionally excited TEI is expected if the following inequality is fulfilled

$$E\alpha(\beta\mu v + \gamma) > 2(1 - \nu)\left(1 + \frac{3.88k_{pin}R_0}{h}\right), \quad (2.26)$$

with the definitions

$$\beta = R_0 + \frac{LR'p_0}{k_{pin}R_0 + L} \quad \text{and} \quad \gamma = \frac{k_{pin}(T_{end} - T_{pin})R'}{k_{pin}R_0 + L} . \quad (2.27)$$

In the above equations, ν is the Poisson ratio, $h = l_{tribo}/2$ is half the contact length, R_0 is the thermal contact resistance $R(p)$ at the steady state value $p = p_0$, L is the length of the pin, R' is the derivative with respect to p of $R(p)$ at p_0 , and T_{pin} and T_{end} are the contact and the end temperatures of the pin, the latter at the position where the pin enters the mounting.

The critical velocity can then be derived as

$$v_{crit} = \frac{2(1 + \frac{3.88k_{pin}R_0}{h})(1 - \nu) - \alpha\gamma E}{\alpha\beta\mu E} . \quad (2.28)$$

Interestingly, the critical velocity due to Eq. (2.25) is independent of the base pressure, which of course is not the case with Eq. (2.28) which explicitly uses a pressure dependent contact heat flux. It is noted, though, that these criteria were derived considering a homogeneous body in consideration and involve half-spaces for one of the contacting bodies. For an inhomogeneous material, the above criteria will only serve as an estimate for the critical sliding speed. They are applied to fictitious, homogenized materials, whose material properties are determined with Mori-Tanaka-estimates.

It must be noted that Ciavarella & Barber claim that, although in most cases frictional heating tends to destabilize the system, for certain forms of the resistance-pressure law, the system can be stable for all sliding speeds. This form of the law is described by Ciavarella and Barber [2005] as

$$R_0 = \frac{L}{Cp_0 - k_{pin}} . \quad (2.29)$$

where C is an arbitrary constant. For $p_0 \leq k_{pin}/C$ this relation is unrealistic, however, for high pressures, Eq. (2.29) defines a resistance which is indirectly proportional to the

pressure. If the thermal resistance exhibits a sufficiently rapid decrease with increasing contact pressure, a stabilizing effect in sliding is found.

2.4.6 Finite element model

The finite element models employed for the simulations are modifications of the models used in the previous chapter, cf. section 2.3.1, therefore the same general descriptions apply. The counterbody is treated differently – mechanically, it is still assumed to be rigid, but it gains the ability to participate in the heat transfer, using the thermophysical material properties of steel. A constant heat partitioning factor $\zeta = 3\%$ is assumed for all runs, which is an input from the combined analytical calculations and experiments. The analytical approach using a homogenized material determines the various heat fluxes, the thermal contact resistance, the heat partitioning factor, and estimates for the critical velocity. In previous experiments [Poletti et al., 2004], the COF of the matrix/steel combination was investigated at different pressures and sliding velocities. For every simulation, the value of the matrix COF is adapted to these experimental findings. The FE simulations are carried out with a pressure and sliding speed of 1MPa and 2mm/s, respectively, which is in the stable regime (see below), and comparisons with the experiments are done by linear extrapolation of the dissipated heat, the temperatures as well as stresses.

2.4.7 Results

Experimental measurements and derived results

Table 2.3 lists the measured and calculated temperatures in the steady state, dependent on the input parameters global pressure, p_{exp} , and sliding speed, v_{exp} , in the experiments performed by cooperation partner *Austrian Research Centers Seibersdorf*. The measured temperatures are $T_{2.5}$ and $T_{7.5}$, respectively, with the indices indicating the approximate distance in mm from the points of measurement to the contact surface of the pin. Using linear extrapolation, the contact temperature, T_{exp} , is derived, and an average temperature, T_{avg} , between the measured temperatures is defined for comparison purposes only. The global temperature of the ring is 20°C for all tests except Test 6, where it is measured as 25°C. The dissipated heat flux, \dot{q}_{diss} , is calculated from the sliding speed, the global COF, and the applied pressure, compare Eq. (2.4). With Fourier's law, Eq.(2.5), the outgoing heat flux of the pin, $\dot{q}_{pin,out}$ is determined; its fraction of the total dissipated heat flux due to frictional sliding, \dot{q}_{diss} , is listed in the column denoted %*Pin*. A large fluctuation of this ratio can be observed here – although in theory the percentage should be approximately constant, as is assumed in the FE simulations. Fluctuation aside, the comparison yields a percentage in the range of 1-3%. The table also lists the global measured COF which includes, but does not distinguish between all dissipative mechanisms of the tribological system. Tests 3 and 7 show a limited number of results due to technical problems during the tests.

A limited number of experimental tests is run, which is clearly too low for quantitatively reliable results but allows for a first estimation of the thermal steady state and the thermal contact resistance of the material pair by the analytical methods described above.

Table 2.3: Experimental measurements as well as some directly derived results; p_{exp} is the applied pressure in the experiment, v_{exp} ...sliding speed in the experiment, T_{exp} ...temperature of contact area in the experiment (linear extrapolation), $T_{2.5}$... temperature, measurement 2.5mm away from contact area, $T_{7.5}$... temperature, measurement 7.5mm away from contact area, T_{avg} ...average of T2.5 and T7.5, μ_{eff} ...macroscopic COF in the experiment, \dot{q}_{diss} ...total dissipated energy at contact area, $\dot{q}_{pin.out}$... heat flux through pin

	p_{exp}	v_{exp}	T_{exp}	$T_{2.5}$	T_{avg}	$T_{7.5}$	μ_{eff}	\dot{q}_{diss}	$\dot{q}_{Pin.out}$	%Pin
#	[MPa]	[mm/s]	[°C]	[°C]	[°C]	[°C]	[-]	[W/m ²]	[W/m ²]	[%]
1	2.0	200	36.5	32	27.5	23	1.05	4.20E+05	1.33E+04	3.17%
2	2.0	700	81.5	68	54.5	41	1.20	1.68E+06	4.00E+04	2.38%
3	9.3	300	93				0.90			
4	2.0	1200	110	100	90.5	81	1.05	2.52E+06	2.81E+04	1.12%
5	2.0	1200	112	94	76	58	1.00	2.40E+06	5.33E+04	2.22%
6	9.3	1200	493	475	457.5	440	1.67	1.86E+07	5.18E+04	0.28%
7	4.6	1000				100	0.80			

Table 2.4: Homogenized material parameters at 20°C as used for the analytical calculations.

	MMC	Counterbody
Young's Modulus	[GPa] 119	(rigid)
Poisson's Ratio	[-] 0.19	(rigid)
Thermal Conductivity	[W/mK] 7.4	20
Coeff. of Thermal Expansion	[1/K] 9.5E-06	-
Specific Heat	[J/kgK] -	450
Mass Density	[kg/m ³] -	7850

Analytical results

The homogenized MMC uses material parameters (at 20°C) according to Table 2.4.

Apart from the outgoing heat flux and the total frictional dissipation, which are listed with the experimental results in Table 2.3, the analytical results comprise the thermal contact resistance and the estimates for the critical sliding speed where TEI is likely to be introduced.

Table 2.5: Results for the thermal contact resistance and the critical velocity.

Thermal contact resistance		
Method 1, Eq. (2.20)	$5.6 \cdot 10^{-6}$	[m ² K/W]
Method 2, Eq. (2.22)	$3.4 \cdot 10^{-6}$	[m ² K/W]
Critical velocity		
Dow & Burton	16	[mm/s]
Ciavarella & Barber (Method 1)	420	[mm/s]
Ciavarella & Barber (Method 2)	470	[mm/s]

The thermal contact resistance is computed by two different methods described above, Eqs. (2.20) and (2.22), compare Table 2.5. Both values are used for further calculations. With knowledge of the total heat dissipated, the thermal contact resistance, the partitioning factor, the outgoing heat flux of the pin, and the global temperature of the ring, the thermal steady state of the system under the above assumptions can be fully described within the scope of the simplified, homogenized analytical model. For a rigid counterbody sliding against the homogenized MMC, the critical velocity following [Dow and Burton, 1972] assuming a perfect thermal contact interface is found to be 16mm/s. Taking into account both thermal contact resistances as calculated above and assuming that they are constant within a test, i.e. $R'(p) = 0$, the critical velocity rises to 420mm/s and 470mm/s, respectively, compare Table 2.5.

It has to be noted that the analytical derivations of the critical sliding speed are based on a homogeneous, isotropic body and are applied to a model with homogenized material parameters, whereas the FEM simulations employ an inhomogeneous MMC. Consequently, the analytically derived critical speeds serve only as estimates. The use of an inhomogeneous composite model of the multi-inclusion unit cell type adds additional variables to the system which alter the value of the critical velocity and, hence, the stability limit, but do not end its existence.

Table 2.6: Material Parameters used in the Simulations.

		Matrix	Particle	Counterbody
Young's Modulus	[GPa]	108	440	(rigid)
Poisson's Ratio	[-]	0.3	0.19	(rigid)
Thermal Conductivity	[W/mK]	6.5	18	20
Coeff. of Thermal Expansion	[1/K]	9.5E-06	8.0E-06	(rigid)

FE simulation results

The material parameters (at 20°C) used in the FE simulations are listed in Table 2.6.

To determine the critical sliding velocity, using the multi-inclusion type model of the MMC described above, the sliding speed is gradually increased from the 2mm/s base speed until its limit is encountered, above which the simulations are non-convergent. The critical velocity in the simulation is about 150mm/s, which is right between the two analytical estimates.

Results for the temperatures predicted in the simulations are listed in Table 2.7. Since the simulations are performed at 1MPa pressure and a sliding speed of 2mm/s, results in terms of temperatures or stresses are extrapolated for different pressures and velocities. Comparing the FE results for the temperatures to the experiments, a very good agreement is observed for the slightly overcritical case ($v = 200\text{m/s}$) and the differences are higher if the sliding speed considerably exceeds the critical velocity.

There are certain effects which will be measured as an increase of the COF in the experiments, like plastic deformation or wearing of material by, e.g., third body abrasion. These are not individually discerned by the given test setup and are likely to increase with loading and sliding speed. In the light of this, it is consistent that the COFs measured in the experiments are consistently higher than the predictions of the FE simulations, where these effects are not regarded.

Table 2.7: FE simulation results at 1MPa pressure and sliding speed 2mm/s, extrapolated to p and v according to the experiments; T_{FE} is the predicted surface temperature, μ_{eff} is the effective COF in the simulations; the heat partitioning factor ζ is fixed at 3%.

Test#	p	v	T_{FE}	μ_{eff}
	[MPa]	[mm/s]	[C]	[-]
1	2.0	200	35	0.89
2	2.0	700	67	1.20
3	9.3	300	88	0.89
4	2.0	1200	88	1.00
5	2.0	1200	85	1.00
6	9.3	1200	496	1.34

2.4.8 Conclusion

The validity of the FE continuum mechanics of materials approach utilizing unit cells is demonstrated for the case of undercritical conditions. Above the stability limit, the tribological FEM system is non-convergent. Perturbations in temperature or pressure which grow in time are not limited to inhomogeneous materials but are also encountered in contact pairs incorporating homogeneous materials. In FE simulations, these perturbations inherently exist due to numerical reasons with their origin in geometrical imperfections in combination with the contact algorithm(s). In reality, pressures or temperatures of course cannot reach infinite values. Therefore, a 'compensation' reaction of the material which limits these values in the form of damping has to take place. TEI is naturally limited by plastic deformation and wearing off of material, in the form of, e.g., thermocracking in case of ceramics or adhesive or abrasive wear in the case of ductile materials. In the view of these findings, the validity of thermo-elastic predictions above the stable regime has to be seriously questioned. Extrapolating from results of linear elastic simulations to sliding speeds above the stability limit is not advised. In any case, the stability limit needs to be estimated in the first place, e.g. by analytical methods as described before.

In experiments, an increase of wear and COFs are observed. This elevations are ascribed

to the effects of TEI, but also to effects of other contributing mechanisms, e.g. plastic deformation, separation energy, etc. The experimental setup used is not designed to allow for distinguishing between these effects individually.

The practical consequence for affected tribological systems, operating in the unstable regime, is that either wear or increased COFs have to be accepted, or a design change has to be considered. For example, if the thermal contact resistance is either not or weakly dependent on pressure, neither will the stability limit. In this case, a possible design change to allow for lower sliding velocities is recommended to avoid or control excessive wear.

Chapter 3

Forming simulations of MMC components by a micromechanics based hierarchical FEM approach

3.1 Introduction

3.1.1 Motivation and scope

Hot forming is an important metal forming technique for semi-finished products. However, the use of metal matrix composites (MMCs) is constrained by their generally limited formability. In order to better understand the process and the variables involved, predictions of the material response to overall loading are of high interest. Computational tools employed in such predictions are challenged by numerous variables associated with the composition of the material, e.g. type, volume fraction, sizes, shapes, or distributions of reinforcing particles. These affect the thermomechanical and physical properties of MMCs, such as thermo-elastic, elasto-plastic, or conduction properties. On the one hand, modeling tools

have to be capable of reliably predicting the overall response of the composite based on the input of the individual properties of the phases, a process denoted as homogenization in the previous chapters. On the other hand, they have to correctly translate prescribed macroscopic loads into local responses (localization). Two different approaches are utilized for homogenization and localization; the Incremental Mori-Tanaka (IMT) as an analytical constitutive material law based on a mean field approach, and a periodic microfield approach in form of a unit cell method. As in the previous chapter, investigations are performed on different length scales in terms of a hierarchical approach.

The present work deals with computational simulations of an elasto-plastic particulate metal matrix composite undergoing finite strains.

3.1.2 Literature review

There are two widely used approaches in micromechanics of materials. Mean field methods aim to obtain the overall properties of inhomogeneous materials in terms of phase averages of the stress and strain fields. They usually give rise to analytical models, and, as a consequence, pose low computational requirements. They are typically based on Eshelby's solution for single ellipsoidal inclusions in an infinite matrix [Eshelby, 1957]. For non-dilute inclusions, Mori-Tanaka type methods [Mori and Tanaka, 1973; Benveniste, 1987] allow an efficient evaluation of the thermo-elastic properties of MMCs. When investigating inhomogeneous materials containing thermo-elasto-plastic constituents, there have been two main lines of development. On the one hand, the secant plasticity concept has been applied [Tandon and Weng, 1988] which is limited to radial loading paths in stress space. On the other hand, incremental plasticity models, such as the incremental Mori-Tanaka (IMT) method, have been developed [Pettermann et al., 1997] for small strain applications. An essential feature of the IMT is the capability of accounting for non-radial load paths, an important prerequisite for its use as a constitutive law. In the elasto-plastic regime, the IMT typically overestimates overall strain hardening of particulate MMCs, but recent

improvements have been achieved by modifications to the model [Doghri and Ouaar, 2003; Bornert, 2001] .

The second micromechanical approach comprises evaluation of highly resolved local fields of a specific microstructure by employing discrete models of its geometry. Periodic microfield approaches (PMAs) typically employ unit cells to study periodic phase arrangements in order to limit the computational effort [Böhm, 2002; Böhm et al., 2002]. However, high resolution discretizations of unit cells containing a number of randomly positioned particles in a matrix result in large models as well as computation times. Consequently, the PMA using unit cells is not suited for predicting the response of an entire component, but is typically employed for computational material characterization.

In this work, both micromechanical approaches for performing homogenization and localization are combined and employed within the framework of the Finite Element Method (FEM). The IMT method is extended to account for finite strains [Pettermann et al., 2006], and is used to predict the effective MMC response. The PMA is employed to investigate the local fields in the matrix and reinforcements, and, by homogenization, the effective response on the mesoscale. The quality of the results of the analytical IMT approach as well as its limit of applicability are evaluated by comparing results with predictions from periodic unit cell models.

3.2 Modeling approach

A hierarchical concept is used, by which the material as well as the component response is investigated on different length scales. These are defined as

- *Macroscale* ... the length scale of the MMC component
- *Mesoscale* ... an intermediate length scale where the MMC is regarded as homoge-

nized material

- *Microscale* . . . the smallest scale which is set by the inclusions' size

On all scales, constitutive formulations which involve co-rotational Cauchy stresses are utilized. Since metal plasticity is to be investigated, where the Young's modulus is typically several orders of magnitude larger than the yield stress, and, consequently, the elastic contributions to the strain are very small, logarithmic strains with additive decomposition of elastic and plastic contribution are used,

$$\boldsymbol{\epsilon} = \boldsymbol{\epsilon}_{el} + \boldsymbol{\epsilon}_{pl} . \quad (3.1)$$

In terms of the deformation gradient, the total deformation is decomposed as

$$\mathbf{F} = \mathbf{F}_{el}\mathbf{F}_{pl} . \quad (3.2)$$

The IMT is employed as constitutive material law, implemented into the FEM package ABAQUS/Standard [Simulia Inc., 2004], in terms of a user-defined subroutine, which can handle thermo-elastoplasticity as well as temperature dependent material data [Pettermann et al., 1997, 2006]. An introduction to Mori-Tanaka estimates and the IMT has been given in chapter 1. The extension from the small strain formulation to finite strains entails the extension of the matrix constitutive behavior to finite strain J2 metal plasticity and the handling of the rotations of the material systems. Within the chosen framework, finite plastic deformations are associated with rotations of the material reference systems at the micro- as well as the mesoscale. For equi-axed reinforcements these rotations are assumed to be equal (in the meanfield sense). This implies that the rotation of the matrix phase is fully conveyed to the embedded linear elastic particles. Inelasticities are confined to plasticity only and do not account for creep, relaxation or damage.

For the PMA, a multi-particle unit cell is taken from [Böhm et al., 2004]. The cell has twenty spherical inclusions in a periodic arrangement comprising a particle volume fraction of 20%, compare Fig. 3.1. Discretization is chosen with respect to the scale of the particles, resulting in about 50000 elements. Three-dimensional tetrahedral continuum elements with second-order shape functions are employed. These elements have ten nodes and four Gauss points and are used in their "modified" form to prevent volumetric locking. The master node concept is utilized to apply mesoscopic deformations. It is performed in terms of the deformation gradient which is suitable as a measure of deformation in the finite deformation regime. As mesoscopic responses, the master node reactions of the unit cells are evaluated in terms of co-rotational Cauchy and first Piola Kirchhoff stresses. Evaluation of the highly resolved microfields is performed statistically and described in terms of histograms. The latter are probability density distributions that not only reproduce the frequency of the classes but also account for their integration point volume is taken into account, since the latter is not constant for every integration point but, in general, can vary on the order of one or two magnitudes within the model.

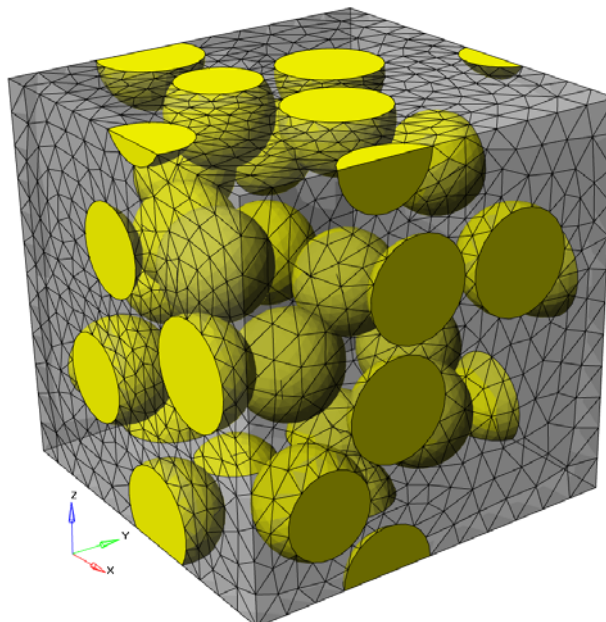


Figure 3.1: The periodic unit cell used in the simulations, with the matrix set semitransparent and masked particle mesh.

Both approaches are combined to make use of their individual capabilities and advantages. The first step in applying the hierarchical concept is the prediction of the components' response to overall loading by the FEM, employing the IMT as mesoscopic constitutive material law. Due to its low computational requirements, the IMT is particularly suited for this task. Further localization is accomplished by this method in terms of phase averages on the microscale. The components of the deformation gradient are also part of the result. The second step is accomplished by selection of appropriate locations in the macroscopic model, extraction of the evolution of the mesoscopic deformation gradients with overall loading, and application of these deformation histories as mesoscopic loads to the computationally expensive PMA. The master node coordinates in the deformed configuration can be directly computed from the definition of the deformation gradient, compare Eq. (1.15), $d\mathbf{x} = \mathbf{F}d\mathbf{X}$, if it is written in the form

$$[d\vec{x}_1, d\vec{x}_2, d\vec{x}_3] = \mathbf{F}[d\vec{X}_1, d\vec{X}_2, d\vec{X}_3] \quad , \quad (3.3)$$

In Eq. (3.3), three line elements make for the column vectors of a matrix in order to define the deformation gradient of a material point. In this context, the three linearly independent line elements are understood as those edges of the unit cell that contain the origin and the master nodes. For the rectangular unit cells used in this work, which are aligned with the global coordinate system (in the undeformed configuration), coincident points of origin, and with edge lengths of 1 unit dimension, the master node coordinates at the actual deformation can directly be seen as the elements of the column vectors of the deformation gradient, since the undeformed configuration equals the identity matrix.

The respective displacement vectors of the master nodes can be determined by, compare Eq. (1.17)

$$[d\vec{u}_1, d\vec{u}_2, d\vec{u}_3] = d\mathbf{x} - d\mathbf{X} = \mathbf{F} - \mathbf{I} \quad . \quad (3.4)$$

This procedure is performed using the program `extract_F` [Luxner, 2007]. The mesoscopic deformation histories are then applied to the periodic unit cells by prescribing the master node displacements deducted from the deformation gradient at the selected region of the model. Since the evolution of the latter is nonlinear with deformation even for simple load cases, the master nodes follow three independent nonlinear prescribed displacements per master node.

For the unit cell response, evaluation of tensors as well as scalar fields is done by volume averaging in the sense of Eq. (1.3), in practice by using approximate numerical quadrature, compare Eq. (1.13). This can be performed for both phases as well as for individual particles. As reference volume, the entire phase, e.g. the matrix, individual particle volume, or the total volume of the unit cell can be chosen. Information on the individual integration point volumes has to be present in the output database. Such volume averaged fields are the averages of the deformation gradient \mathbf{F} and its rotational part \mathbf{R} , the logarithmic strain tensor (the elastic and plastic part), the accumulated equivalent plastic strain and the Cauchy stress tensor. In practice, the described steps are performed by the program `deformationanalyzer` [Luxner, 2007], which also provides histogram data per integration point associated with the respective element sets.

Applying mesoscopic deformation histories extracted from the FEM-IMT predictions to the unit cells gives access to the mesoscopic MMC responses, e.g. the Cauchy stress tensor. These are used to verify the IMT results attained in the previous step. On the other hand, the microfields of the PMA are predicted for detailed insight to the matrix and particle scale. Additionally, they are compared to the IMT's phase averaged results to assess the latter's limits of applicability.

Table 3.1: Elastic material parameters of matrix and particles.

		matrix	particles
Young's Modulus	[GPa]	100	400
Poisson's Ratio	[-]	0.3	0.19

3.3 Example

Simulations are performed on a Gleeble^{®1)}-type experiment, which is a compression test of a cylindrical specimen between two anvils. The length and diameter of the specimen are 15mm and 10mm, respectively. The model material investigated in this work resembles an MMC with 20%vol of ceramic particulate inclusions. The particles are assumed to be of spherical shape and statistically homogeneously distributed. The matrix is taken to behave elasto-plastically and the inclusions are linear elastic; both phases are isotropic.

The elastic material parameters Young's moduli $E^{(m)}$ and $E^{(p)}$ as well as the Poisson's ratios $\nu^{(m)}$ and $\nu^{(p)}$ of matrix and particles are listed in Table 3.1. The flow curve of the matrix material is shown in Fig. 3.2. Associated J2-plasticity and isotropic hardening are adopted. A perfect interface bonds the individual phases and no damage is assumed to occur throughout the loading history.

An axisymmetric FEM model for the upper half of the specimen is employed using continuum elements with biquadratic displacement interpolation and reduced integration. The initial aspect ratio of the elements is set to 2/3 (radial/axial dimension). In Fig. 3.3, the undeformed, homogeneous mesh is visible at the top. The global deformation applied resembles a reduction in length to 2/3, and is prescribed in the axial direction at the top edge. To model stiction between specimen and anvil, radial displacements at this edge are locked.

The FEM simulation of the above sample is carried out with the constitutive behavior

¹⁾Dynamic Systems Inc., Poestenkill, NY

of the MMC described by the IMT. Three locations in the macroscopic model are chosen (Fig. 3.3) such that a broad spectrum of mesoscopic stress and strain histories is provided for detailed analysis by the PMA. Location A is the Gauss point closest to the center of the specimen. Location B is close to the outer surface, and location C represents a region where shear deformation is expected. The simulations are based on a stress-free initial state and temperature effects are not regarded.

3.4 Results

3.4.1 Macro response: deformation

The final state of deformation is described by the macroscopic deformation gradient component in axial direction, $F_{22} = 2/3$. The predicted global deformation of the specimen in this state is shown in Fig. 3.3; no deformation scaling is used. The stiction condition between the anvils and the specimen causes barreling. Note that elements at the top right corner are severely distorted because of the chosen load introduction. However, this region

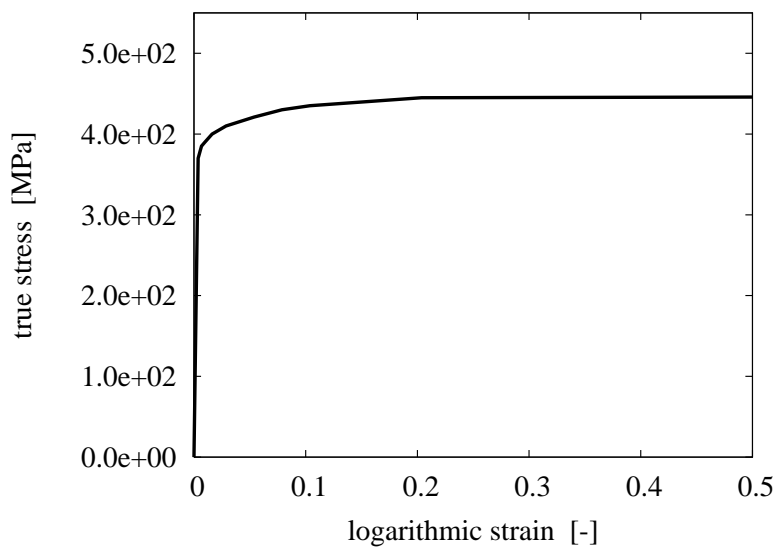


Figure 3.2: Uniaxial stress-strain curve for the matrix material

is not evaluated and does not influence the response of the investigated regions. The center region of the specimen undergoes the highest deformation. Deformation is constrained at the top, where a cone-shaped region of mildly deformed material is driven through the sample.

3.4.2 Meso response: Cauchy stresses

The evolution of the mesoscopic Cauchy stresses at the selected locations versus the global measure of deformation, F_{22} , is shown in Figs. 3.4-3.6. The figures include the IMT predictions as well as the unit cell results, which agree excellently for all cases. For location

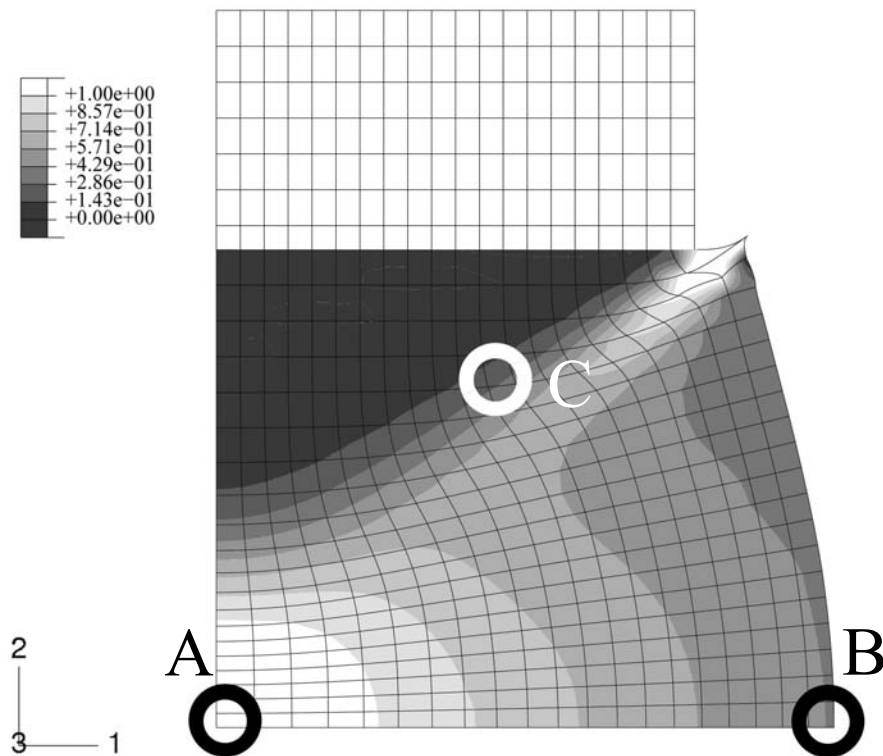


Figure 3.3: FEM simulation of the macroscopic uniaxial compression of a cylindrical MMC component; undeformed regular axisymmetric mesh and true scale deformation; contours show the accumulated equivalent plastic strain in the matrix phase; selected locations A,B,C for subsequent detailed analyses.

A, the mesoscopic stress histories are close to a uniaxial compressive stress state, showing some 'hardening' despite a nearly ideal plastic flow behavior of the MMC material on the mesoscale. Note that for the PMA prediction, no convergence could be achieved beyond a macroscopic deformation gradient of $F_{22} = 0.72$.

For location B, a biaxial stress state with compression in the axial and tension in the hoop directions is predicted. Although axial compression is dominant at the macro level, the meso-stress magnitude in this direction reaches a maximum and then decreases in the course of deformation, whereas the tensile hoop stress increases steadily. This markedly non-radial loading history is consistently predicted by the IMT, owing to its incremental formulation. Region C shows a more general stress state including mesoscopic shear. For the present stress-strain formulation, this causes rotation of the material reference system. The resulting deformation of unit cells pertaining to the three locations and the final states of deformation are displayed in Fig. 3.7, no displacement scaling being used. Note that in the case of location C the employed unit cell exhibits some mesoscopic strain concentration. However, this has no influence on the results, which will be explained in the next chapter.

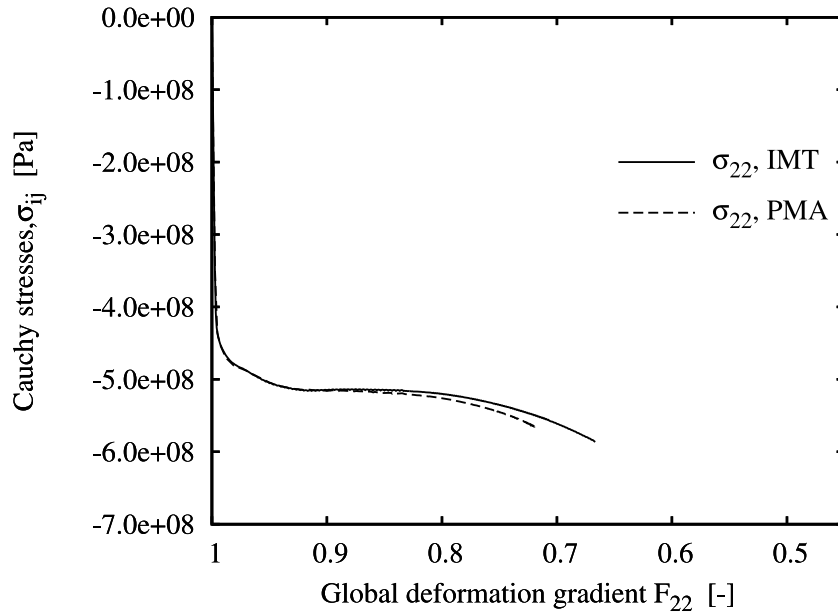


Figure 3.4: Evolution of the mesoscopic Cauchy stress tensor component σ_{22} over the global deformation gradient component for location A, predicted by the IMT and the PMA.

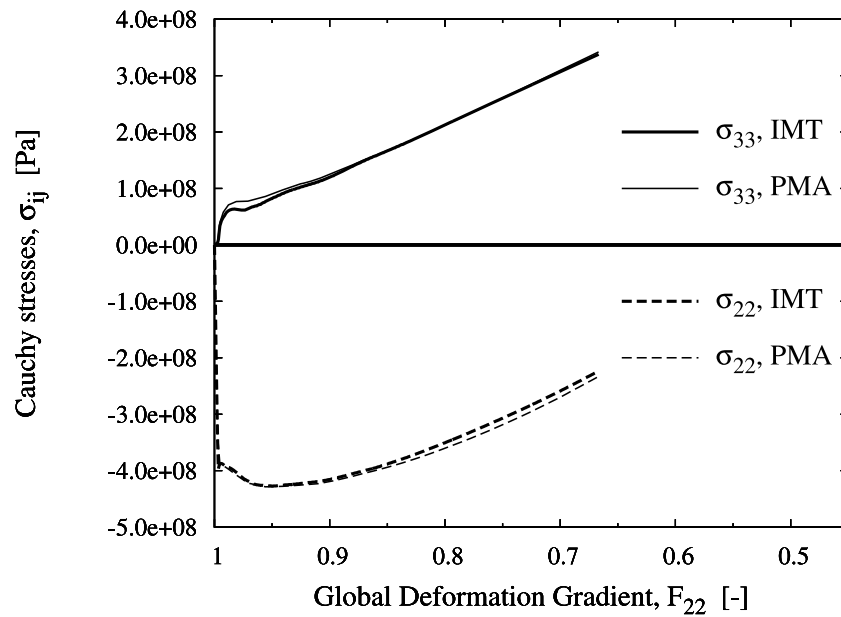


Figure 3.5: Evolution of the mesoscopic Cauchy stress tensor components over the global deformation gradient component for location B, predicted by the IMT and the PMA.

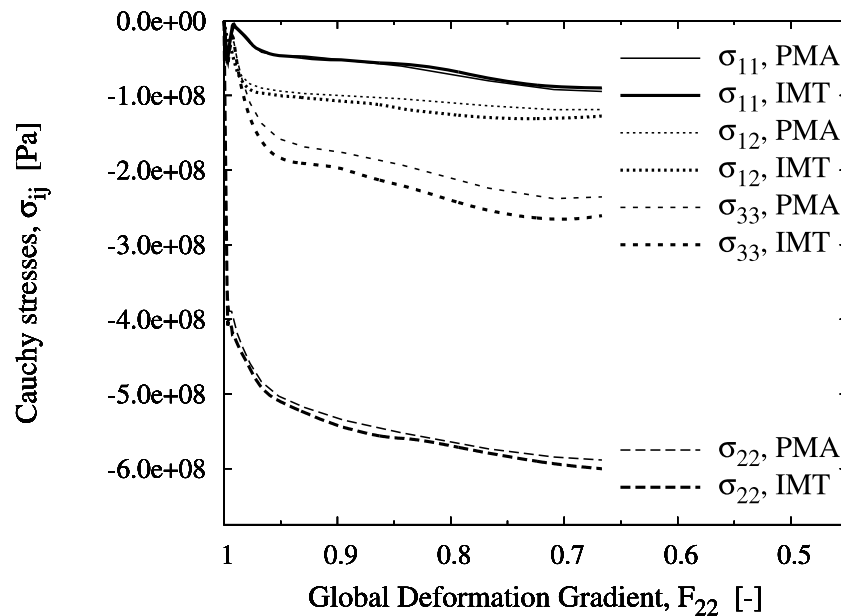


Figure 3.6: Evolution of the mesoscopic Cauchy stress tensor components over the global deformation gradient component for location C, predicted by the IMT and the PMA.

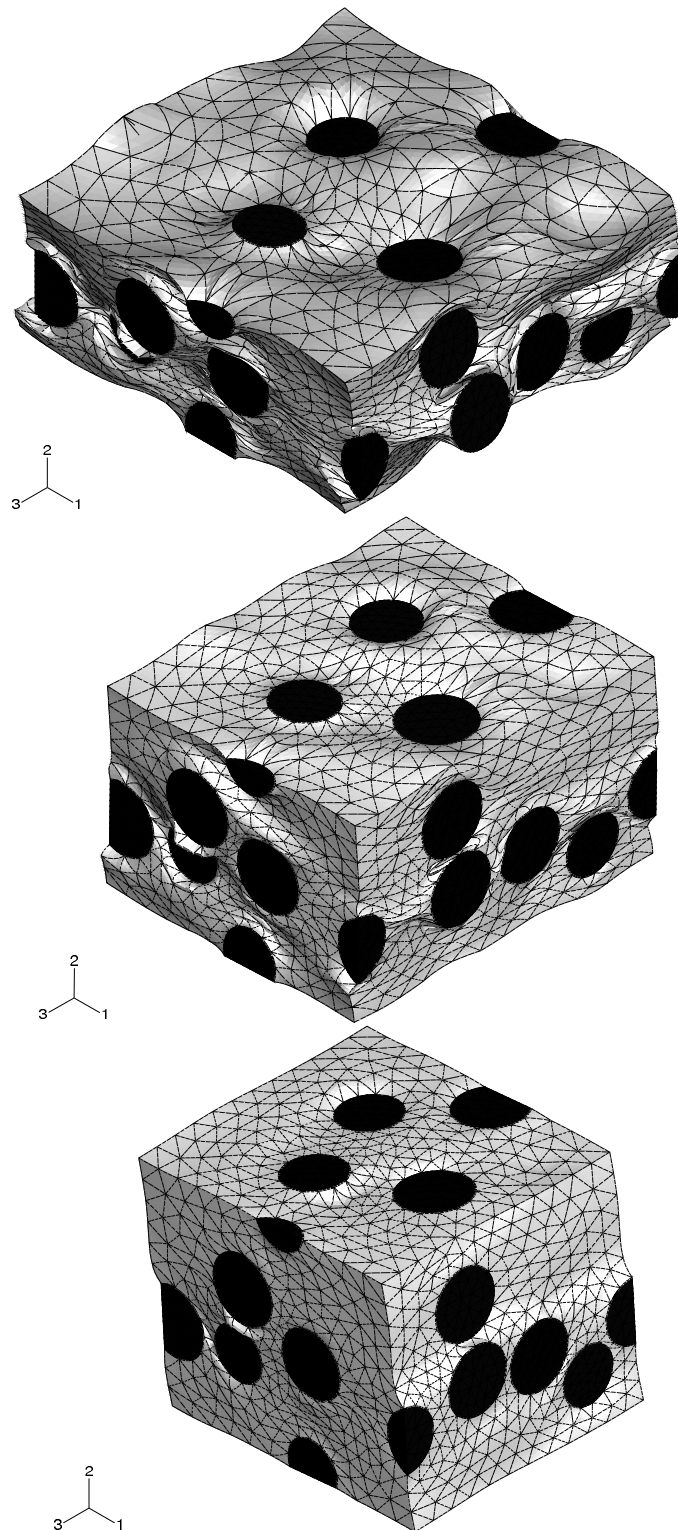


Figure 3.7: Unit cell deformations for the three selected locations A (top), B (middle), and C (bottom), at their final state of deformation F_{22} , at true scale; undeformed unit cells are cubic.

3.4.3 Micro response

Accumulated equivalent plastic strain in the matrix

The probability density distribution of the accumulated equivalent plastic strain in the matrix, as predicted by the unit cell simulations at location A, is shown in Fig. 3.8 for the global deformation gradient $F_{22} = 0.88$. Also indicated are its phase average value from the unit cell, and the prediction by the IMT. The latter is very close to the phase average obtained from the unit cell. On the microscale, however, the scatter of the accumulated equivalent plastic strain in the matrix phase is considerable.

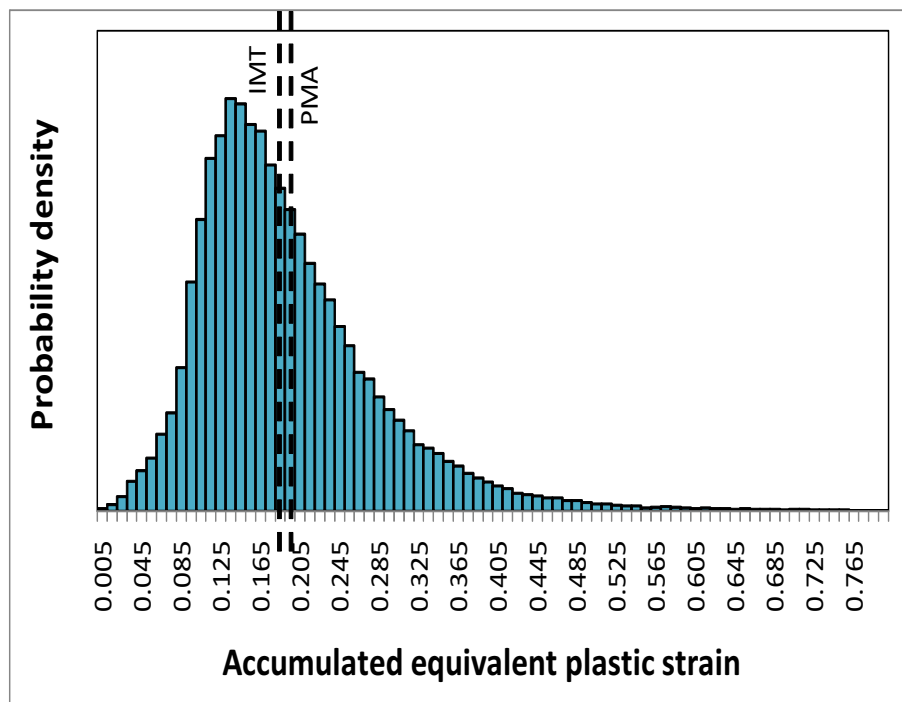


Figure 3.8: Probability density distribution of the accumulated equivalent plastic strain in the matrix phase as predicted by the unit cell simulations at $F_{22} = 0.88$ for location A, its mean value (PMA), and the IMT prediction.

Maximum principal stresses in the particles

The maximum principal stresses can serve as an indicator for particle fracture. Figures 3.9 and 3.10 show the probability density distribution of the maximum principal stresses in the particle phase, as predicted by the unit cells, for locations A and B, respectively. In the figure, only the envelope curves are presented for easier viewing; bin spacing is $5 \cdot 10^7$ MPa. Two states in the deformation history are illustrated, described by macroscopic deformation gradients $F_{22} = 0.988$ and $F_{22} = 0.88$, respectively. The figures also show the phase averages from the unit cell and the mesoscopic IMT predictions. It should be noted that the maximum principal stresses at some Gauss points are outside the displayed interval. However, the associated volumes are two orders of magnitudes smaller than that of a particle.

Generally, for both selected regions, the distribution of the maximum principal stresses shifts towards higher values in course of the deformation. At the same time, its scatter increases. Although location A is associated with a uniaxial compressive stress state mesoscopically, the unit cell simulation predicts a considerable level of positive maximum principal stresses in the particles, even at moderate deformation, cf. Fig. 3.9. In fact, particle fracture in the center of Gleeble tests has been found experimentally [Poletti et al., 2003]. The IMT severely underestimates the maximum principal stresses; its predictions are compressive with a value of $\sigma_I^{(p)} = -20$ MPa at $F_{22} = 0.988$ and close to zero at $F_{22} = 0.88$, respectively.

Rigid body rotations

Figure 3.11 shows the distribution of the rigid body rotations of individual particles within the unit cell in the 12-plane for location C. The average rotation of all particles as well as the mesoscopic rotation of the material system are also indicated in the figure. In this case, the end-state of the simulation is regarded, $F_{22} = 2/3$. The rotations of components in

other planes than the 12-plane are at least one order of magnitude smaller. Because of the much higher Young's modulus of the particle phase compared to the matrix, deformations of the particles are small. Therefore, the scatter within individual particles disappears and the distribution of rotations is represented well by the average rotations of individual particles.

The good agreement in the averages of the PMA and the IMT as well as the relatively small scatter in rotation of the individual particles justify the assumption made in the finite strain formulation of the IMT, compare Section 1.3.3, 12.

Other load cases

Two essential load cases associated with forming are hydrostatic pressure and spatially homogeneous temperature changes. Due to its formulation, the IMT is not capable of predicting plastic yielding in these cases. However, unit cell simulations of these load cases do not show mesoscopic residual strains either, at least not at reasonable loads, compare Fig. 3.12, which pertains to the triaxial compression (hydrostatic) load case. Consequently, the IMT maintains its good predictive capabilities on the mesoscale.

All tools are fully prepared to include the thermal expansion, temperature history as well as the temperature dependence of the material properties in the simulations.

Note that although the adopted flow curve of the matrix almost approaches that of an ideally plastic material, the IMT is capable of utilizing all kinds of hardening curves, including softening (where, however, mesh dependencies may occur). Several loading scenarios are performed successfully using strain hardening as well as strain softening, compare also Section 3.6.

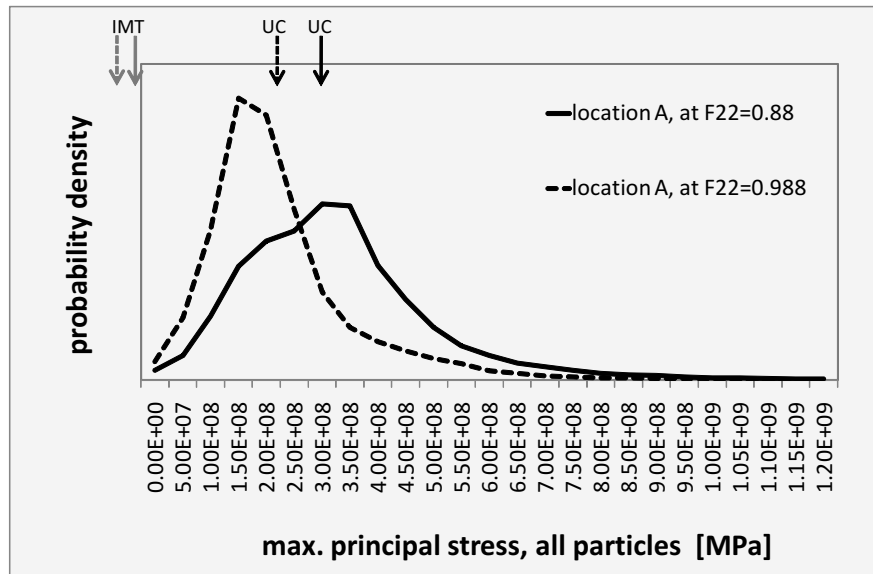


Figure 3.9: Probability density of the maximum principal stress in all particles as predicted by the unit cell simulations for location A, evaluated at $F_{22} = 0.988$ and $F_{22} = 0.88$; arrows indicate its mean value (PMA) and the IMT prediction.

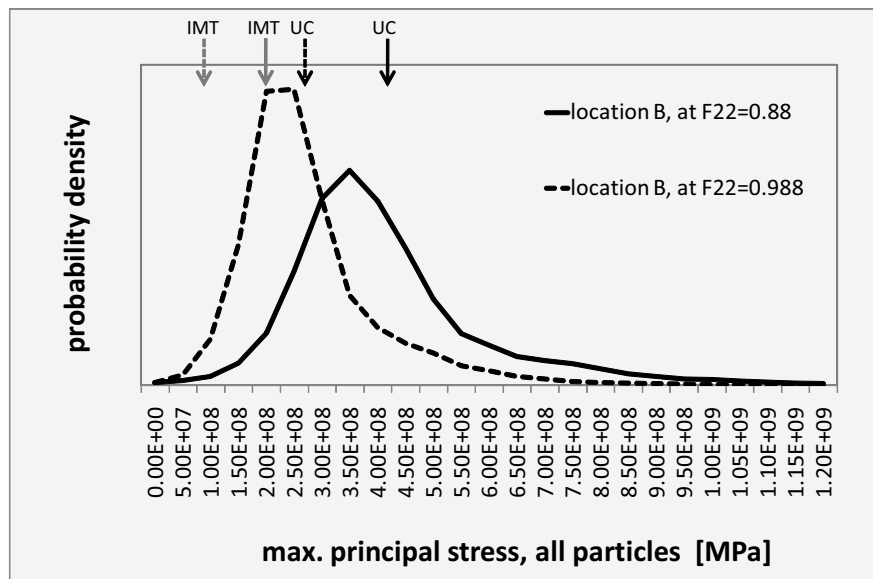


Figure 3.10: Probability density of the maximum principal stress in all particles as predicted by the unit cell simulations for location B, evaluated at $F_{22} = 0.988$ and $F_{22} = 0.88$; arrows indicate its mean value (PMA) and the IMT prediction.

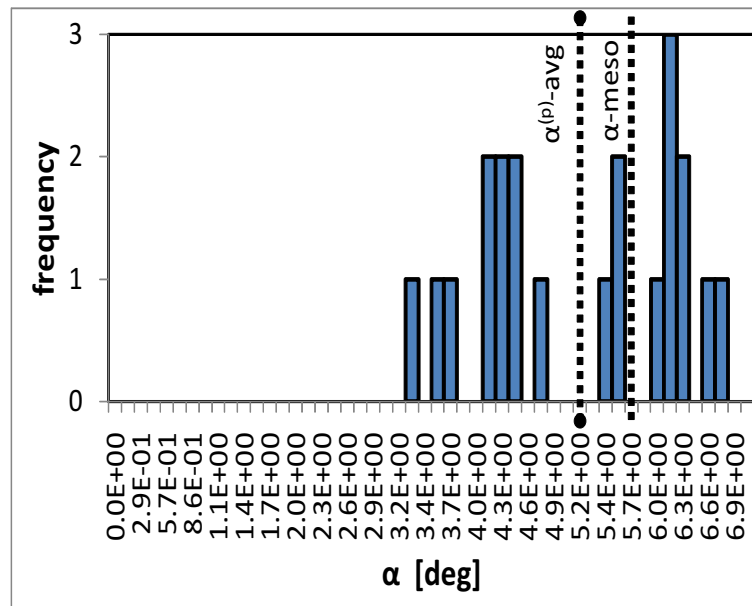


Figure 3.11: Distribution of average rigid body rotations of individual particles in the 12-plane, the particle phase average $\alpha^{(p)}\text{-avg}$ as predicted by the PMA, and the mesoscopic rigid body rotation, $\alpha\text{-meso}$, due to finite shear deformation (corresponding to the IMT prediction).

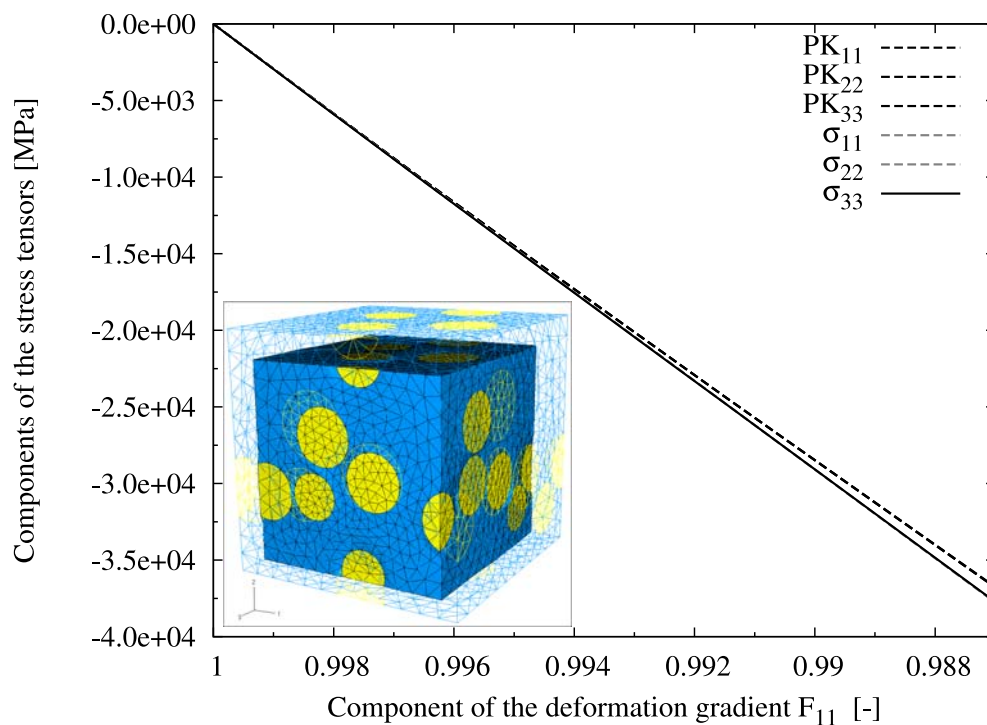


Figure 3.12: Components of the first Piola-Kirchoff and Cauchy stress tensors vs. deformation gradient F_{11} for the hydrostatic load case.

3.4.4 Conclusion

When comparing the IMT results to those of the PMA on the mesoscale, the former's predictions are found to be excellent and the assumptions made in the IMT's formulation are shown to hold. Predictions on the microscale are limited by the inherent mean field assumptions, though, and the PMA is still the tool of choice on these length scales.

An advantage of the IMT is, apart from low computational costs in terms of speed and memory requirements, the possibility to employ a micromechanical constitutive material law to an entire structure or component. To combine the strengths of both methods for predicting the response of a macroscopic metal matrix composite component, the following procedure is suggested. The IMT is employed to provide quick and reliable access to the material response at the mesoscale, where its predictions render excellent results. As the periodic microfield approach is computationally very expensive, it is used for selected regions only if more detail at the fluctuating fields in the phases is required, e.g. to provide information about the onset of damage, particle fracture or interface delamination.

3.5 Mesoscopic strain concentration/localization in periodic unit cells

3.5.1 Problem description, identified conditions, and an approach to prevent mesoscopic strain concentration in the employed unit cells

The periodic unit cells employed in the finite strain predictions show a distinctive behavior with load cases involving shear deformation. In this case, certain regions across the unit cell develop in which the average strain is considerably higher than in other regions of the unit cell. To illustrate this behavior, the "simple shear" load case is studied, which is accomplished by prescribing one of the displacements of master node i , u_i , in j direction ($i, j = 1, 2, 3; i \neq j$)²⁾, e.g. displacement of master node 3 in 2-direction, compare Fig. 3.13. For the following examples, the prescribed master node displacements are chosen to be half a unit cell dimension, clearly exceeding the shear deformation of location "C" in the previous chapter.

All shear load cases show mesoscopic strain concentration behavior with the employed periodic unit cells, compare Fig. 3.14, which presents the final deformation state for all load cases. The accumulated equivalent plastic strain in the region of a plane exhibiting this behavior is several times higher than the average. Shear in the 13- and 23-planes exhibits this behavior in a plane near the top (in 3-direction) of the unit cell, compare Fig. 3.14, middle row left and right, and bottom row right. When the displacements in the 3-direction of master node 2 are prescribed, also resulting in shear in the 23-plane, a plane near the left face (in 2-direction) is activated, compare bottom row left in the figure. The unit cell simulations comprising shear in the 12-plane suffer from convergence problems

²⁾thus, resulting in six sub-load cases

and break off at approximately half the final deformation when compared to the other load cases, so that mesoscopic strain concentrations are visually less evident. Nevertheless, at this time, the equivalent plastic strain exceeds the average in planes near the far side in 2-direction and the near face in 1-direction.

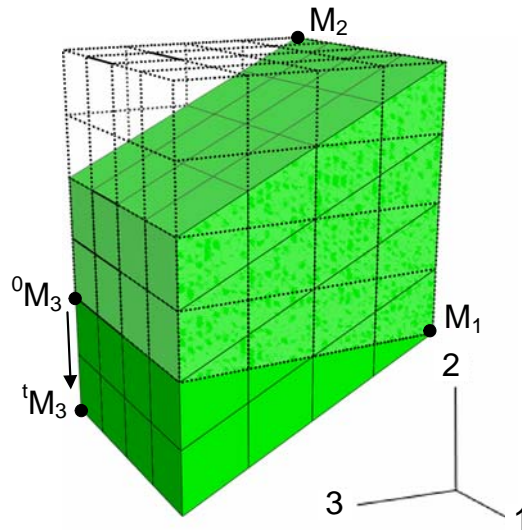


Figure 3.13: Master nodes of the employed unit cell. In this example, master node 3 has a prescribed displacement in 2-direction, resulting in a simple shear load case in the 32-plane.

Conditions identified for mesoscopic strain concentration of periodic unit cells

There are certain conditions identified which must be met for mesoscopic strain concentrations to occur in periodic unit cells: The geometry as well as the boundary conditions of the unit cells have to allow it. The geometric attributes are a sparse distribution of inclusions in a plane normal to the shear plane (which is also a matter of the unit cell size), and a direction of the normal vector defining the plane of maximum shear stress, which is near or coincident with a vector of periodicity of the unit cell.

A transformation approach to prevent mesoscopic strain concentration by making use of the periodic boundary conditions

The results above indicate that the employed periodic unit cell is too small for the given load scenarios. Hence, the question arises how to extract any more information within the scope of the employed tools. The first approach to solve the problem of obviously too small unit cells is the introduction of 'bigger'³⁾ unit cells comprising higher particle counts. However, due to the disproportional⁴⁾ increase in computing time and memory requirements, this is out of question at the present time. The presented method, on the other hand, utilizes the same unit cell, but comprises the transformation of the problem to a coordinate system where the normal to the plane of maximum shear does not coincide with a vector of periodicity of the unit cell, effectively making use of the periodic boundary conditions to break one of the conditions mentioned above. Consequently, unit cell simulations are carried out which transform the evolution of deformation to different coordinate systems with varying angles of rotation to the original system.

³⁾bigger in the sense of increased number of particles while maintaining the same discretization standards

⁴⁾For example, for implicit algorithms, doubling of the cell's edge lengths, resulting in an increase by a factor of 8 in its initial volume, would imply roughly 64-times the computing time.

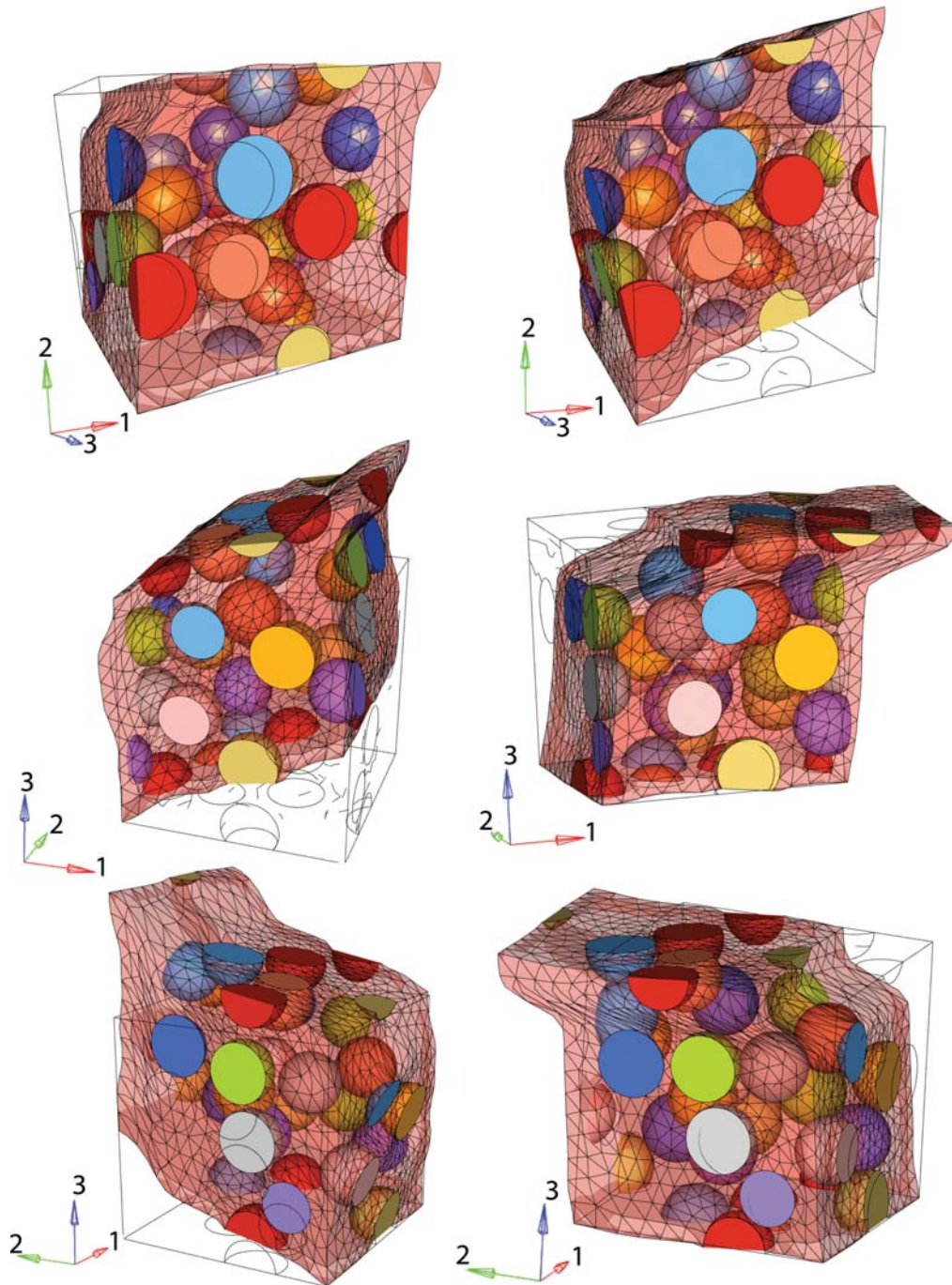


Figure 3.14: The unit cell deformations display mesoscopic strain concentration with simple shear loading. Top row: 12-plane, obtained by displacement of master node 2 in 1-direction (left) and master node 1 in 2-direction (right). Middle row: 13-plane, with prescribed displacement of master node 1 in 3-direction (left) and master node 3 in 1-direction (right). Bottom row: 23-plane, with displacement of master node 2 in 3-direction (left) and master node 3 in 2-direction (right). Deformations are scaled 1:1.

3.5.2 Method

The proposed approach is as follows. First the evolution⁵⁾ of deformation, described by the deformation gradient of the problem, is transformed into a rotated configuration. The master node displacements are determined to perform the simulations in this rotated coordinate system in order to solve the original problem. Homogenization is performed using the reaction forces at the master nodes, compare Eq. (1.20), to provide a transition from the micro to the mesoscopic level. The results, e.g. the Cauchy or the first Piola-Kirchhoff stress tensors, are then transformed back to the original coordinate system.

It is essential to understand that the same problem of macroscopic deformation is solved, just in a different coordinate system⁶⁾. This can be seen (and in practice is checked) on the spectral decomposition of the right Cauchy-Green tensor, compare Eq. (1.25). The Eigenvalues as well as the Eigenvectors of the right Cauchy-Green tensor of the rotated and the original problem have to be identical, minding their invariance to rotation of the material system. Given the polar decomposition, Eq. (1.24), the same holds true for the left and right stretch tensors. For the simple shear example, the rigid body rotation at any state of deformation is the component R_{ij} of the orthogonal rotation tensor, $\mathbf{R}(\alpha)$, for shear in the ij -plane, ($i, j = 1, 2, 3; i \neq j$).

3.5.3 Example and results

The approach is presented on the example of simple shear in the 23-plane. The considered load case is accomplished by prescribing the displacement of master node 3 in the 2-direction. The associated transformation is described in the original, unrotated coordinate system by

⁵⁾with respect to the FEM, this is done in terms of time increments

⁶⁾However, this does not imply that the microscopic response is equal – see later.

$${}^0\mathbf{F} = \begin{pmatrix} 1 & 0 & 0 \\ 0 & 1 & 0 \\ 0 & 0 & 1 \end{pmatrix} \longrightarrow \begin{pmatrix} 1 & 0 & 0 \\ 0 & 1 & 0 \\ 0 & 0.5 & 1 \end{pmatrix} = {}^{t_e}\mathbf{F} , \quad (3.5)$$

where time t_e marks the end of transformation. The deformation, described in a system which is rotated by, e.g, $\alpha = \pi/4$ reads

$${}^{t_e}\mathbf{F}' = \begin{pmatrix} 1 & 0 & 0 \\ 0 & 1.25 & -0.25 \\ 0 & 0.25 & 0.75 \end{pmatrix} , \quad {}^{t_e}\mathbf{U}' = \begin{pmatrix} 0 & 0 & 0 \\ 0 & 0.25 & -0.25 \\ 0 & 0.25 & -0.25 \end{pmatrix} , \quad (3.6)$$

with ${}^{t_e}\mathbf{U}'$ being the associated master node displacements to achieve this final state of deformation.

Fig. 3.15 presents results obtained with angles of rotation, α , of $\pi/4$, $\pi/6$, and $\pi/12$, respectively, and also shows the associated final deformations of the individual unit cell configurations. Transformation of the deformation gradient results in different master node displacements for attaining the prescribed deformation, giving rise to certain reaction forces at these master nodes. These master node displacements and reaction forces are plotted to scale at the bottom of Fig. 3.15. Note that the out-of-plane displacements (direction 1) of the unit cells are constrained in order to prescribe all 12 degrees of freedom of the master nodes - hence this is a plane strain problem by design.

For the PMA, the multi-particle periodic unit cell from the previous chapter, taken from [Böhm et al., 2004], is employed (twenty spherical inclusions, 20% particle volume fraction, tetrahedral continuum elements), compare Fig. 3.16. The master node concept is utilized to apply mesoscopic deformations. As mesoscopic responses, the master node reactions of the unit cells are evaluated in terms of first Piola-Kirchhoff stresses. The results are also

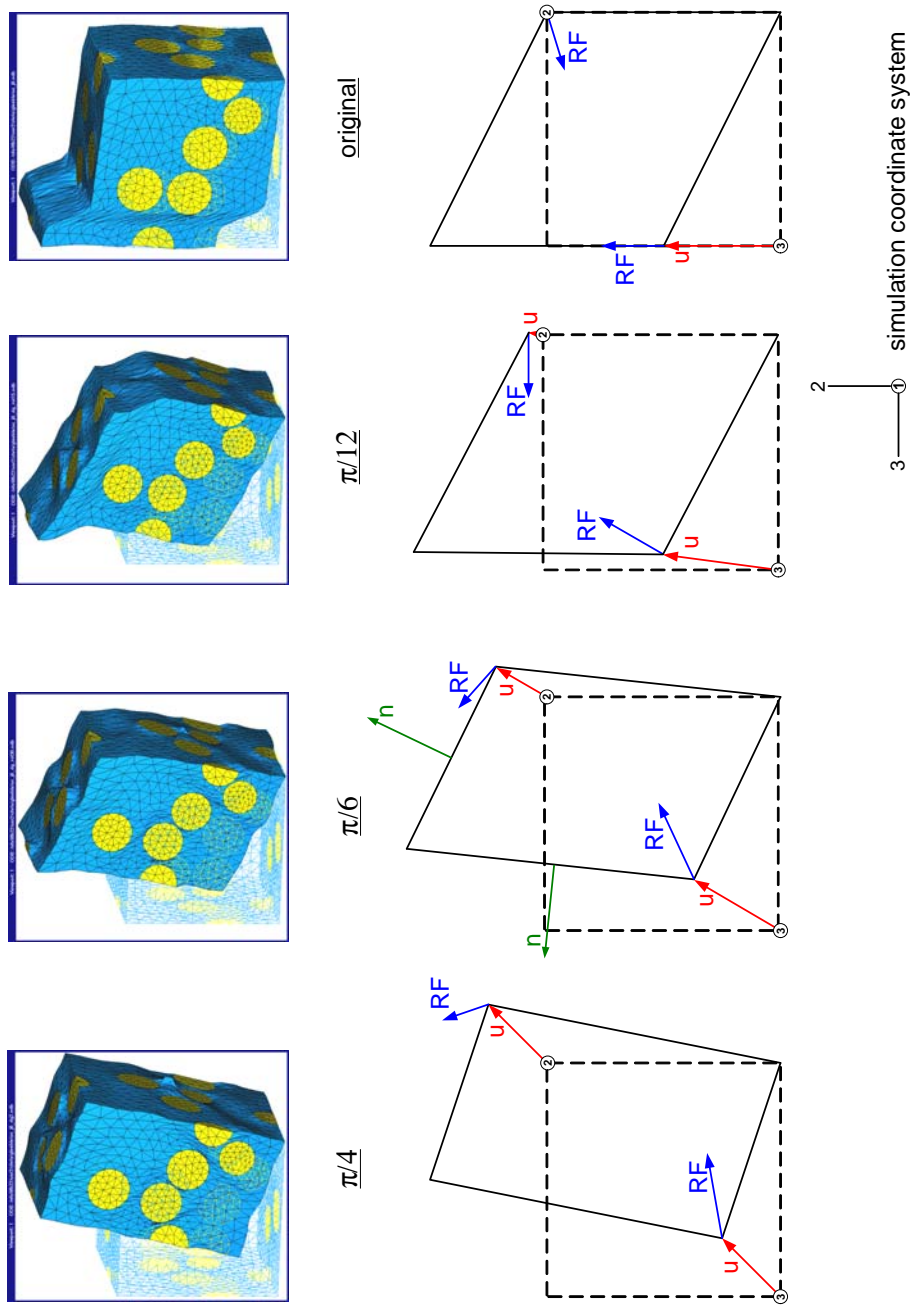


Figure 3.15: The final state of mesoscopic deformation of the individually rotated configurations of the unit cell simulations, all describing the same deformation gradient but in different coordinate systems (left). The right hand side of the figure shows the prescribed displacements (' u ') of master nodes 2 and 3 in the rotated system and the resulting reaction forces (' RF ') at these nodes. Ideal plastic material behavior is employed.

compared to the IMT prediction for this load scenario. For the IMT simulations, a very simple "unit cell" is employed, since information about geometry (in a statistical sense) and volume fraction of the inclusions is already contained in the analytical part of the method. Since the unit cell response is already "homogenized" due to the nature of the IMT approach, a single element cell is adequate for material response description⁷⁾.

The same elastic material parameters as in the previous chapter are used, compare Table 3.1. Again, the matrix is taken to behave elasto-plastically and the inclusions are linear elastic. The adopted flow curves of the matrix are shown in Fig. 3.17 – ideal plastic, strain hardening and strain softening are considered. Both phases are isotropic and share a perfect interface. No damage is assumed to occur throughout the loading history, nor does creep or relaxation. Temperature effects are not considered.

⁷⁾However, an existing 4x4x4 element unit cell with periodic boundary conditions is employed as the difference in computation time is negligible.

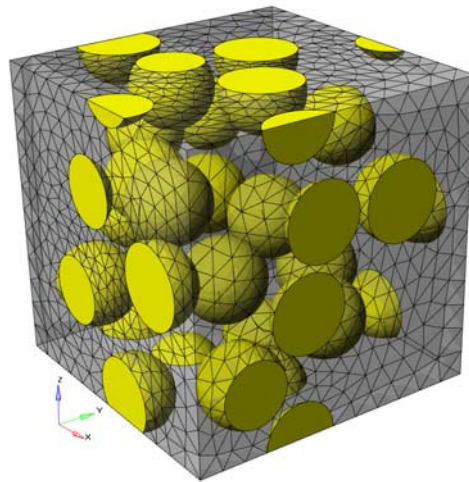


Figure 3.16: The periodic unit cell used in the simulations, employing 20 randomly distributed particulate inclusions [Böhm et al., 2004]. The matrix material is set semitransparent to display the individual particles and to facilitate envisioning of the periodicity. Particle mesh is masked for better visibility.

Ideal plastic matrix behavior

The resulting unit cell deformations for this load case, comprising ideal plastic matrix behavior, are presented in Fig. 3.15. The plane of strain concentration can change within the 23-shear problem even for a moderately small rotation, which can be observed on the different deformation 'characters' of the unrotated and the $\pi/12$ rotated configuration. For a rotation of $\pi/6$, the strain concentration is somewhat muted and for a rotation of $\pi/4$ it is prevented. No plane normal to the shear plane and coincident with a vector of periodicity at the same time is sparse enough (in terms of inclusions) to trigger the phenomenon.

The results of the simulations, in terms of the evolution of the components of the first Piola Kirchhoff stress tensor with deformation, are plotted in Figs. (3.18 - 3.21). Since the first Piola Kirchhoff stress tensor, \mathbf{P} , is unsymmetric, all nine components are plotted. The smaller of the shear components within the 23-shear plane is coincident with the respective Cauchy component because the associated reference area does not change. As the out-of-plane displacement (the 1-direction) of the unit cells is constrained, there are nonzero components of the stress tensors in the other principal directions since the load

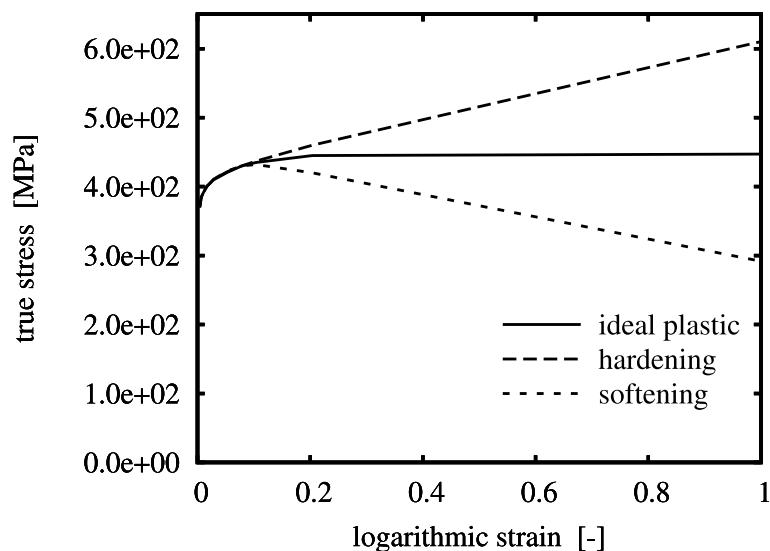


Figure 3.17: Different uniaxial stress-strain curves for the matrix material comprising strain hardening and softening.

case does not represent pure shear neither a plane stress situation. Furthermore, there are nonzero (but very small) out-of-plane shear components because the unit cell is too small to exactly show isotropic behavior.

Although some individual fluctuations arise⁸⁾, the mesoscopic behavior of the individual rotated unit cells in terms of the components of the stress tensors is not so different like one would assume from looking at the strongly varying deformation presented in Fig. 3.15, because the matrix material comprises ideal plastic behavior. The Mori-Tanaka yield limits for the matrix of an MMC with 20%vol randomly dispersed isotropic reinforcements with aspect ratio 1, employing the same material data as above, are 420MPa for the effective uniaxial yield limit, and 242MPa for the effective shear yield limit. Onset of yielding in the FEM simulations is the same for all unit cell configurations and is found to be approximately 220MPa. The simulations employing the IMT as constitutive law have to match the Mori-Tanaka value from above, as the calculations are inherently based on the same micromechanical model and material, compare Fig. 3.22. However, the mesoscopic strain concentration has an effect on the original configuration (and, somewhat diminished, also on the $\pi/12$ -rotated unit cell configuration), as the level of the shear stresses associated with the simple shear load in the 23-plane, \mathbf{P}_{23} , $\mathbf{P}_{32} = \boldsymbol{\sigma}_{23}$ is higher in the rotated than in the unrotated unit cell configurations. A comparison of these shear stress components only, for all unit cell configurations, is presented in Fig. 3.23.

Results are very similar for the other simple shear load cases (not presented).

⁸⁾which is also an indication of the employed unit cell being too small

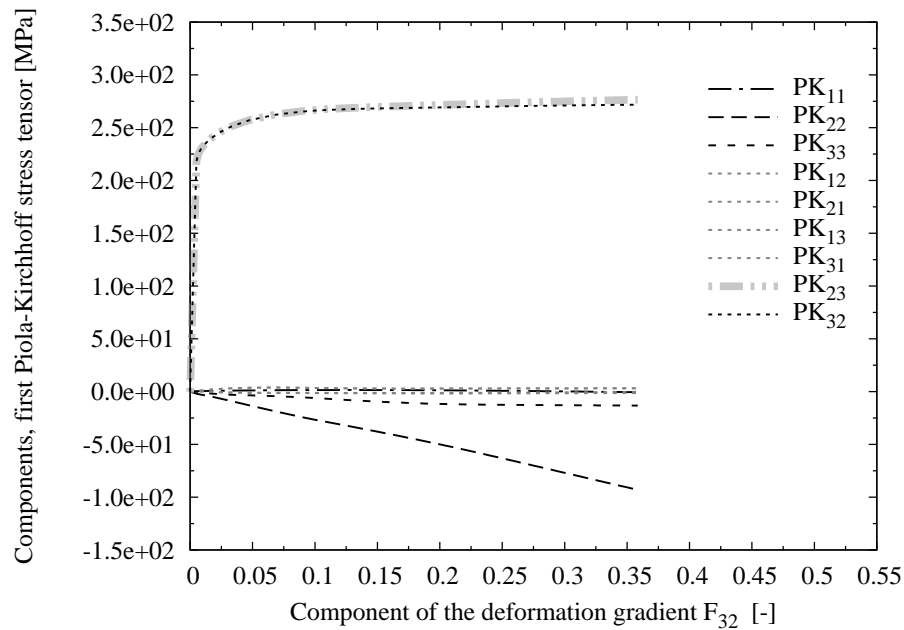


Figure 3.18: Components of the mesoscopic 1st Piola-Kirchhoff stress tensor vs. the mesoscopic deformation gradient F_{32} for the original, non-rotated unit cell, for shear stress in the 23-plane and ideal plastic matrix material. Note that the simulation stops at $F_{32}=0.36$ due to convergence problems caused by excessively distorted elements.

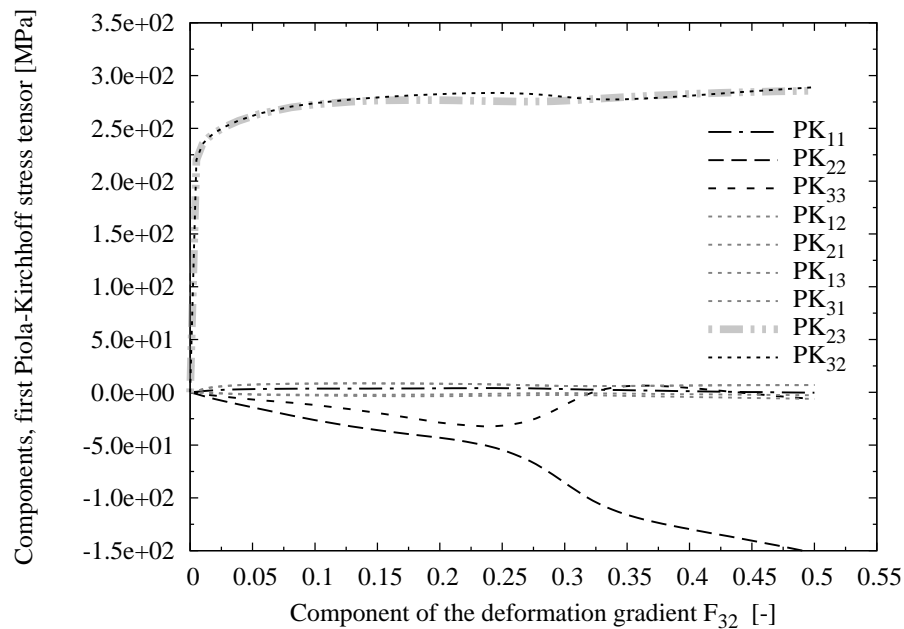


Figure 3.19: Components of the mesoscopic 1st Piola-Kirchhoff stress tensor vs. the mesoscopic deformation gradient F_{32} for the $\pi/12$ -rotated unit cell, for shear stress in the 23-plane and ideal plastic matrix material.

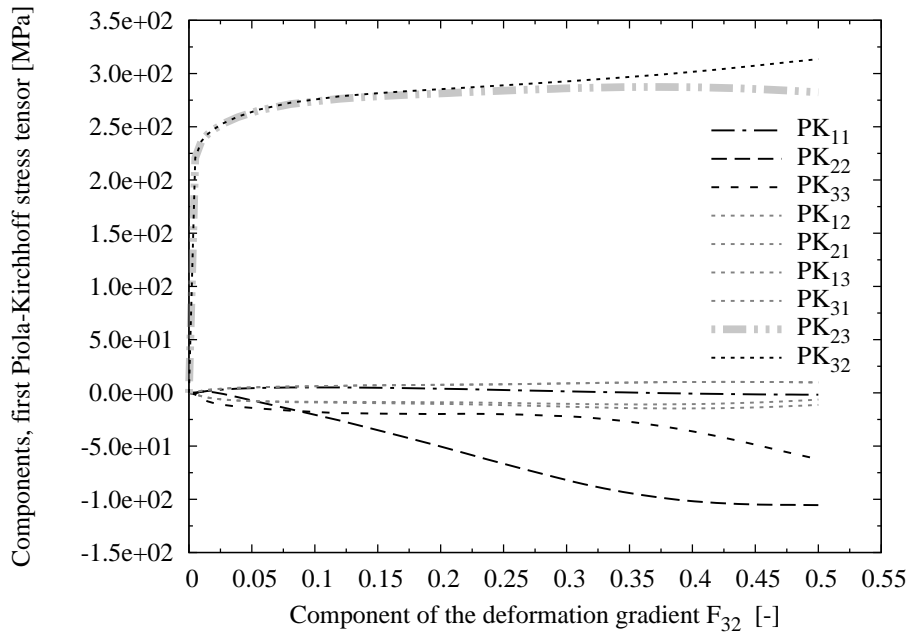


Figure 3.20: Components of the mesoscopic 1st Piola-Kirchhoff stress tensor vs. the mesoscopic deformation gradient F_{32} for the $\pi/6$ -rotated unit cell, for shear stress in the 23-plane and ideal plastic matrix material.

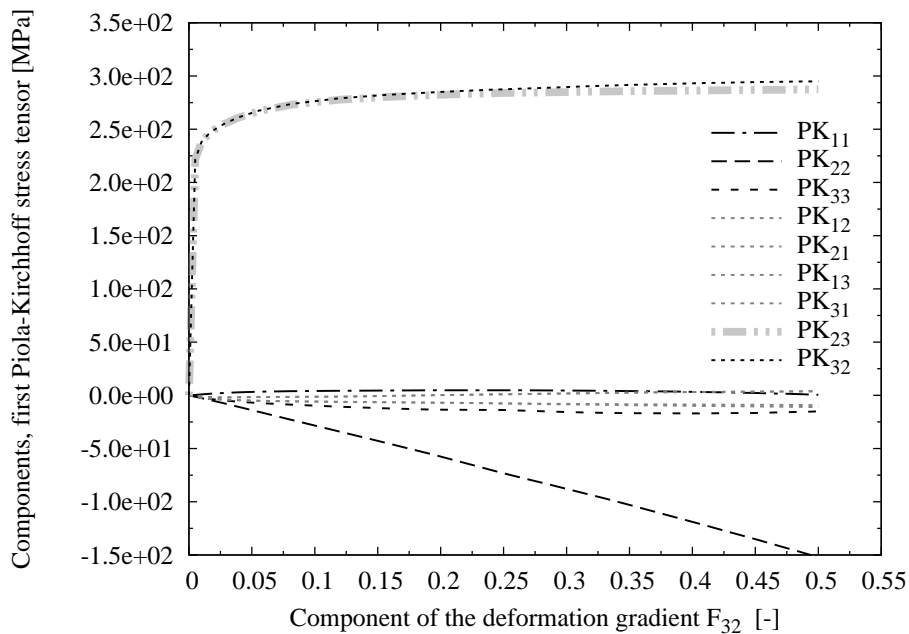


Figure 3.21: Components of the mesoscopic 1st Piola-Kirchhoff stress tensor vs. the mesoscopic deformation gradient F_{32} for the $\pi/4$ -rotated unit cell, for shear stress in the 23-plane and ideal plastic matrix material.

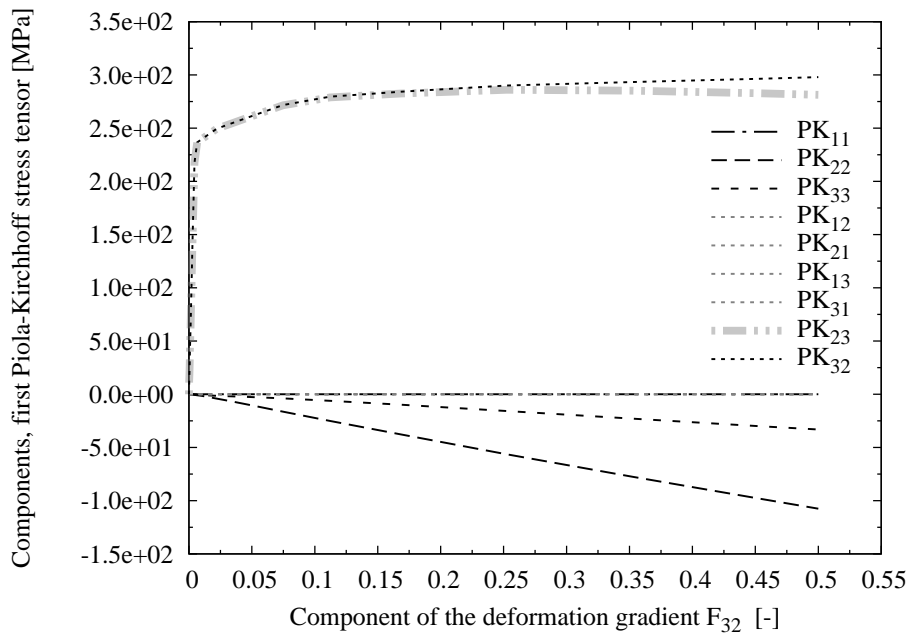


Figure 3.22: Components of the mesoscopic 1st Piola-Kirchhoff stress tensor vs. the mesoscopic deformation gradient F_{32} for the unit cell employing the IMT as constitutive law, for shear stress in the 23-plane and ideal plastic matrix material.

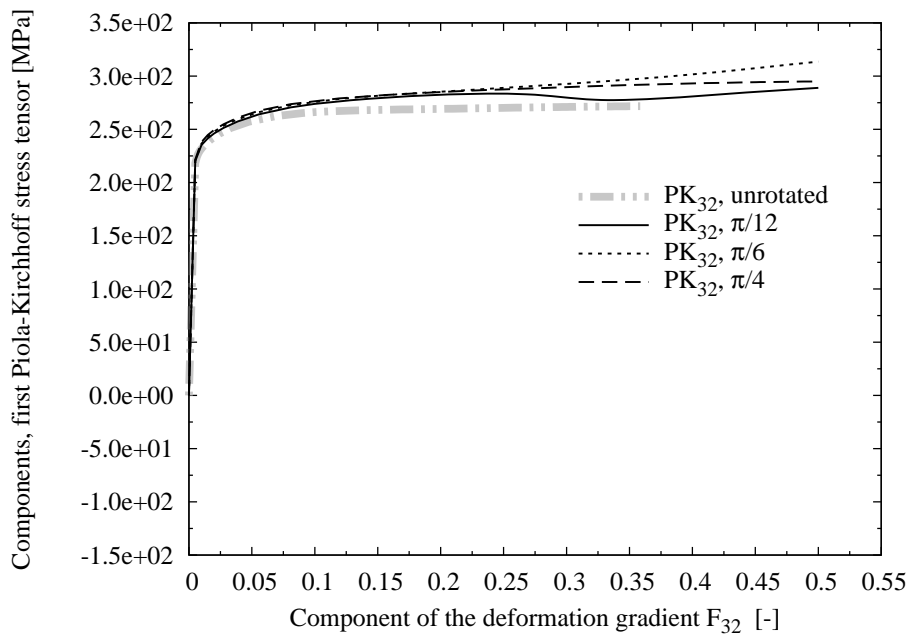


Figure 3.23: Comparison of the mesoscopic first Piola-Kirchhoff tensor components in the 23-plane vs. the mesoscopic deformation gradient F_{32} , of the original as well as the non-rotated unit cells; for shear stress in the 23-plane. The difference between the individual configurations is small for an ideal plastic matrix material.

Influence of strain hardening and softening behavior of the matrix material

The problem significantly changes if the matrix behavior shows strain softening behavior. The adopted flow curve for this case is shown in Fig. 3.17. The effect of transforming the deformation to a rotated coordinate system becomes more pronounced, compare Figs. 3.24 and 3.25, which comprise all stress tensor components. The shear components in the 23-plane of unrotated and $\pi/4$ -rotated configurations are individually compared in Fig. 3.28(top), which contains also the final deformation of the unit cells. Although both results resemble the changed matrix behavior, the non-rotated unit cell shows significantly more softening. In fact, mesoscopic strain concentration is superseded by localization in this case. It is noted that such problems show mesh dependence unless non-local or regularized formulations are employed, which is beyond the scope of the present work.

For significant strain hardening behavior of the matrix material, however, the differences in the individual configurations become very small, compare Figs. 3.26 and 3.27; with individual comparison of the stress tensors' shear components and the final deformation in Fig. 3.28(bottom). This is mostly due to the fact, that the non-rotated unit cell builds up no or very small mesoscopic strain concentration in the first place because of stress re-distribution.

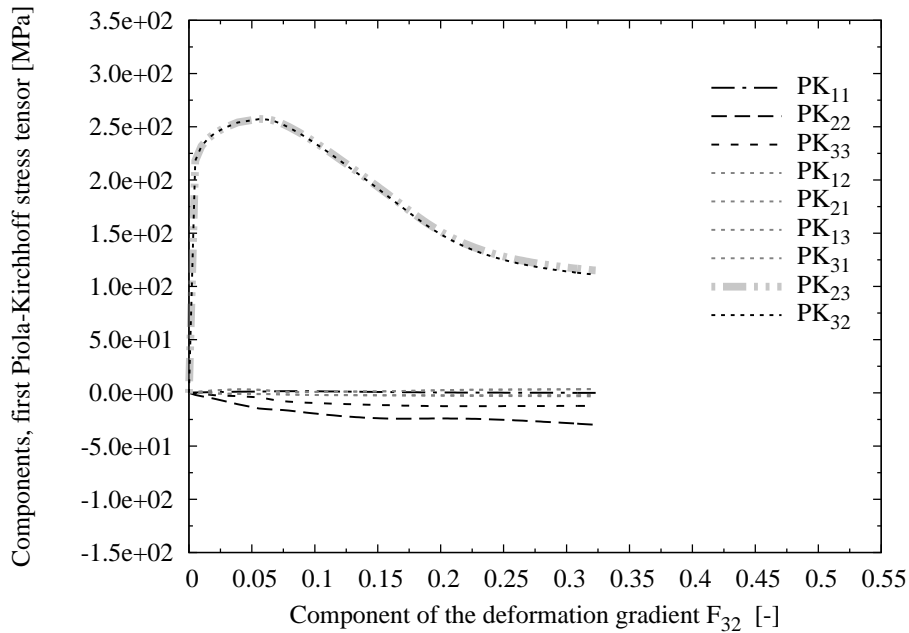


Figure 3.24: Components of the mesoscopic 1st Piola-Kirchhoff stress tensor vs. the mesoscopic deformation gradient F_{32} for the unrotated unit cell, for shear stress in the 23-plane and matrix material with softening behavior.

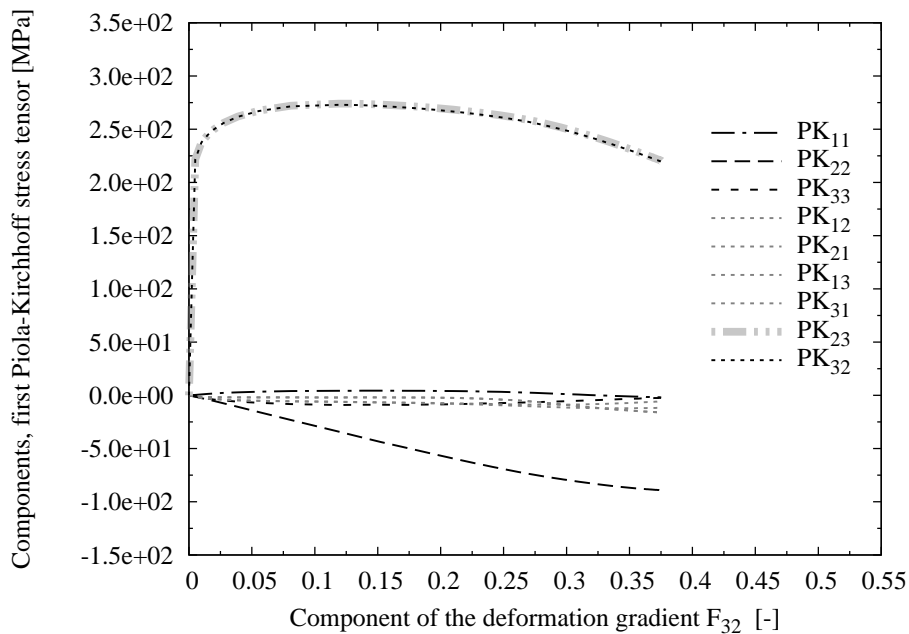


Figure 3.25: Components of the mesoscopic 1st Piola-Kirchhoff stress tensor vs. the mesoscopic deformation gradient F_{32} for the $\pi/4$ -rotated unit cell, for shear stress in the 23-plane and matrix material with softening behavior.

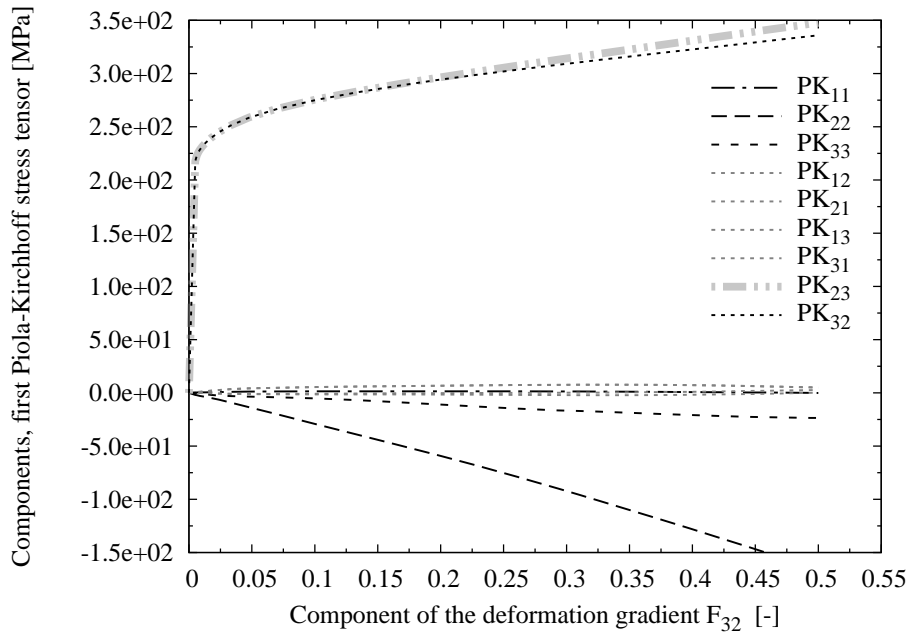


Figure 3.26: Components of the mesoscopic 1st Piola-Kirchhoff stress tensor vs. the mesoscopic deformation gradient F_{32} for the unrotated unit cell, for shear stress in the 23-plane and matrix material with strain hardening behavior.

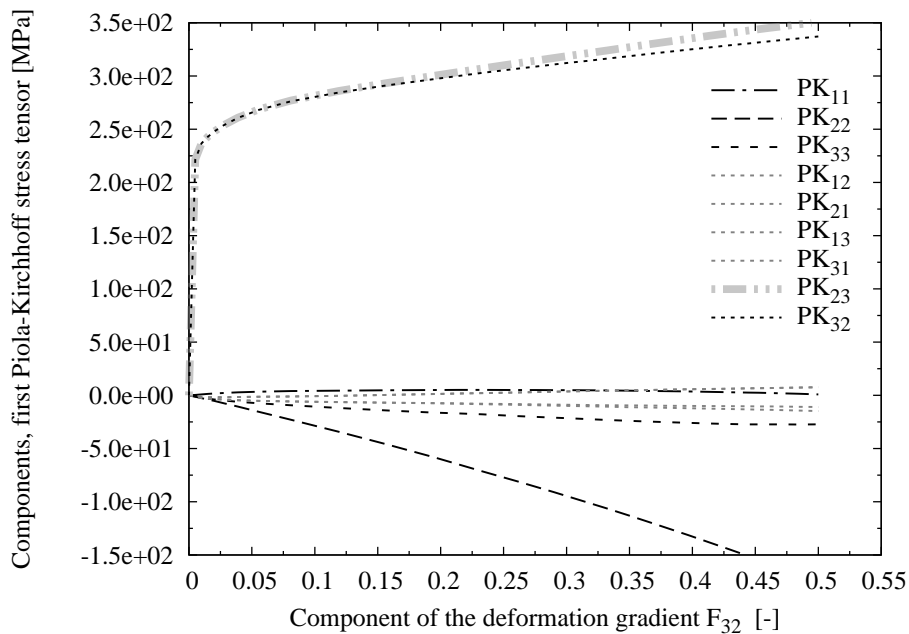


Figure 3.27: Components of the mesoscopic 1st Piola-Kirchhoff stress tensor vs. deformation gradient F_{32} for the $\pi/4$ -rotated unit cell, for shear stress in the 23-plane and matrix material with strain hardening behavior.

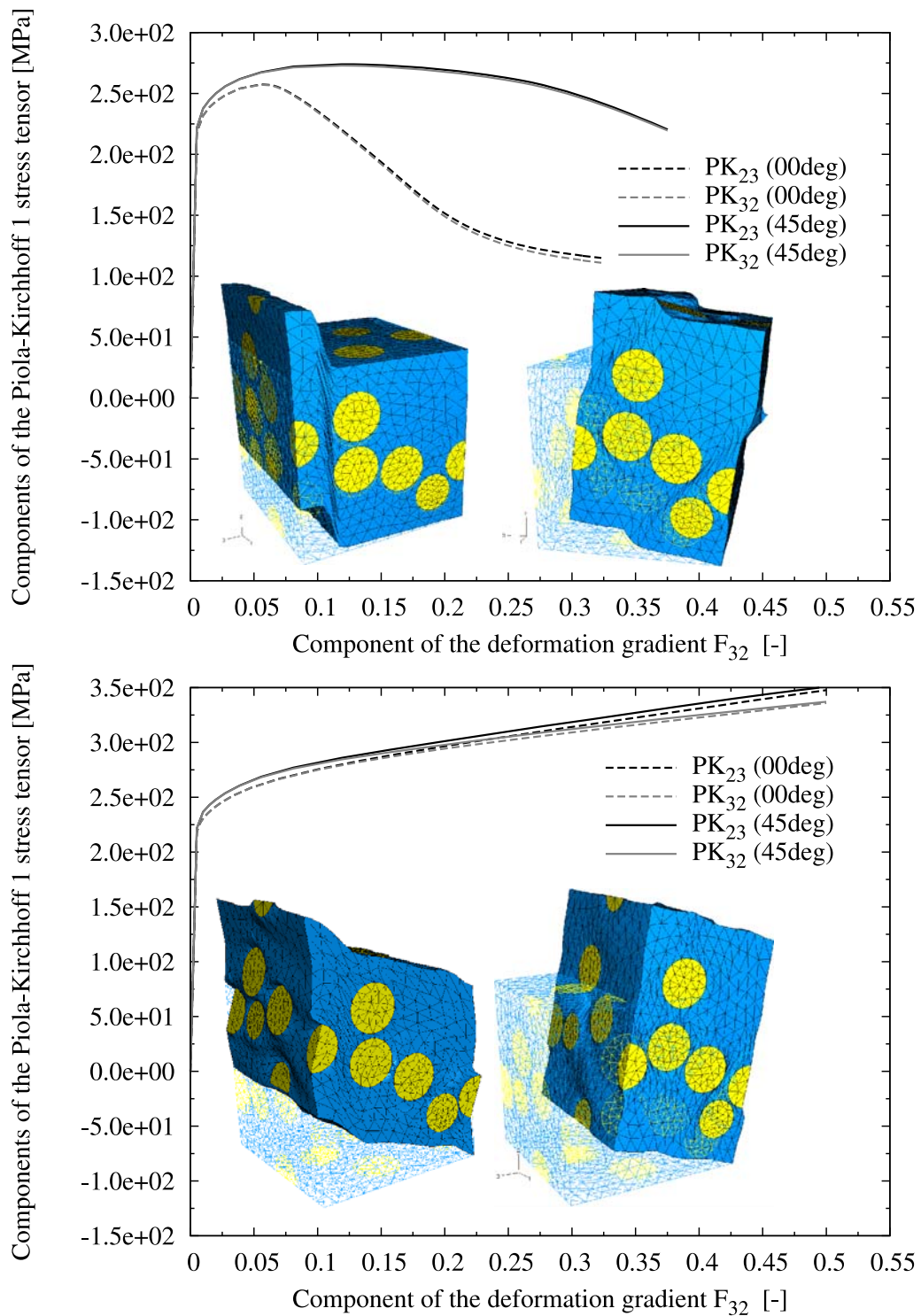


Figure 3.28: Comparison of the components 23 and 32 of the mesoscopic Piola-Kirchhoff 1 stress tensor vs. the mesoscopic deformation gradient F_{32} , for shear stress in the 23-plane. The matrix shows strain softening (top) or strain hardening (bottom), and unit cell deformation is shown for the unrotated (left) and $\pi/4$ -rotated (right) configuration, respectively.

3.5.4 Conclusion

Concerns arise how the results are to be interpreted. The question which is the better or more accurate solution cannot be answered satisfactorily, as it is conceivable that mesoscopic strain concentration may well be a valid response of the actual material. The transformation approach makes use of the boundary conditions to the effect that mesoscopic strain concentration is in fact 'filtered', because a concentration band running across the unit cell is only possible for certain angles of rotation. For periodic unit cells these angles are 0 , $\pi/4$, and $\pi/2$. Thus, new constraints are introduced to the unit cell via the periodic boundary conditions, which are angular dependent. The equality in the mesoscopic deformation does not imply that the underlying microfields are equal as well, which shows in the – dependent on matrix behavior – noticeable differences of the individual configurations. If a material model comprising damage or failure is employed for one of the constituents, which is sensitive to variations in the microfields, a significant difference in the behavior of the rotated configurations is expected. However, the present method is a practical approach for obtaining the unit cells' homogenized behavior.

A conclusion that most certainly can be drawn from the of from the simulations is that the employed unit cell is too small for load scenarios considerably immersing into the finite strain regime.

3.6 Comparison of the two constitutive laws, J2-plasticity and Incremental Mori-Tanaka

In the previous sections, an MMC has been treated with micromechanical methods, in particular the IMT approach. The question arises how large an error is made (on the mesoscopic level) if the behavior of the inhomogeneous material is described by a homogeneous, isotropic material model employing the uniaxial stress-strain curve of the MMC and adopting J2-plasticity for the post-yield regime.

3.6.1 Method

For this comparison, a 'quasi'-MMC material is modeled, using homogenized elastic parameters and adopting the flow curve obtained with the IMT with 20%vol particles. The homogenized elastic material parameters are listed in Table 3.2, and the uniaxial flow curves are shown in Fig. 3.29. The homogenized material ('MMC-J2') is adjusted to fit the IMT behavior. The logarithmic plastic strain required for the definition of the MMC-J2 flow curve in ABAQUS is determined from the uniaxial IMT flow curve, minding the additive decomposition of strains, by subtracting the elastic part of the strains from the total strains, reading

$$\epsilon_{11}^{\ln} = \ln(1 + \epsilon_{11}^{\text{nom}}) - \frac{\sigma_{11}}{E_1^*} , \quad (3.7)$$

with $\epsilon_{11}^{\text{nom}}$ being the nominal (linear) strain; E_1^* is the homogenized Young's modulus and $1 + \epsilon_{11}^{\text{nom}}$ is the principal stretch λ_1 .

The comparison of IMT to J2-plasticity comprises various standard load histories employed on a single element, the material behavior of which is described by either these two constitutive laws. As the MMC-J2 model represents a homogenized material, predictions are

Table 3.2: Homogenized elastic material parameters for the MMC material.

Young's Modulus	E^*	[GPa]	127
Poisson's Ratio	ν^*	[-]	0.28
Yield stress	σ_y	[MPa]	420

restricted to the mesoscale.

3.6.2 Example, mesoscopic results, and conclusion

Several load cases are considered. A *biaxial stress state* is achieved by prescribing displacements in 1- and 2-direction, $u_1 = u_2$ (a radial load path), resulting in tensile stress $\sigma_{11} = \sigma_{22}$ in the respective directions, compare Fig. 3.30. Prescribing the displacement in 1-direction, $-u_1$, and constraining displacements in 2-direction results in pressure in 1- and 2-directions, defining a *confined compression*, compare Fig. 3.31. *Uniaxial strain* is

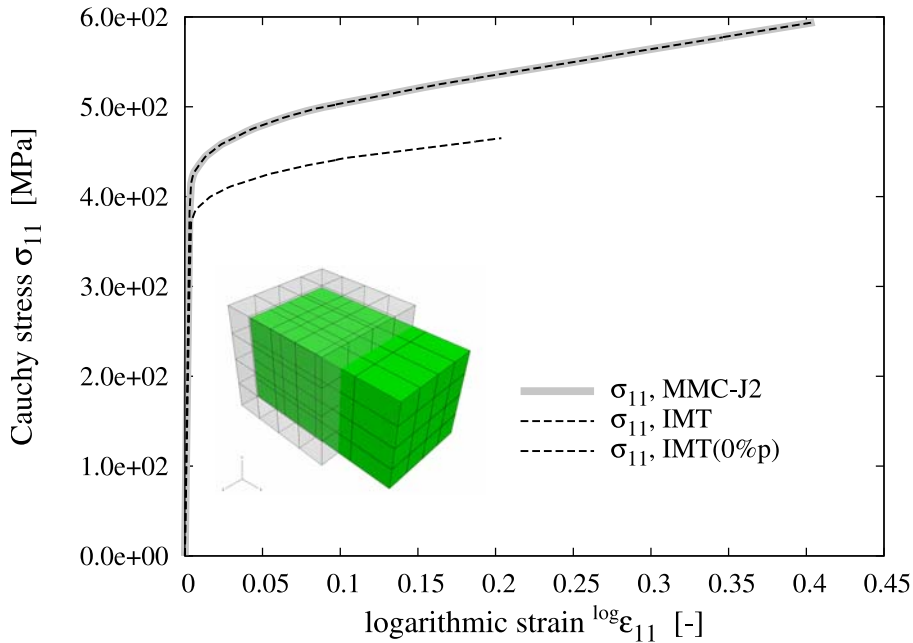


Figure 3.29: Flow curves of the investigated materials for the uniaxial stress load case. The MMC is described by J2-plasticity (MMC-J2), fitted to the IMT uniaxial behavior. For comparison, the respective behavior of the matrix material, IMT(0%p), is also presented.

achieved by prescribing a displacement in 1-direction, u_1 , and constraining the displacements in 2- and 3-directions, resulting in tensions σ_{11} and $\sigma_{22} = \sigma_{33}$, a triaxial stress state, compare Fig. 3.32. Finally, the *simple shear* load case is obtained by prescribing a displacement of master node 3 in 2-direction, u_{32} , resulting in stresses σ_{23} , and small contributions σ_{22} and σ_{33} , compare Fig. 3.33.

For all considered load scenarios, the difference in response between the IMT and the homogenized MMC is subtle at best. For the given material with a particle volume fraction of 20%vol, the error produced by employing J2-plasticity is small. However, with this approach access to the microscopic level is lost – predictions on this level are only possible employing the IMT, unit cell analyses or similar micromechanical approaches.

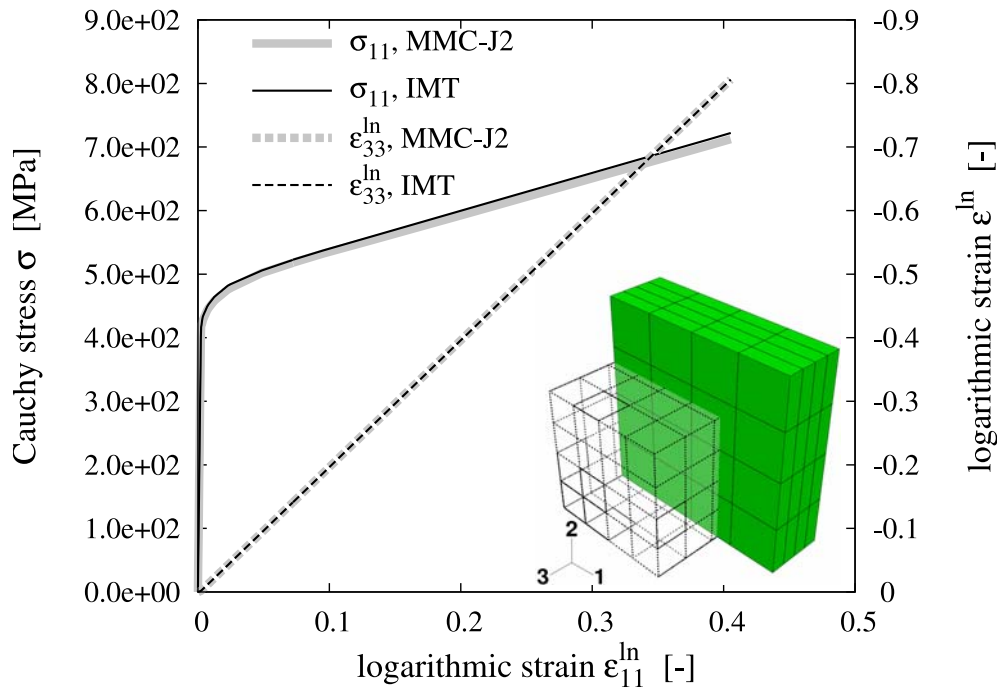


Figure 3.30: Comparison of the IMT to J2-plasticity. Flow curves of the investigated materials for the biaxial stress load case ($\sigma_{11} = \sigma_{22}$); the second ordinate shows the logarithmic strain in 3-direction.

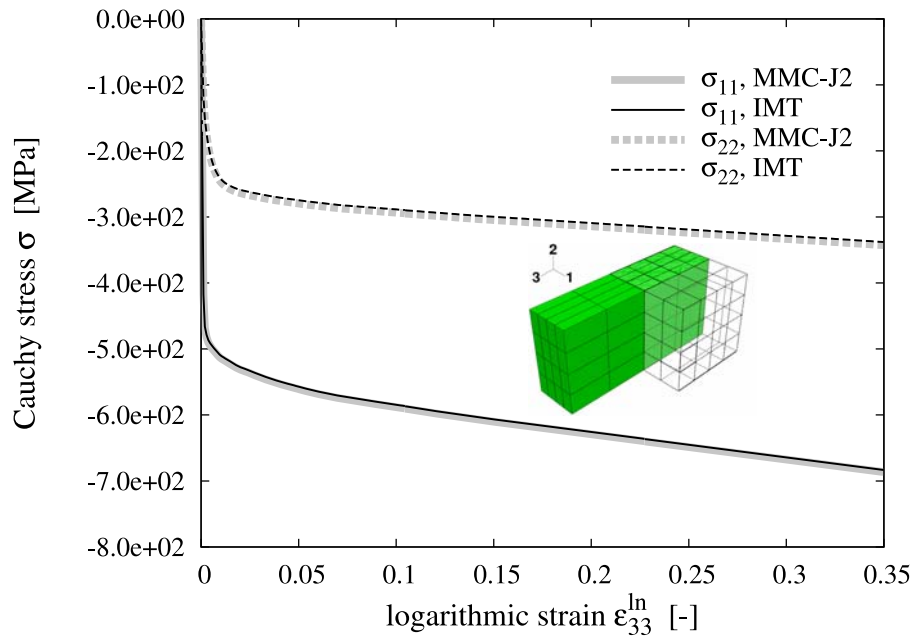


Figure 3.31: Comparison of the IMT to J2-plasticity. Flow curves of the investigated materials for the confined compression load case.

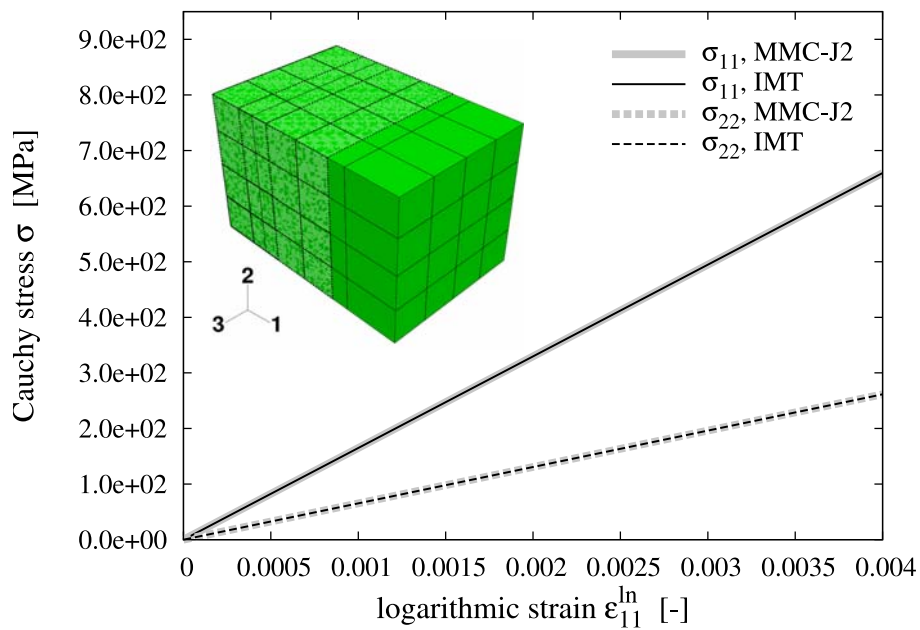


Figure 3.32: Comparison of the IMT to J2-plasticity. Flow curves of the investigated materials for the uniaxial strain load case.

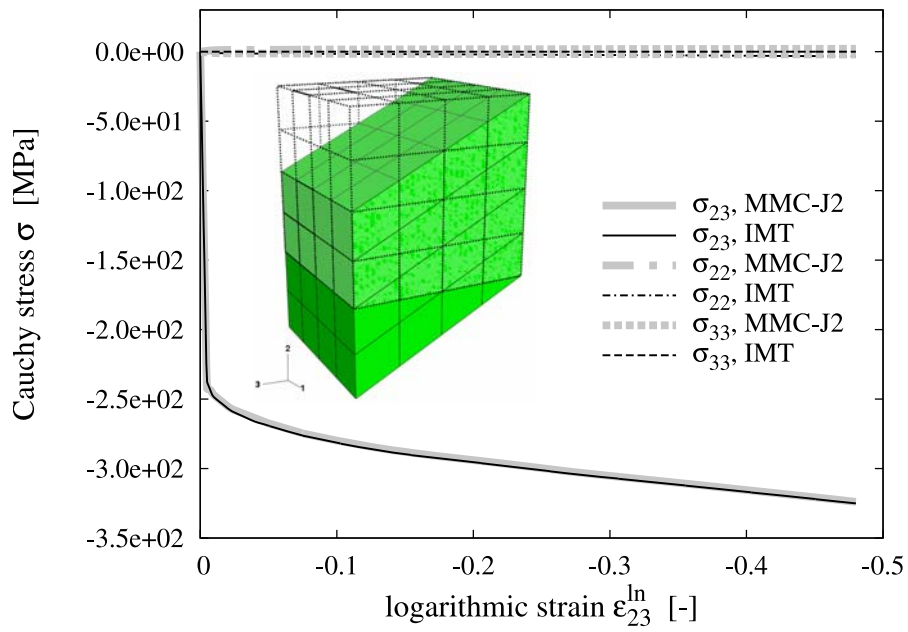


Figure 3.33: Comparison of the IMT to J2-plasticity. Flow curves of the investigated materials for the simple shear load case.

3.6.3 Incremental Mori-Tanaka hardening behavior

A simple test is performed to determine if the IMT has a homogenized hardening behavior which deviates from J2–isotropic hardening behavior. The test is chosen to take place in the $\sigma_{11} - \sigma_{22}$ stress space, involving three cycles of uniaxial stress in σ_{11} direction (step time 0..5), after which σ_{11} is reduced to zero (step time 5..6), followed by 2 cycles of uniaxial stress in the σ_{22} direction (step time 6..10), compare Fig. 3.34 (top). The simulation is displacement controlled. The input, in terms of the displacements of the master nodes 1 and 2, is shown in Fig. 3.34 (bottom). During the prescribed displacement of master node 1, master node 2 is free and vice versa. Note that the elastic strains are small compared to the plastic ones and yielding in the opposite direction is obtained shortly after changing the direction of displacement. Because presentation of the time histories of the stresses is not very intuitive, the resulting stresses are also presented versus the logarithmic strain ϵ_{11}^{ln} , compare Fig. 3.35. Note that in this case, the elastic slope of the σ_{22} -cycles is negative and approximately five times steeper because σ_{22} is also plotted versus ϵ_{11} and the Poisson's ratio $\nu_{12} = -\epsilon_{22}/\epsilon_{11}$ is about 0.2.

No indications are given that the strain hardening behavior of the IMT causes the yield surface to be non-isotropic. However, there is a small shift when switching from the σ_{11} -cycles to σ_{22} -cycles, which is irrelevant for practical purposes.

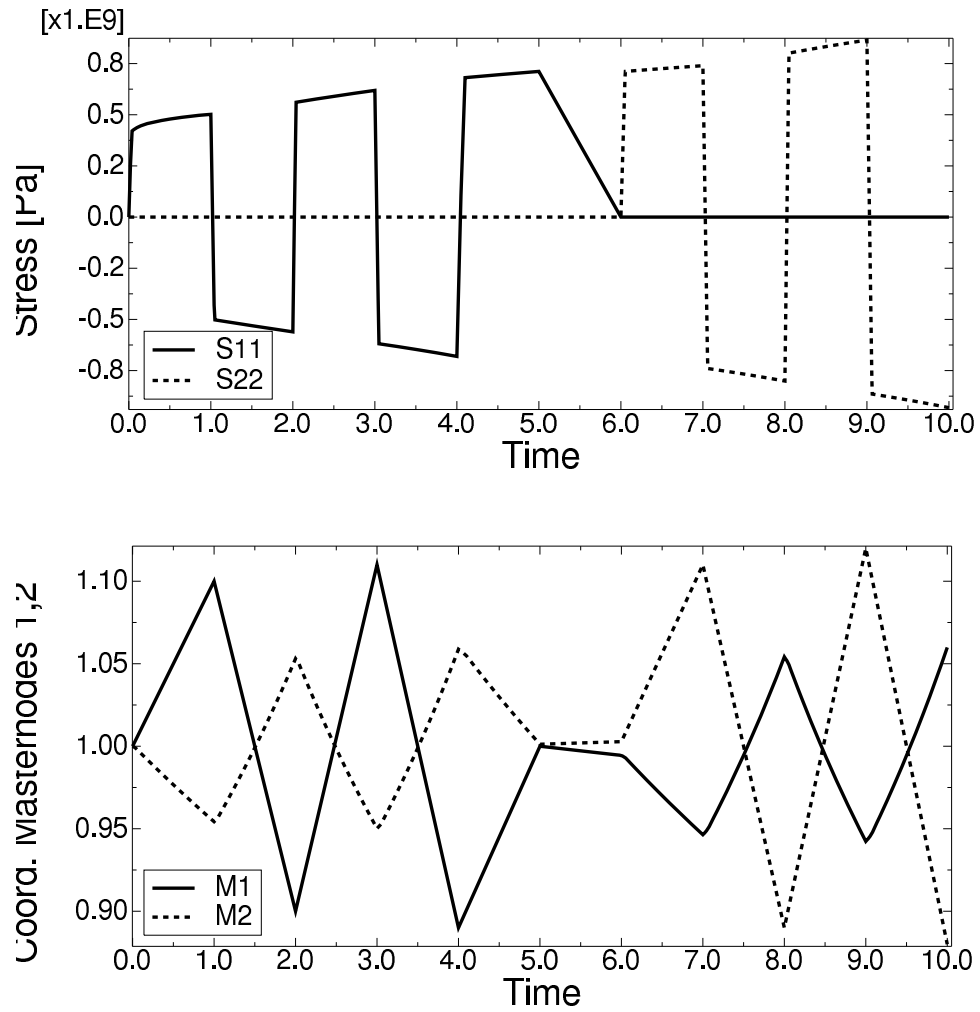


Figure 3.34: Stresses σ_{11} and σ_{22} vs. time (top); the respective coordinates of master nodes 1 and 2 (bottom).

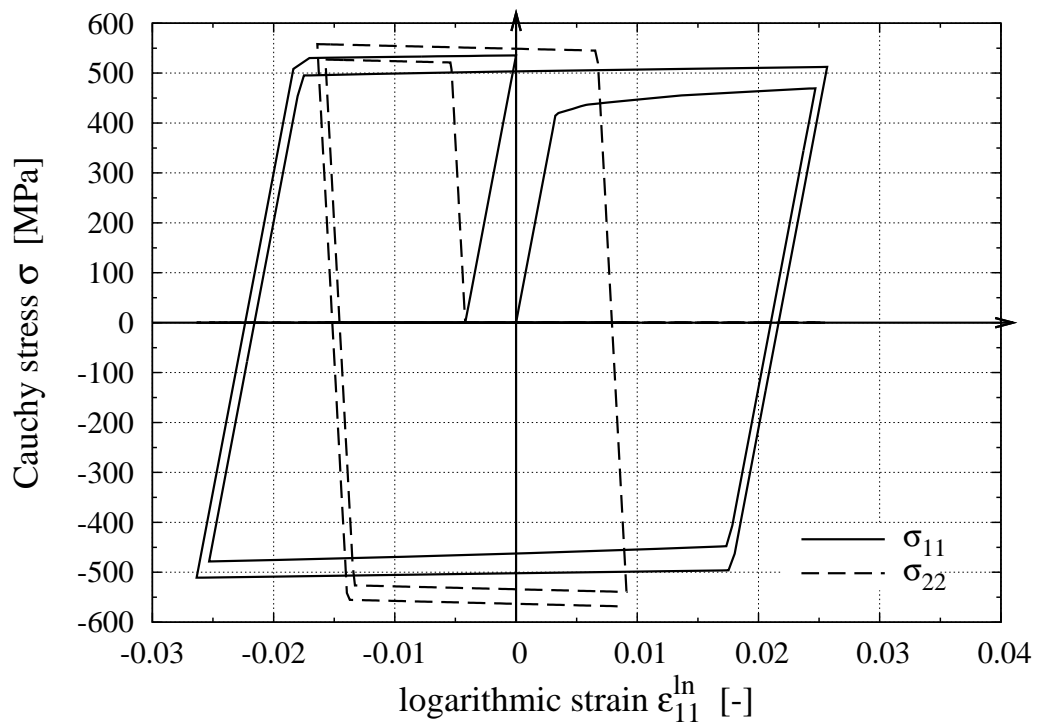


Figure 3.35: Stresses σ_{11} and σ_{22} vs. logarithmic strain ϵ_{11}^{\ln} .

Chapter 4

Summary

Computational simulations of Metal Matrix Composites (MMCs) are performed with the aim to improve computational predictions of the thermo-mechanical behavior in frictional contact (Chapter 2) and of the elasto-plastic properties of MMCs undergoing finite strains (Chapter 3). A hierarchical approach employing micromechanical methods within the continuum mechanics framework is followed.

Chapter 2 deals with computational predictions of the tribological behavior of MMCs, where the influence of particle volume fraction and clustering of particles is investigated at different length scales. Finite Element simulations are performed employing periodic unit cells with both homogeneous random and clustered distributions. Based on these experiences, numerical simulations employing the Finite Element Method (FEM) of the frictional behavior of a MMC material, including heat conduction in the steady state, are performed. Experiments and analytical calculations jointly serve to determine unknown process parameters by means of a simplified, homogenized model, whereas in the FEM simulations, the inhomogeneous body is considered. The validity of the FE continuum mechanics of materials approach utilizing unit cells is demonstrated in case of undercritical conditions. However, limitations of the thermo-elastic FEM predictions are encountered

and related to frictionally excited thermo-elastic instability. The stability limit is estimated analytically using two different approaches from the literature and compared to the FEM simulation findings. In view of these findings, the validity of thermo-elastic predictions beyond the stable regime has to be seriously questioned. The stability limit needs to be estimated in the first place, e.g. by the described analytical methods. Extrapolating from results of linear elastic simulations to sliding speeds above the stability limit is not advised.

Chapter 3 is concerned with the computational simulation of a forming process of a particulate MMC component. A hierarchical concept is utilized within the framework of the Finite Element Method to study a Gleeble-type experiment employing two micromechanics of materials approaches. The analytical incremental Mori-Tanaka method, which has been extended to account for finite strains, is employed to predict mesoscale responses and approximations of microscale fields. The periodic microfield approach using unit cells is utilized to predict the mesoscopic responses as well as the fluctuating microfields. It also serves as a reference to assess the quality of the results of the analytical approach. The advantages of the IMT are low computational costs in terms of speed and memory requirements, and the possibility to employ a micromechanical constitutive material law within the FEM to a entire structure or component. Due to performance and capacity restrictions, this is not possible with the PMA at the moment. When comparing the IMT results to those of the PMA on the mesoscale, the former's predictions are found to be excellent and the assumptions made in the IMT's formulations are shown to hold. Predictions on the microscale are limited by the inherent mean field assumptions, though, so the PMA is still the tool of choice on these length scales.

A comparison of the two constitutive material laws IMT and J2-plasticity is performed. While for the given material, the difference in response is subtle, access to predictions on the microscopic level is lost when only relying on the homogenized material. Furthermore, a method to address mesoscopic strain concentration of periodic unit cells under certain circumstances is presented.

Appendix A

Transformation of the deformation to rotated coordinate systems, step by step procedure

The presented approach is as follows. First the evolution of deformation, described by the deformation gradient of the problem, is transformed into a rotated configuration. The master node displacements are determined to perform the simulations in this rotated coordinate system in order to solve the original problem. Homogenization is performed using the reaction forces at the master nodes, compare Eq. (1.20), to provide the transition from the micro to the mesoscopic level. The results, e.g. the Cauchy or the first Piola-Kirchhoff stress tensors, are then transformed back to the original coordinate system.

The individual steps of the actual procedure are demonstrated by the example of simple shear in the 23-plane.

1. The evolution of the deformation gradient, $\mathbf{F}(t)$, is prescribed in a master coordinate system for the original, unrotated configuration using, e.g. Eq. (1.16).
2. Transform the deformation gradient to a rotated $'$ -coordinate system, $\mathbf{F}'(t)$, in which

the FEM analysis will be performed,

$$\mathbf{F}' = \mathbf{R}(\alpha)\mathbf{F}(t)\mathbf{R}^T(\alpha), \quad (\text{A.1})$$

with $\mathbf{R}(\alpha)$ being the orthogonal ($\mathbf{R}^T = \mathbf{R}^{-1}$) transformation matrix of rank two for rotation about the angle α . For example, $\mathbf{R}(\alpha)$ for rotation about the 1-axis (transforming the 'simple shear in the 23-plane' problem) formally reads

$$\mathbf{R}(\alpha) = \begin{pmatrix} 1 & 0 & 0 \\ 0 & \cos(\alpha) & \sin(\alpha) \\ 0 & -\sin(\alpha) & \cos(\alpha) \end{pmatrix}. \quad (\text{A.2})$$

3. From $\mathbf{F}'(t)$, compute the evolution of the new master node coordinates, $d\mathbf{x} = [d\vec{x}_1, d\vec{x}_2, d\vec{x}_3]$, from the definition of the deformation gradient

$$d\mathbf{x} = \mathbf{F}' \cdot d\mathbf{X}. \quad (\text{A.3})$$

For the cubic unit cells employed, the column vectors of $d\mathbf{x}$ end up containing the actual coordinates of the master nodes in the deformed configuration. From $d\mathbf{x}$, the displacements of the master nodes for performing the simulation in the rotated configuration are computed by subtracting the identity matrix (the original position vectors).

4. Run simulation in the rotated system by prescribing the nonlinear evolution of the master node displacements, for example by employing amplitude curves.
5. Extract the reaction forces at the master nodes in the rotated configuration.
6. From the actual master node coordinates and periodicity vectors of the unit cells, compute normal vectors, \vec{n}_i , in the undeformed and deformed states, compare Eq. 1.19.

The normal vectors in the undeformed configuration follow from the vector product of the initial periodicity vectors, where no displacements have occurred.

7. Solve system of equations from normal vectors, \mathbf{N} , and reaction forces, \mathbf{H} , to obtain the Cauchy, $\boldsymbol{\sigma}$, or the first Piola-Kirchhoff, \mathbf{P} , stress tensor in the rotated configuration, compare Eq. 1.20.

$$\begin{aligned}\boldsymbol{\sigma}' &= {}^t\mathbf{H}' \cdot \mathbf{n}' \\ \mathbf{P}' &= {}^t\mathbf{H}' \cdot \mathbf{N}' ,\end{aligned}\tag{A.4}$$

8. Transform stress tensors and deformation gradient back to the original coordinate system. If tensors of rank 2 are employed, quadratic multiplication with the rotation transformation matrix, $\mathbf{R}(-\alpha)$, is performed. However, the second rank tensors of stress are often formally denoted in terms of (1x6)-vectors of the tensors' components. In this case, transformation is achieved by multiplication with a (6x6) matrix, R_{6x6} , e.g. for the Cauchy stress 'vector' this reads

$$\vec{\sigma} = \mathbf{R}_{6x6} \cdot \vec{\sigma}' ,\tag{A.5}$$

with rotation transformation matrices of the form

$$\mathbf{R}_{6x6} = \begin{pmatrix} 1 & 0 & 0 & 0 & 0 & 0 \\ 0 & \cos^2(\alpha) & \sin^2(\alpha) & \sin(2\alpha) & 0 & 0 \\ 0 & \sin^2(\alpha) & \cos^2(\alpha) & -\sin(2\alpha) & 0 & 0 \\ 0 & -\sin(2\alpha)/2 & \sin(2\alpha)/2 & \cos(2\alpha) & 0 & 0 \\ 0 & 0 & 0 & 0 & \cos(\alpha) & \sin(\alpha) \\ 0 & 0 & 0 & 0 & -\sin(\alpha) & \cos(\alpha) \end{pmatrix} ,\tag{A.6}$$

as an example for rotation about the 1-axis. The rotation matrix of course is different for the first Piola-Kirchhoff stress 'vector', as the latter comprises nine individual components.

Bibliography

- J.R. Barber. Thermoelastic Instabilities in the Sliding of Conforming Solids. *Proc.Roy.Soc.*, pages 381–394, 1969.
- Y. Benveniste. A New Approach to the Application of Mori-Tanaka’s Theory in Composite Materials. *Mechanics of Materials*, 6(2):147–157, 1987.
- B. Bhushan, editor. *Modern Tribology Handbook*, volume 1 - Principles of Tribology. CRC Press, 2001.
- D. B. Bogy. Two Edge-Bonded Elastic Wedges Of Different Materials And Wedge Angles Under Surface Traction. *J. Appl. Mech.*, 38(2):377–386, 1971.
- H.J. Böhm. A Short Introduction To Continuum Micromechanics. In *Mechanics of Microstructured Materials*, pages 1–40. CISM Courses and Lectures, Springer-Verlag, Vienna, 2002.
- H.J. Böhm, A. Eckschlager, and W. Han. Multi-Inclusion Unit Cell Models for Metal Matrix Composites with Randomly Oriented Discontinuous Reinforcements. *Computational Material Science*, 25(1-2):42–53, 2002.
- H.J. Böhm, W. Han, and A. Eckschlager. Multi Inclusion Unit Cell Studies of Reinforcement Stresses and Particle Failure in Discontinuously Reinforced Ductile Matrix Composites. *Comput.Model.Engng.Sci.*, 5:2–20, 2004.

- M. Bornert. Homogénéisation des milieux aléatoires: bornes et estimations. In *Homogénéisation en mécanique des matériaux 1. Matériaux aléatoires élastiques et milieux périodiques*, pages 133–221, Paris, 2001. Editions Hermès.
- M. Bornert, T. Bretheau, and P. Gilormini, editors. *Homogénéisation en mécanique des matériaux. 2. Comportements non linéaires et problèmes ouverts*. Hermes, Science, Paris, 2001.
- M. Ciavarella and J.R. Barber. Stability of Thermoelastic Contact for a Rectangular Elastic Block Sliding against a Rigid Wall. *Eur. J. Mech. A/Solids*, 24:371–376, 2005.
- I. Doghri and A. Ouair. Homogenization of Two-Phase Elasto-Plastic Composite Materials and Structures. *Int.J.Sol.Struct*, 40 (7)(1):1681–1712, 2003.
- T.A. Dow and R.A. Burton. Thermoelastic Instability of Sliding Contact in the Absence of Wear. *Wear*, 19:315–328, 1972.
- J.D. Eshelby. The Determination of the Elastic Field of an Ellipsoidal Inclusion and Related Problems. *Proc.of the Royal Society London*, A241:376–396, 1957.
- G. Fichera. Boundary Value Problems of Elasticity with Unilateral Constraints. In *Handbuch der Physik*, volume a/2, pages 391–424. Springer, Berlin, 1972.
- A.C. Gavazzi and D.C. Lagoudas. On the Numerical Evaluation of Eshelby’s Tensor and its Application to Elastoplastic Fibrous Composites. *Comput.Mech*, 7:12–19, 1990.
- C. Gonzalez and J. Llorca. A Self-consistent Approach to the Elasto-Plastic Behavior of Two-phase Materials including Damage. *J.Mech.Phys.Solids*, 48:675–692, 2000.
- R. Hill. Elastic Properties of Reinforced Solids: Some Theoretical Principles. *J.Mech.Phys.Sol*, 11:357–372, 1963.
- C.O Huber, M.H. Luxner, S. Kremmer, S. Nogales, H.J. Böhm, and H.E. Pettermann. Forming Simulations of MMC Components by a Micromechanics Based Hierarchical

- FEM Approach. In J. M. A. Cesar de Sa and A. D. Santos, editors, *9th International Conference in Numerical Methods in Industrial Forming Processes (NUMIFORM07)*, pages 1351–1357. American Institute of Physics, 2007.
- K.L. Johnson. *Contact Mechanics*. Cambridge Univ. Pr., 1992.
- N. Kikuchi and J.T. Oden. *Contact Problems in Elasticity: A Study of Variational Inequalities and Finite Element Methods*. SIAM, Philadelphia, PA, 1988.
- U. Landman, W.D. Luetke, and E.M. Ringer. Molecular Dynamics Simulations of Adhesive Contact Formulation and Friction. In I.L. Singer and H.M. Pollock, editors, *Fundamentals of Friction: Macroscopic and Microscopic Processes*, page 463. Kluwer Academic Publishers, Dordrecht, 1993.
- M. Luxner. Nichtlineare Homogenisierung von FEM Einheitszellenanalysen für MMCs. AAR-ILSB Report No.37, Institute of Lightweight Design and Structural Biomechanics, Vienna University of Technology, 2007.
- T. Mori and T. Tanaka. Average Stress in the Matrix and Average Elastic Energy of Materials with Misfitting Inclusions. *Acta Metall.*, 21(5):571–574, 1973.
- D. H. Pahr. Linear and Non-linear Homogenization using FEM. Technical report, Institute of Lightweight Design and Structural Biomechanics, Vienna University of Technology, 2004.
- H. E. Pettermann, A. F. Plankensteiner, H. J. Böhm, and F. G. Rammerstorfer. A Thermo-Elasto-Plastic Constitutive Law for Inhomogeneous Materials Based on an Incremental Mori-Tanaka Approach. *Computers and Structures*, 71:197 – 214, 1999.
- H.E. Pettermann. *Derivation and Finite Element Implementation of Constitutive Material Laws for Multiphase Composites Based on Mori-Tanaka Approaches*. PhD thesis, Institute of Lightweight Structures and Aerospace Engineering, Vienna University of Technology, 1997. (also appeared as VDI Report 217/18, VDI-Verlag, Düsseldorf, Germany, 1997).

- H.E. Pettermann and S. Suresh. A Comprehensive Unit Cell Model for the Thermomechanical Response of 1-3 Piezoelectric Composites. *International Journal of Solids and Structures*, 37:5447–5464, 2000.
- H.E. Pettermann, H.J. Böhm, and F.G. Rammerstorfer. Some Direction Dependent Properties of Matrix-Inclusion Type Composites with Given Reinforcement Orientation Distributions. *Composites*, 28B(3):1–24, 1997.
- H.E. Pettermann, C.O. Huber, M.H. Luxner, S. Nogales, and H.J. Böhm. Finite Elastic-Plastic Deformation of MMC Components – Multiscale Mean Field and Unit Cell Simulations. In *Volume of Abstracts of the 35th Solid Mechanics Conference, SolMech2006*, Krakow, Poland, 2006.
- O. Pierard and I. Doghri. A Study of Various Estimates of the Macroscopic Tangent Operator in the Incremental Homogenization of Elasto-plastic Composites. *Int.J.Mult.Comp.Eng.*, 4(4):521–543, 2006.
- C. Poletti. *Hot Deformation and Properties of PRTi alloys*. PhD thesis, Vienna University of Technology, Vienna, 2005.
- C. Poletti, W. Marketz, and H.P. Degischer. Hot Formability of a Particle Reinforced Ti-Alloy. *Ti-2003 Science and Technology*, pages 2531–2538, 2003.
- C. Poletti, A. Merstallinger, Th. Schubert, W. Marketz, and H.P. Degischer. Wear and Friction Coefficients of Particle Reinforced Ti-Alloys. *Mat.-wiss. u. Werkstofftech.*, 35(10):741 – 749, 2004.
- F.G. Rammerstorfer and H.J. Böhm. Lecture Notes Composite Engineering. *Institute of Lightweight Structures and Structural Biomechanics, Vienna University of Technology*. Vienna, Austria, 2004.
- D.A. Rigney and J.P. Hirth. Plastic Deformation and Sliding Friction of Metals. *Wear*, 53:345–370, 1979.

- C. Schuecker. *Mechanism based modeling of damage and failure in fiber reinforced polymer laminates*. PhD thesis, Vienna University of Technology, 2005.
- J. Segurado, A. Merstallinger, and H.E. Pettermann. Numerical Simulations in Tribology – A Micro-mechanics of Materials Approach. In *Proc.of the WTC2001*. The Austrian Tribology Society, Austria, 2001.
- Simulia Inc. *ABAQUS/Standard Manual*. Providence, RI, USA, v6.4 edition, 2004.
- S. Suresh, A. Mortensen, and A. Needleman, editors. *Fundamentals of Metal-Matrix Composites*. Butterworth-Heinemann, Stoneham, MA, USA, 1993.
- G.P. Tandon and G.J. Weng. A Theory of Particle-Reinforced Plasticity. *J.Appl.Mech.*, 55:126–135, 1988.
- H. Uetz and J. Föhl. Wear as an Energy Transformation Process. *Wear*, 49:253–264, 1978.
- G.J. Weng. The Theoretical Connection between Mori-Tanaka Theory and the Hashin-Shtrikman-Walpole Bounds. *Int.J.Engng.Sci.*, 28:1111–1120, 1990.
- C. Zweben. *Comprehensive Composite Materials*, volume 3 - Metal Matrix Composites. Cambridge University Press, UK, 2000.